Design and Understanding of Reconfigurable Surface Wave Communication Technology

Zhiyuan Chu

A thesis submitted for the degree of

Doctor of Philosophy

of

University College London

Information and Communication Engineering Research Group

Department of Electronic and Electrical Engineering

University College London

August 2023

Statement of Originality

I, Zhiyuan Chu, confirm that the work presented in this thesis is my own. Where information has been derived from other sources, I confirm that this has been indicated in the thesis.

Signed: Zhiyuan Chu

Date: 15 / 08 / 2023

"One must imagine Sisyphus happy." — Albert Camus (1913 – 1960)

Abstract

This thesis endeavors to develop innovative reconfigurable surface wave transmission technology and investigate its propagation characteristics. Surface waves exhibit potential advantages over traditional space waves, including low path attenuation and resistance to interference. This introduces a promising avenue for highly intelligent wireless communication systems to tackle the intricate challenges posed by complex channel environments and extensive device connectivity.

The study introduces a variety of novel porous reconfigurable surface wave platforms applicable to diverse scenarios, ranging from outdoor to indoor and on-chip communications. This platform can dynamically establish diverse fluid-metal-based pathways on the surface, effectively guiding and localizing the propagation of surface waves. These pathways encompass linear, curved, and distributed trajectories.

Theoretically, this study establishes a relatively comprehensive mathematical analysis model to forecast the electromagnetic field intensity and losses of surface waves within propagation pathways. This facilitates a systematic understanding of how variables like surface material, thickness, cavity porosity, and more impact propagation performance, thus enabling the effective optimization of reconfigurable surface structures.

In practice, the study evaluates numerous outcomes through 3D-printed platforms and thorough electromagnetic simulations. An intricate exploration encompasses parameters such as metal layer count, pathway width, configurations of turns and intersections, symmetry, and asymmetry. These investigations further contribute to the optimization of dynamic pathway structures. Moreover, simulation outcomes are corroborated through corresponding experiments, confirming the accuracy of the mathematical analysis presented within this thesis.

The research findings unequivocally underscore the feasibility of the proposed reconfigurable platform concerning broadband capacity, minimal path loss, and dynamic reconfigurability in communication. The platform adeptly materializes adaptable functionalities, encompassing surface wave path configuration, power

distribution, and frequency selection, thereby fostering heightened flexibility and adaptability within surface wave communication networks. Furthermore, it accentuates the prospective application of surface wave technology within future communication systems.

Impact Statement

Summary of the impact

The rapid development and widespread application of fifth-generation (5G) communication technology have significantly improved information exchange and retrieval. However, with the continuous increase in connected devices, the design of space waves as carriers for information transmission has become more complex, and bandwidth resources are under tremendous strain. In response to this, we have undertaken a research initiative focused on surface wave communication. The objective is to explore new carrier modes by transmitting electromagnetic waves on surfaces, attempting to address various communication application scenarios within the realm of 5G.

Underpinning research

In recent years, software-controlled metamaterials and programmable metasurfaces have emerged as innovative technologies enhancing wireless communication systems. Surface Wave Communications (SWC), based on these advancements, has gained significant attention [1]. The foundational theory of surface waves dates back to the 19th century, pioneered by Jonathan Zenneck [2]. In the 1950s, Professor Harold Barlow's group at University College London (UCL) furthered this theory, exploring electromagnetic and attenuation characteristics of surface waves along surfaces [3]. Their work laid the theoretical groundwork for subsequent research. In the early 2010s, Professor Kin-Fai (Kenneth) Tong's group at UCL explored the use of surface wave-based Hybrid On-Chip Networks (NoC) systems, providing a potential alternative for scalability and performance issues in traditional wired NoC systems [4]. Concepts of waveguide design, propagation pathways, and industrialization for surface waves were also introduced. Recent collaborations between Professor Kai-Kit Wong and Professor Kin-Fai Kenneth Tong at UCL have introduced fluidic antennas, expanding the application scenarios of surface waves [5].

References to the research

[1] A. Li, S. Singh, and D. Sievenpiper, "Metasurfaces and their applications,"

Nanophotonics, vol. 7, no. 6, pp. 989-1011, 2018.

[2] A. Sommerfeld, "Über die Ausbreitung der Wellen in der drahtlosen Telegraphie," *Annalen der Physik*, vol. 333, no. 4, pp. 665-736, 1909.

[3] H. M. Barlow and J. Brown, "Radio surface waves," *IEEE Transactions on Antennas and Propagation*, vol. 10, no. 6, pp. 750-754, 1962.

[4] M. O. Agyeman, J.-X. Wan, Q.-T. Vien, W. Zong, A. Yakovlev, K.-F. Tong, and T. Mak, "On the design of reliable hybrid wired-wireless network-on-chip architectures," in *2015 IEEE 9th International Symposium on Embedded Multicore/Many-core Systems-on-Chip*, pp. 251-258, 2015.

[5] Y. Shen, K.-F. Tong, and K.-K. Wong, "Beam-steering surface wave fluid antennas for MIMO applications," in *2020 IEEE Asia-Pacific Microwave Conference (APMC)*, pp. 634-636, 2020.

Details of the impact

This research provides a thorough exploration of surface wave communication, covering fundamental theory and recent developments. It establishes formulas correlating field strength with surface impedance and details the inherent propagation characteristics of surface waves. The study highlights advantages and applications, including outdoor communication with reconfigurable intelligent surfaces and secure indoor communication [a].

Introducing a novel reconfigurable surface wave platform, the research enables dynamic control of propagation paths, incorporating fluidic metals and microfluidic technology for adaptability [b]. The study innovatively establishes a comprehensive mathematical model for predicting electromagnetic field strength and losses in surface wave pathways [c]. Practical validation using a 3D-printed platform examines the impact of parameters on surface wave pathways [d]. Results contribute to a systematic understanding, optimizing reconfigurable surface structures. The outcomes introduce a reconfigurable platform, enhancing adaptability in surface wave communication networks. This opens possibilities for efficient adaptive wireless communication in dense device environments. The study advances surface wave communication through mathematical modeling, experimental validation, and opti-

mization techniques.

This project has greatly benefited from the generous support of Engineering and Physical Sciences Research Council (EPSRC), British Telecommunications, Toshiba, and the City University of Hong Kong.

Sources to corroborate the impact

[a] K.-K. Wong, K.-F. Tong, Z. Chu, and Y. Zhang, "A vision to smart radio environment: Surface wave communication superhighways," *IEEE Wireless Communications*, vol. 28, no. 1, pp. 112-119, 2020.

[b] Z. Chu, K.-K. Wong, and K.-F. Tong, "Enhancing and localizing surface wave propagation with reconfigurable surfaces," in *2021 International Symposium on Antennas and Propagation (ISAP)*, pp. 1-2, October 2021, Taipei, Taiwan.

[c] Z. Chu, K.-F. Tong, K.-K. Wong, C.-B. Chae, and C. H. Chan, "On propagation characteristics of reconfigurable surface wave platform: Simulation and experimental verification," *IEEE Transactions on Antennas and Propagation*, (submitted August 2023, under review).

[d] Z. Chu, K.-K. Wong, and K.-F. Tong, "Reconfigurable surface wave platform using fluidic conductive structures," in *2021 IEEE International Symposium on Antennas and Propagation and USNC-URSI Radio Science Meeting (APS/URSI)*, pp. 909-910, December 2021, Singapore.

Key researchers: Mr. Zhiyuan Chu, PhD student of UCL (2019-2023); Prof. Kai-Kit Wong, Professor of Wireless Communications of UCL (2006- present); Prof. Kin-Fai (Kenneth) Tong, Professor of Antennas and Applied Electromagnetics of UCL (2005-present).

Peer-reviewed funding: Since 2021, the research programme has been supported by the EPSRC under Grant EP/V052942/1.

Acknowledgments

I would like to express my profound gratitude to my supervisor, Prof. Kai-Kit Wong, for his invaluable guidance and support throughout my PhD. Kit's expertise in wireless communications, combined with his insightful comprehension of theoretical practical considerations, has significantly shaped the trajectory of my research. Whenever I faced obstacles during my research, he consistently engaged with me in passionate discussions, actively guiding me in exploring potential solutions. I still recall Kit's advice that he used the metaphor of searching for hidden treasures in the depths of the ocean to emphasize the importance of delving deep and contemplating far-reaching horizons in order to uncover truly invaluable insights. It is through Kit's guidance that I have persevered and completed this thesis.

I also extend heartfelt gratitude to Prof. Kin-Fai (Kenneth) Tong for his invaluable guidance and support throughout my doctoral journey. Kenneth's expertise and meticulous approach in electromagnetic and antennas have been truly commendable. He demonstrates great attention to detail when addressing research problems and engages in patient discussions, stimulating comprehensive thinking on various aspects of the research questions. Furthermore, Kenneth's calm demeanor and guidance have been instrumental in helping me navigate through technical challenges and find suitable solutions. Additionally, Kenneth has also demonstrated his wit and humor, creating a pleasant working environment that keeps me positive.

I want to express my gratitude to Dr. Laura Toni for her kind support throughout my PhD study. And I'd give thank my colleagues: Dr. Hao Xu, Dr. Chao Wang, Dr. Tongyang Xu, Haizhe Liu, and Hadumanro Malau. Their invaluable research experiences and insightful advice have enriched my journey at UCL. And my friends have made my time at UCL full of joy and memories. I would like to extend special thanks to Meiran Yang, Dr. Zinie Zhang, Dr. Hengbo Yue, Ruiming Zhang, Chip Qian, Yushuang Shi, Fan Wu, Weiqing Zeng, Dr. Xi Peng, Kaka Zheng, Liwei Cheng, Dr. Jingqi Gao, Yezi Lin, Zhaohui Zhu, Teng Teng, and Yuanhao Zhao.

Finally, I would like to express my deepest gratitude to my parents for their unwavering support and love on my journey to pursue my dreams.

Contents

List of Figures

List of Tables

List of Symbols and Operators

A	Amplitude of electromagnetic wave
d	Propagation distance
d_e	Depth of splitting pin
d_m	Propagation distance of path m
$\hat{\boldsymbol{E}}_p$	Electric field of surface wave in its propagation direction
$\hat{\boldsymbol{E}}_x$	Electric field of surface wave in the $+x$-direction
$\hat{\boldsymbol{E}}_{x,c}$	Cumulative electric field of all surface wave rays in the $+x$-direction at the measured point
$\hat{\boldsymbol{E}}_z$	Electric field of surface wave in the $+z$-direction
f	Operating frequency
f_b	Frequency band
h_a	Height of transducer aperture
h_d	Thickness of the dielectric layer
h_m	Thickness of the metal ground
$\hat{\boldsymbol{H}}_v$	Magnetic field of surface wave in the vertical direction
$\hat{\boldsymbol{H}}_y$	Magnetic field of surface wave in the $+y$-direction
j	Complex number, $\sqrt{-1}$
k	Wave number of free space
k_p	Wave number of surface wave in its propagation direction
k_x	Wave number of surface wave in the $+x$-direction
k_z	Wave number of surface wave in the $+z$-direction
L	Path loss

l_w	Length of metal walls
m	Number of surface wave paths
n	Number of reflections
Q_m	Set factor
r	Radius of cavity/metal pin
R	Reflection coefficient
R_s	Surface resistance
t	Time
T_1	Transmission coefficient of the surface wave ray propagating from air to metal
T_2	Transmission coefficient of the surface wave ray propagating from metal to air
$\hat{\boldsymbol{v}}$	Unit vector in the vertical direction
w_1	Distance from the source point to the lower metal wall
w_2	Distance from the source point to the upper metal wall
w_a	Width of transducer aperture
w_c	Center-to-center separation between adjacent cavities/metal pins
w_h	Horizontal center-to-center distance between adjacent cavities/metal pins
w_p	Pathway width, i.e., the vertical dimension between two rows of metal walls
w_t	Corner width
w_v	Vertical center-to-center distance between adjacent cavities/metal pins
w_w	Width of metal walls
$\hat{\boldsymbol{x}}$	Unit vector in the $+x$-direction
X_s	Surface reactance
$\hat{\boldsymbol{y}}$	Unit vector in the $+y$-direction
y_0	Measured point position at the y-axis
$\hat{\boldsymbol{z}}$	Unit vector in the $+z$-direction
Z_s	Surface impedance

z_0	Measured point position at the z-axis
α_x	Attenuation constant in the $+x$-direction
α_z	Attenuation constant in the $+z$-direction
β_x	Phase constant in the $+x$-direction
β_z	Phase constant in the $+z$-direction
γ_0	Propagation coefficient of free space
γ_x	Propagation coefficient in the $+x$-direction
γ_z	Propagation coefficient in the $+z$-direction
ε_0	Permittivity of free space
ε_r	Relative permittivity of the dielectric layer
$\varepsilon_r^{\text{eff}}$	Effective relative permittivity of the porous dielectric layer
ε_w	Permittivity of metal walls
θ_0	Tilted angle included between the z-axis and the line connecting the source and measured points
θ_i	Incident angle of mathematical model inside the pathway
θ_i'	Incident angle of mathematical model outside the pathway
θ_B	Brewster angle
θ_m	Reflection angle of the surface wave ray in path m
θ_t	Transmission angle
λ	Wavelength
μ_0	Permeability of free space
π	Pi
ρ	Porosity of the dielectric layer
σ	Standard deviation
σ_c	Electric conductivity of copper
σ_g	Electric conductivity of Galinstan
σ_m	Electric conductivity of metal pin
σ_m	Electric conductivity of metal pin
σ_M	Electric conductivity of ideal thermoelectric semiconductor
σ_w	Electric conductivity of metal wall

ω	Angular frequency
Δ	Skin depth
∞	Infinity
mod	Remainder function
$\tan\delta$	Loss tangent
$^\circ$	Degree
$^\circ$C	Degree centigrade
$\mathbb{N}$	Natural numbers

List of Abbreviations

2D	Two-dimensional
3D	Three-dimensional
5G	Fifth-generation
6G	Sixth-generation
AAU	Active Antenna Unit
CST	Computer Simulation Technology
E-field	Electric Field
FPGA	Field Programmable Gate Arrays
FR	Frequency Range
H-field	Magnetic Field
MATLAB	Matrix Laboratory
MIMO	Multiple-Input Multiple-Output
mmWave	Millimeter Wave
NLOS	Non-Line-of-Sight
NoC	Network-on-Chip
PEC	Perfect Electrical Conductor
PTFE	Polytetrafluoroethylene
RIS	Reconfigurable Intelligent Surface
SIMO	Single-Input Multiple-Output
SISO	Single-Input Single-Output
SIW	Substrate-Integrated Waveguides
SPP	Surface Plasmon Polariton

SWC	Surface Wave Communications
TE	Transverse-Electric
TM	Transverse-Magnetic
WR	Rectangular Waveguide
ZSW	Zenneck Surface Wave

Chapter 1

Introduction

1.1 Background

The rapid advancement and extensive deployment of fifth-generation (5G) communication technology have improved information exchange and retrieval, offering individuals seamless connectivity at any time and location. Nevertheless, the expansion of wireless communication networks, coupled with the scarcity of available spectrum resources and the proliferation of connected devices, has presented formidable challenges and constraints to conventional communication approaches. To surmount these hurdles and furnish enhanced efficacy and dependability, there is a concerted effort underway to investigate the possibilities afforded by emerging communication technologies.

Surface wave communications (SWC), as an emerging communication technology, has garnered considerable interest in recent years due to its potential applications across various communication scenarios [3, 1, 2]. In SWC, the process of exciting surface waves is not overly complex. Electromagnetic signals, originating from antennas or waveguides, are transmitted and incident upon the surface at specific angles, leading to the excitation of surface waves that subsequently propagate along the surface closely [4]. This propagation surface can be common homogeneous metal or dielectric-metal surfaces, or it can be specially designed metasurfaces that enable further manipulation of surface characteristics[5, 6, 7]. Fig. 1.1

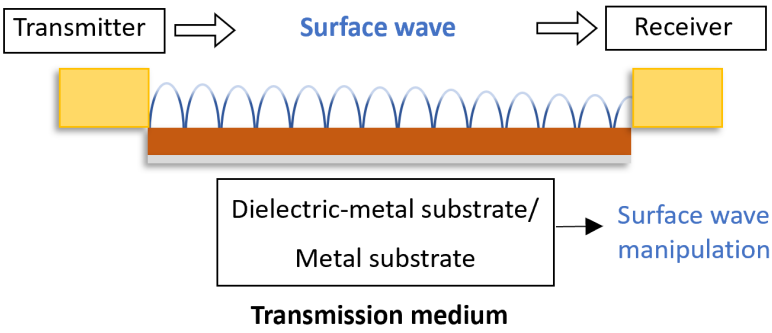

Figure 1.1: An example of surface wave propagation.

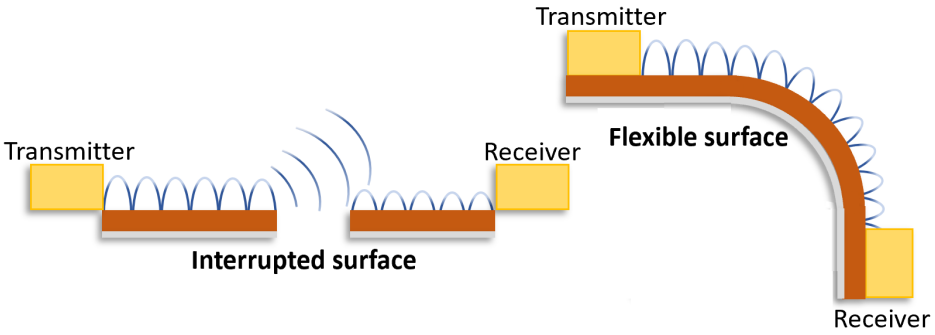

Figure 1.2: Two examples of surface wave propagation surface: interrupted surface and curved surface.

depicts a fundamental SWC model, wherein it is evident that surface waves travel along the substrate medium between the transmitting and receiving ends, thereby facilitating stable transmission and reception of information.

Compared to traditional space propagation methods, SWC has the potential to offer distinctive advantages. Firstly, owing to the electromagnetic properties of surface waves as cylindrical waves, its attenuation of field strength power is inversely proportional to the propagation distance d, in contrast to the squared distance d^2 in space waves. This fundamental distinction demonstrates that SWC exhibits lower transmission losses, effectively mitigating signal attenuation during long-distance transmissions [8]. And surface waves exhibit a distinctive characteristic of adhering closely to surfaces, facilitating stable and efficient propagation within a two-dimensional (2D) plane. And the power distribution of surface waves

concentrates predominantly near the surface and experiences rapid attenuation as one moves away from the vertical surface, this phenomenon suggests that proximate substrates situated near antennas or waveguides can function as direct propagation medium in SWC. This quality effectively diminishes the interference between surface wave signals and other space signals within a three-dimensional (3D) space, thereby mitigating mutual interference. Furthermore, this implies that SWC can function without the stringent requirement to allocate distinct frequencies to circumvent aerial interference. Consequently, this yields a diminished demand for supplementary spectrum resources, thereby optimizing the utilization of available spectrum. Moreover, due to the focused and confined propagation path along the medium surface, surface waves exhibit enhanced resilience against external interference in short-distance transmissions. Additionally, as depicted in Fig. 1.2, surface waves can propagate reliably on interrupted and curved surfaces. It shows that surface waves are still able to traverse gaps and continue gliding along the surface. These characteristics underscore the robust connectivity of surface waves and their well-suited practicality in various application [1].

In recent years, there has been a notable increase in the widespread application of surface waves across various domains. Within network-on-chip (NoC) systems, surface waves have been proposed as a viable option for achieving high-speed communication and data transmission. By integrating multiple miniature antenna units on chips, surface waves can be utilized to establish flexible communication paths between nodes [9, 10]. In the realm of wearable devices, surface wave antennas have shown potential for facilitating information transmission and reception between the human body's surface and the surrounding environment [11, 12]. Furthermore, the emergence of surface wave fluid antennas, a novel antenna technology that combines fluid metal with surface waves, holds promise. This technology enables the manipulation and radiation of surface waves by controlling the properties and flow state of the fluid medium [13, 14]. Additionally, in industrial environment, surface waves are being explored as an alternative to reduce overall lifecycle costs. Leveraging surface waves for signal and energy transmission in industrial equipment and

systems can lead to decreased costs associated with cables while enhancing reliability and flexibility [15].

In summary, the control and manipulation of surface waves through metasurfaces or reconfigurable surfaces, as pointed in Fig. 1.1, allow for the regulation of their propagation characteristics, transmission paths, and radiation effects, thereby expanding their applications in fields such as communication, sensing, and optics. Despite facing challenges in both theory and practice, including issues like multipath interference and pathway allocation, surface wave communication presents a potential novel approach and solution for the design and optimization of modern communication systems. Consequently, this thesis aims to investigate a reconfigurable platform based on the fundamental principles of surface waves to address the existing challenges and enhance SWC systems. By utilizing this platform, precise controlling surface waves can be exerted over critical propagation characteristics, such as propagation direction, power allocation, frequency selection, and other key features associated with surface waves. Furthermore, this thesis delves into the exploration of SWC technology in various domains, including NoC communication, indoor secure communication, and Non-Line-of-Sight (NLOS) communication. The vision of this thesis is to provide research-based support for the advancement of intelligent and highly efficient communication technologies based on surface waves.

1.2 Research Motivations

The motivations behind this research stem from the challenges and opportunities presented by surface wave applications where it is common to encounter scenarios with multiple simultaneous propagation ends [1], where each end serves as a transceiver for dynamic and flexible multi-end in SWC. However, on common even homogeneous surfaces, surface waves generally propagate and diffuse across the entire surface [16]. This introduces several existing challenges in SWC: 1) The

[1]Throughout this thesis, the term 'end' is used as a general term to refer to both the transmitting and receiving nodes of communication links, as well as the terminal devices of the communication system, such as waveguides or user devices like computers, smartphones, and sensors in surface wave communications.

propagation path of surface waves cannot be dynamically controlled, preventing the adjustment of the directional propagation of surface waves for achieving flexible SWC. 2) Surface wave multipath interference: Since surface waves originate from different points and propagate along the surface, multiple surface waves corresponding to different propagation pathways can reach the receiving end totally. This leads to mutual interference, causing phenomena such as delay spread and adversely affecting signal quality and reliability. 3) Surface wave fast fading: Due to multiple reflections and diffractions of surface waves along different pathways, the phase and amplitude of surface waves undergo changes upon reaching the receiving end. As a result, the received signal strength becomes unstable, posing difficulties in accurate signal recovery and demodulation. 4) Surface wave transmission Security: The broadcast of surface wave signals, without specific dedicated propagation pathways, presents challenges in selecting receiving ends. Additionally, the lack of predefined pathways makes SWC vulnerable to potential signal interception and disruption, thus compromising its security.

Clearly, the above issues also arise in traditional wireless communications. The distinction lies in the context of SWC, ideally, these challenges and questions can be addressed by implementing specific SWC pathways to concentrate and control the propagation directions of surface wave signals on the surface. However, the current research progress in manipulating the direction of surface wave propagation is still limited, lacking the necessary flexibility to adapt to diverse communication needs and changing environments. These limitations motivate the investigation of dynamic control over the direction of surface wave propagation using dedicated propagation pathways. In order to solve these existing issues, this study considers the following research directions as follows:

Dedicated pathways: Research should focus on studying directional transmission and end-to-end communication schemes with dedicated propagation pathways to mitigate the effects of multipath interference effectively.

Flexibility and adaptability: The development of a reconfigurable hardware architecture capable of dynamically controlling the direction of surface wave propa-

gation is essential. Such an architecture would enable flexible adjustment of SWC pathways according to communication requirements and network typologies while minimizing energy consumption.

Multi-end support: Current surface wave research has primarily concentrated on single-input single-output (SISO) architectures, with limited exploration of single-input multiple-output (SIMO) or multiple-input multiple-output (MIMO) architectures. A shared SWC platform with multi-end support demands dynamic control of surface wave propagation direction, enabling simultaneous resource sharing among multiple ends, thereby enhancing system capacity and scalability.

Enhanced communication quality: By dynamically controlling the direction of surface wave, signal propagation pathways and propagation environments can be optimized, leading to reduced attenuation, interference, and propagation delay. These improvements significantly enhance communication quality, decrease bit error rates, and enable more reliable data transmission.

In addressing these challenges, this thesis has contributed correspondingly, as detailed in Section 1.3 and supported by relevant publications in Section 1.4.

1.3 Thesis Organization and Main Contributions

Following this introductory chapter, the subsequent chapters of this thesis are organized as follows. Chapter 2 presents an introduction to fundamental theories and the latest research works related to surface waves. Driven by the research motivations outlined in Section 1.2, this thesis have sequentially constructed four technical chapters on reconfigurable surface wave platforms, specifically addressing the mathematical analysis model, reconfigurable pathway and distribution pathway. These chapters, in order, are Chapter 3, Chapter 4 and Chapter 5, respectively, comprehensively exploring the effectiveness of reconfigurable surfaces in a progressive manner. Finally, the conclusions of this thesis and future works based on the findings are summarized in Chapter 6. The following section provide a summary of the content and contributions of each chapter.

In Chapter 2, an extensive examination is conducted on the fundamental theo-

ries and recent research pertaining to surface waves. The equations describing the field strength and surface impedance of surface waves are presented, providing a detailed demonstration of the inherent propagation characteristics of surface waves as carriers of information. Drawing upon this foundational knowledge, a range of simulation results is provided to illustrate the uninterrupted propagation capabilities of surface waves on surfaces that are non-uniform and non-flat. Moreover, the unique advantages of surface wave communication are emphasized, including characteristics such as low loss, resistance to interference, and energy efficiency, setting it apart from conventional communication systems based on space waves. Furthermore, several potential application scenarios are thoroughly explored, such as outdoor communication employing reconfigurable intelligent surfaces (based on Paper 8 in publications' Section 1.4), indoor communication incorporating enhanced security measures (Paper 7), and the conceptualization of a network-on-chip based on surface waves.

In Chapter 3, the proposal of a novel reconfigurable surface wave platform is presented (Paper 5), along with a discussion of its geometric structure, working mechanism, and the mathematical model (Paper 6). The platform introduces a porous architecture that allows for the dynamic manipulation and control of surface wave propagation pathways (Paper 4). Furthermore, a corresponding mathematical analysis model is introduced to consider scenarios where multiple surface wave rays follow different paths, taking into account multiple reflections and transmissions at the wall. This model provides expressions for the cumulative field strength at specific measurement points on the surface, both within and beyond the metal wall pathway (Paper 3). Moreover, the influence of surface materials, metal wall material, and pathway width on the propagation characteristics is investigated in both short and long-distance transmission scenarios.

In Chapter 4, the straight pathway within the reconfigurable surface wave platform is subjected to comprehensive experimental measurements, utilizing a 3D-printed prototype and lossy Polytetrafluoroethylene (PTFE) (Paper 2). The analysis of path loss in the physical environment is conducted at different propagation dis-

tances and operating frequencies. Furthermore, the measurement and evaluation of various key factors, such as pathway widths and the number of metal wall layers, are performed to ascertain the optimal structure for the surface wave pathway. All experimental results are compared with their corresponding simulation outcomes. In addition, the design of a T-shaped reconfigurable surface with an adjustable junction is undertaken to facilitate the directional switching of surface wave propagation between a straight pathway and a pathway with a 90° turn (Paper 2). The attenuation characteristics of surface waves propagating along these two distinct pathways are measured and subjected to a comparison. Additionally, different corner configurations are examined within the 90° turn pathway, and the optimal shape with minimal turn insertion losses is determined.

In Chapter 5, the utilization of the reconfigurable surface wave platform with an adjustable T-junction is implemented to partition a surface wave signal into two segments along distribution pathways (Paper 1). The effectiveness of the split and guided surface waves, with minimal interference, is demonstrated by comparing the results of simulations and experiments. The analysis focuses on examining the impact of key physical parameters of the T-junction, including splitting depth, splitting shape, and symmetry or asymmetry. Furthermore, the feasibility of achieving varying power ratios and frequency dependence through the utilization of the reconfigurable T-junction is investigated.

In Chapter 6, the summary of the thesis is provided in Section 6.1, offering a comprehensive overview of the key findings. The chapter also delves into the existing limitations and challenges of the surface wave platform in Section 6.2, proposing potential remedies and research strategies. Additionally, this section outlines potential research directions for future surface wave studies and an ideal digital control model.

In the Appendices, detailed derivations of the surface wave excitation process and equivalent surface impedance are presented. This chapter also concludes by providing the field strength expressions for surface waves and summarizing the equivalent transmission line model. These derivation formulas serve as the theo-

retical foundation for the discussions on surface waves in this thesis.

1.4 List of Publications

The contributions discussed in Section 1.3 have resulted in the publication of three submitted journal papers (under review), three conference papers, and two magazine papers.

Journal papers:

1. **Z. Chu**, K.-F. Tong, K.-K. Wong, C.-B. Chae, and C. H. Chan, “On propagation characteristics of reconfigurable surface wave platform: Simulation and experimental verification,” *IEEE Transactions on Antennas and Propagation*. (submitted August 2023, under review)
2. **Z. Chu**, K.-F. Tong, K.-K. Wong, C.-B. Chae, and Y. Zhang, “Reconfigurable surface wave divider,” *Nature Scientific Reports*. (submitted August 2023, under review)
3. **Z. Chu**, K.-K. Wong, and K.-F. Tong, “Study on surface wave path loss in reconfigurable surface guided pathways,” *IEEE Transactions on Communications*. (in preparation)

Conference papers:

4. **Z. Chu**, K.-K. Wong, and K.-F. Tong, "Enhancing and localizing surface wave propagation with reconfigurable surfaces," in *2021 International Symposium on Antennas and Propagation (ISAP)*, pp. 1-2, October 2021, Taipei, Taiwan.
5. **Z. Chu**, K.-K. Wong, and K.-F. Tong, "Reconfigurable surface wave platform using fluidic conductive structures," in *2021 IEEE International Symposium on Antennas and Propagation and USNC-URSI Radio Science Meeting (APS/URSI)*, pp. 909-910, December 2021, Singapore.

6. **Z. Chu**, K.-K. Wong, and K.-F. Tong, "On Surface Wave Propagation Characteristics of Porosity-Based Reconfigurable Surfaces," in *2022 Asia-Pacific Microwave Conference (APMC)*, pp. 479-481, November 2022, Yokohama, Japan.

Magazine papers:

7. K.-K. Wong, K.-F. Tong, **Z. Chu**, and Y. Zhang, "A vision to smart radio environment: Surface wave communication superhighways," *IEEE Wireless Communications*, vol. 28, no. 1, pp. 112-119, 2020.
8. A. Shojaeifard, K.-K. Wong, K.-F. Tong, **Z. Chu**, A. Mourad, A. Haghighat, I. Hemadeh, N. T. Nguyen, V. Tapio, and M. Juntti, "MIMO evolution beyond 5G through reconfigurable intelligent surfaces and fluid antenna systems," *Proceedings of the IEEE*, vol. 110, no. 9, pp. 1244-1265, 2022.

Awards:

1. **Best Student Paper Award** for the paper “Enhancing and localizing surface wave propagation with reconfigurable surfaces” (list of authors in order: **Zhiyuan Chu**, Kai-Kit Wong, and Kin-Fai Tong) presented in *International Symposium on Antennas and Propagation (ISAP 2021)*, 19-22 October 2021, Taipei, Taiwan.

Chapter 2

Fundamental Theories and Related Works

2.1 Introduction

This chapter delves into the fundamental theories and recent research in surface wave communication, providing a comprehensive overview. It begins by organizing formulas that establish the correlation between the field strength and surface impedance of surface waves, which detailedly demonstrates the propagation characteristics inherent in surface waves as information carriers. Building upon this foundation, the chapter proceeds to present various simulation results that highlight the uninterrupted propagation capabilities of surface waves on non-uniform and non-flat surfaces. Additionally, the chapter emphasizes the advantages of surface wave communication, including low loss, interference resistance, and energy efficiency, distinguishing it from conventional space wave-based communication systems. Moreover, the chapter explores potential application scenarios, offering in-depth discussions on outdoor communication utilizing reconfigurable intelligent surfaces, indoor communication incorporating enhanced security measures, and the conceptualization of NoC based on surface waves. And these scenarios highlight the potential diversity and substantial impact that surface wave communications can have in various application domains.

2.2 Zenneck Surface Wave

Zenneck surface wave (ZSW) is a type of surface waves that propagates along the interface between a metal-dielectric surface and free space. It is named after Jonathan Zenneck, who first derived the wave solution for this phenomenon on non-uniform surfaces in the late 19th century [17, 18]. ZSW exhibits the unique characteristic of tightly adhering to the surface, enabling stable and efficient propagation in a 2D plane [19, 4]. And then the definitions and derivations related to ZSW have be summarized in [20, 21]. It clarified the types of surface waves, including ZSW, which is supported by a specific metal-dielectric surface, also known as a coated dielectric conductor. ZSW is distinguished by its excitation mechanism, which involves electromagnetic excitation on the surface by space waves rather than antenna radiation or scattering directly, and its propagation in the transverse-magnetic (TM) mode along the propagation surface. And other types of surface waves may indeed exhibit different propagation modes, such as transverse-electric (TE) or hybrid modes. However, despite these variations in propagation modes, they still present similar propagation characteristics with ZSW. It is worth noting that ZSW demonstrates a remarkable ability to tightly propagate 2D surfaces as mentioned. The power distribution of surface waves near the surface, which can be referred to as tightness, is influenced by the impedance of its propagating surface. In general, a higher surface impedance serves to confine the ZSW more effectively, resulting in rapid attenuation of surface waves away from the surface vertically [22, 23, 24]. Unlike free space waves, ZSW, as a special solution of cylindrical waves, exhibits path loss that is directly proportional to the propagation distance d, rather than following the squared distance d^2 of free space waves. This indicates that utilizing ZSW as information carriers can significantly reduce path loss. However, in the previous century, researchers are limited by the lack of technical equipment to perform simulations or experiments, which led them to focus primarily on the excitation and propagation phenomena of surface waves, resulting in limited understanding of surface wave's applications.

In recent years, with the rapid development of communication technologies

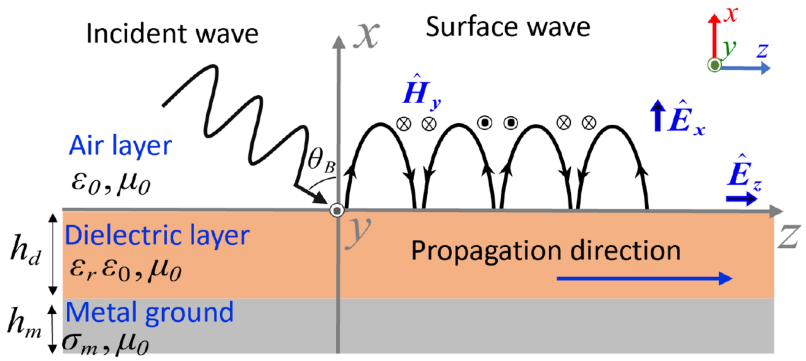

Figure 2.1: Illustration of surface wave excitation by the incident space wave with Brewster's angle of incidence on a dielectric-metal surface.

in various application scenarios such as NoC, wearable devices, and smart home devices, as well as the emergence of programmable metasurfaces, the exploration of surface waves has regained attention. And the increasing technology for precise control over the phase, amplitude, and propagation direction of electromagnetic waves has prompted the research of surface waves which have the potential to act as a more stable and promising information carrier.

For a systematic elucidation of surface waves, referred to as ZSW, in this thesis, Section 2.3 will further discuss the electromagnetic theory and propagation characteristics of surface waves [1]. Section 2.4 will highlight the advantages of surface waves, while Section 2.5 will delve into the relevant research efforts in this field. Lastly, Section 2.6 will explore potential application scenarios for surface waves.

2.3 Electromagnetic Theory and Propagation Characteristics

2.3.1 Field Strengths

The geometry of a flat dielectric-metal surface is illustrated in Fig. 2.1 from a front view. It consists of a dielectric layer on top and a metal ground layer at the bottom. Above the dielectric layer, an air layer is present, which can also be considered as a free space environment. The air layer has a permittivity of $\varepsilon_0 = 8.854 \times 10^{-12}\,\mathrm{F/m}$

[1] Later in this thesis, the term 'surface waves' is used instead of 'Zenneck surface wave' to facilitate the discussion of extensive research and applications based on surface waves.

and a permeability of $\mu_0 = 4\pi \times 10^{-7}\,\mathrm{H/m}$. In the dielectric layer, the thickness is represented by h_d and the relative permittivity by ε_r. And in the metal ground layer, the thickness is denoted as h_m and the electrical conductivity as σ_m. It is noted that the dielectric-metal surface is composed of non-magnetic materials, resulting in a magnetic permeability equivalent to μ_0.

From this front view, an interface $x-z$ plane is formed between the air and the dielectric-metal surface. When this surface is incident by the space wave parallel to the $x-z$ plane, originating from a transducer in an optically thinner medium, such as air in this example, at an incident angle equal to the Brewster's angle θ_B, the incident wave will be transferred to the surface wave and become "trapped" on the surface. And it will propagate along the surface in the $+z$-direction. For a detailed derivation of the excitation process of surface waves on the surface, please refer to Appendix A.1.

It can be seen that the magnetic field (H-field) $\hat{\boldsymbol{H}}_{\boldsymbol{y}}$ [2] of the excited surface wave is perpendicular to the incident $x-z$ plane, while the electric field (E-field) $\hat{\boldsymbol{E}}_{\boldsymbol{x}}$ and $\hat{\boldsymbol{E}}_{\boldsymbol{z}}$ are parallel to the incident plane. And the derivation of surface waves as cylindrical waves is obtained by solving the Bessel equation in [22]. By deriving the Maxwell's equations under the boundary conditions of a multi-layer structure, assuming that the incident wave is a normally attenuated plane wave, the field strength for the electromagnetic surface wave can be obtained as shown in (2.1) [21]. The derivation of the Maxwell's equations for these equations is provided in Appendix A.3.

$$\begin{cases} \hat{\boldsymbol{H}}_{\boldsymbol{y}} = \hat{\boldsymbol{y}} \dfrac{1}{\sqrt{d}} A e^{-\gamma_z z} e^{-\gamma_x x} e^{j\omega t} \\ \hat{\boldsymbol{E}}_{\boldsymbol{x}} = \hat{\boldsymbol{x}} \dfrac{\gamma_z}{\sqrt{d}\, j\omega\varepsilon_0} A e^{-\gamma_z z} e^{-\gamma_x x} e^{j\omega t} \\ \hat{\boldsymbol{E}}_{\boldsymbol{z}} = -\hat{\boldsymbol{z}} \dfrac{\gamma_x}{\sqrt{d}\, j\omega\varepsilon_0} A e^{-\gamma_z z} e^{-\gamma_x x} e^{j\omega t} \\ \gamma_x^2 + \gamma_z^2 = \gamma_0^2, \end{cases} \tag{2.1}$$

where $\hat{\boldsymbol{x}}$, $\hat{\boldsymbol{y}}$, and $\hat{\boldsymbol{z}}$ denote the unit vectors in the $+x$, $+y$, and $+z$-directions, respec-

[2] The bold symbols with a superscript are emphasized as direction vectors in this thesis.

tively. A is the amplitude constant, d is the propagation distance of the surface wave along the surface in the $+z$-directions, ω is the angular frequency, t is the time, γ_0 is the propagation coefficient in free space, γ_x and γ_z are the propagation coefficients of the surface wave in the $+x$ and $+z$-directions, respectively. And these propagation coefficients can be written as

$$\begin{cases} \gamma_0 = jk = j\omega\sqrt{\mu_0\varepsilon_0} \\ \gamma_x = \alpha_x + j\beta_x \\ \gamma_z = \alpha_z + j\beta_z \,, \end{cases} \tag{2.2}$$

where j is the imaginary unit, k is the wave number, α_x and α_z are the attenuation constants, and β_x and β_z are the phase constants in the corresponding directions, respectively, which can be given as

$$\begin{cases} \alpha_x = -\omega^2\mu_0\varepsilon_0\left[\dfrac{(\varepsilon_r - 1)}{\varepsilon_r}h_d + \dfrac{\Delta}{2}\right] \\ \beta_x = \omega^2\mu_0\varepsilon_0\dfrac{\Delta}{2} \\ \alpha_z = \left\{\dfrac{\sqrt{\left[\left(-\omega^2\mu_0\varepsilon_0 + \beta_x^2 - \alpha_x^2 - 2j\alpha_x\beta_x\right)^2 + \left(-\omega^2\mu_0\varepsilon_0 + \beta_x^2 - \alpha_x^2\right)^2\right]}}{2}\right\}^{\frac{1}{2}} \\ \beta_z = \left\{\dfrac{\sqrt{\left[\left(-\omega^2\mu_0\varepsilon_0 + \beta_x^2 - \alpha_x^2 - 2j\alpha_x\beta_x\right)^2 - \left(-\omega^2\mu_0\varepsilon_0 + \beta_x^2 - \alpha_x^2\right)^2\right]}}{2}\right\}^{\frac{1}{2}} , \end{cases} \tag{2.3}$$

where the attenuation constants α_x and α_z determine the rate at which the field strengths of the surface wave attenuate in the $+x$ and $+z$-directions with increasing distance. It can be observed that their values are affected by the relative permittivity ε_r and thickness h_d of the dielectric layer. Here, Δ represents the skin depth of the surface and can be written as

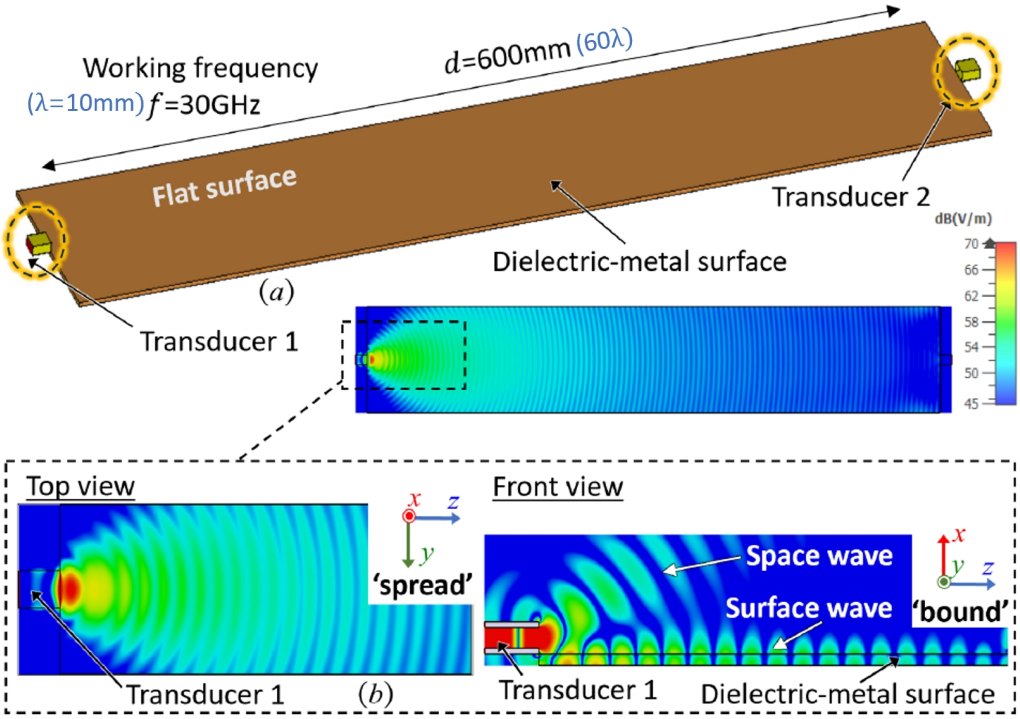

Figure 2.2: An example of (a) flat dielectric-metal surface with a propagation distance $d = 600\,\text{mm}$ and (b) its simulation results form the top view and front view at $30\,\text{GHz}$.

$$\Delta = \sqrt{\frac{2}{\omega \mu_0 \sigma_m}}. \tag{2.4}$$

In order to explain a clear depiction of the propagation process of the surface wave, Fig. 2.2 presents an illustrative example of a flat dielectric-metal surface along with its corresponding surface wave simulation results at a frequency of $30\,\text{GHz}$. This set of experiments is conducted at $30\,\text{GHz}$ with the wavelength $\lambda = 10\,\text{mm}$, and the propagation distance d is set to $600\,\text{mm}$. The relationship between the propagation distance and wavelength can be easily calculated. In the top view, it can be observed that the surface wave is excited by the space wave emitted from the transducer 1, referred to as a waveguide here, and then bound by the surface and propagates along the surface in the $+z$-direction towards the transducer 2, which serves as the receiving end. Furthermore, from the front view, it can be observed that both the surface wave and space wave coexist on the right-hand side of the transmitting end, transducer 1. This phenomenon can be addressed by design-

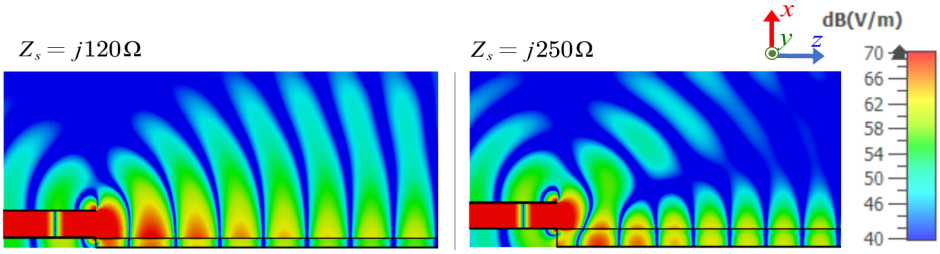

Figure 2.3: Two simulation examples of the flat dielectric-metal surfaces with surface impedance of $Z_s = j120\,\Omega$ and $j250\,\Omega$.

ing transducers that closely match the surface, thereby suppressing the divergence of space wave in the air layer and enhancing the excitation efficiency of surface wave [25]. And from the top view, it can be seen that the surface wave uniformly spreads across the entire surface. As discussed research motivations in Section 1.2, the presence of uncontrolled diffused surface wave reaching any receiving end on the propagation surface can result in significant multipath interference, thus degrading the quality of SWC. This issue will be further investigated in subsequent research conducted within this thesis.

2.3.2 Surface Impedance

The ability to confine surface wave on a propagation surface is determined by the surface impedance of the surface. It can be given as

$$\begin{aligned} Z_s &= R_s + jX_s \\ &= -\frac{E_z}{H_y} = \frac{\gamma_x}{j\omega\varepsilon_0} = w\mu_0\frac{\Delta}{2} + j\omega\mu_0\left[\frac{(\varepsilon_r - 1)}{\varepsilon_r}h_d + \frac{\Delta}{2}\right], \end{aligned} \tag{2.5}$$

where R_s is the surface reactive resistance as the real part of Z_s and X_s is the surface inductive reactance as the imaginary part of Z_s given by

$$X_s = \omega\mu_0\left[\frac{(\varepsilon_r - 1)}{\varepsilon_r}h_d + \frac{\Delta}{2}\right]. \tag{2.6}$$

For a detailed derivation of the excitation process of surface impedance, please refer to Appendix A.2.

From (2.3) and (2.6), it can be observed that a high inductive reactance re-

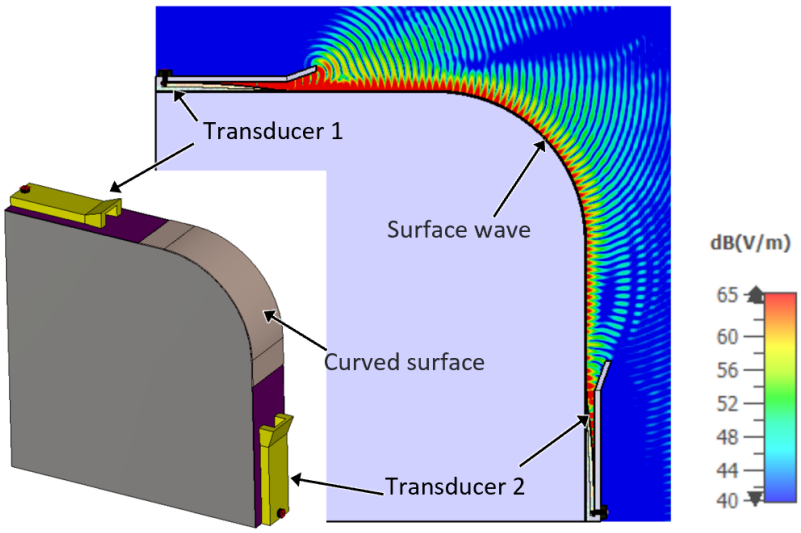

Figure 2.4: A example of surface wave propagating over a curved surface with 90° corner.

sults in a high attenuation constant α_x, indicating greater attenuation away from the surface in $+x$-direction. In other words, the surface wave becomes more tightly bound near the surface. The surface impedance can be adjusted by manipulating the relative permittivity ε_r and thickness h_d of the dielectric layer. Fig. 2.6 illustrates two simulation examples of flat dielectric-metal surfaces with different surface impedances of $Z_s = j120\,\Omega$ and $Z_s = j250\,\Omega$. It is evident that the surface wave is more bound on the surface with $Z_s = j250\,\Omega$ and dissipates more rapidly in the in $+x$-direction. Therefore, in practical applications, surfaces with high inductive reactance are preferred to reduce interference in the air layer in a 3D space. Additionally, high surface reactance can also be achieved through corrugated metal surfaces with periodic protrusions [21]. Nevertheless, for application scenarios in the millimeter-wave frequency band, coated dielectric-metal surfaces are easier to design and fabricate.

2.3.3 Various Propagation Surfaces

Another significant characteristic of surface waves is their ability to propagate over various surfaces, indicating that the surface does not need to be perfectly flat for transmission to occur. This greatly expands the design possibilities and application scenarios for SWC. Fig. 2.4 depicts the case of a curved surface, where the surface

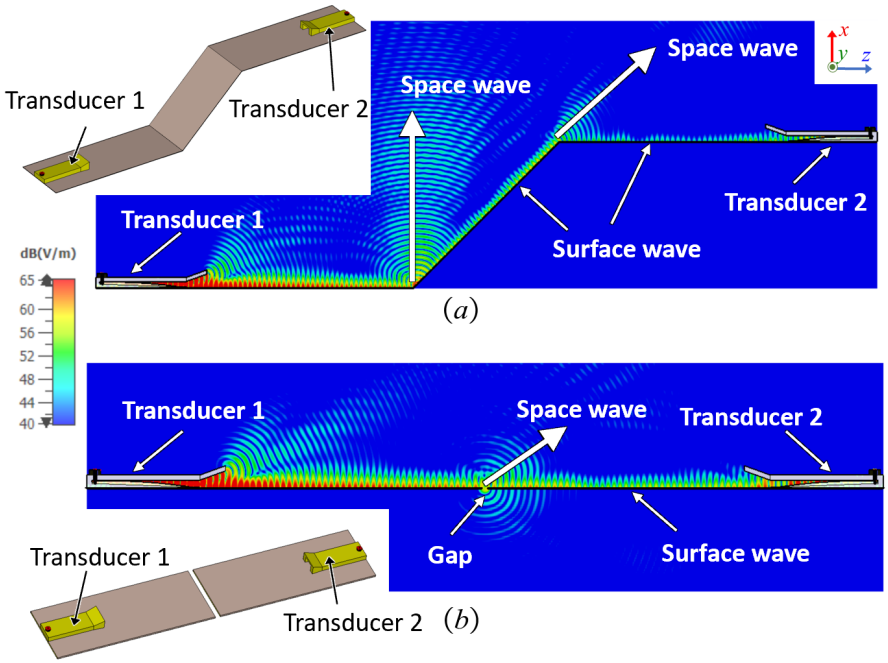

Figure 2.5: Two examples of surface waves propagating over (a) a surface with 45° sharp turns and (b) a surface with a gap.

wave continues to propagate smoothly around a 90° corner. The results demonstrate that even at the curved corner, the surface wave maintains significant radiated power. The prominent presence of space wave is caused by the sharp edge discontinuities on the relatively narrow surface. Furthermore, the surrounding space wave and reflected wave can be disregarded since the transducers are solely responsible for generating the surface wave.

And Fig. 2.5 (a) further demonstrates that surface wave propagation persists even with 45° sharp turns on the surface, although these turns introduce additional space wave. In practical applications, angled surfaces can be utilized to generate the required space wave for reaching user equipment located away from the surface. Additionally, surface wave exhibit remarkable resilience to gaps on the surface, even when installed in outdoor environments. Fig. 2.5 (b) investigates this scenario and examines the impact on surface wave propagation. It is evident that the gap introduces discontinuities and it leads to the emission of space wave, with larger gaps resulting in a greater amount of space wave. However, the surface wave is still able to bridge the gap and continue gliding along the surface. These findings

highlight the robust connectivity of surface wave and their practicality in practical application scenarios.

2.4 Advantages of Surface Wave Communications

Based on the aforementioned theoretical understanding and propagation characteristics of surface waves, several advantages of SWC can be summarized when surface waves are utilized as the information carrier compared to traditional wireless communication. It is worth noting that this section primarily focuses on discussing the advantages and potential of surface waves. Limitations and challenges related to surface waves and SWC, as well as the strategies employed to address them, are listed in Section 6.2.1.

Low loss: Surface waves exhibit lower attenuation compared to traditional communication based on space waves as the propagation distance increases. Additionally, they do not experience selective fading like space waves in free space due to environmental factors. This characteristic enables surface waves to maintain high transmission quality over long distances.

Energy efficiency: Surface waves can achieve signal transmission with lower energy consumption. By utilizing the 2D surface of the medium for signal transmission, SWC can reduce the energy losses incurred by 3D propagation in the air. This has the potential to optimize energy consumption for battery-powered mobile devices and wireless sensor networks.

Reduced signal interference: SWC has the potential to mitigate signal interference encountered during the surface wave propagation process through further optimization design. Simultaneously, it can reduce susceptibility to surrounding electromagnetic interference in 3D environment since it is based on 2D plate. This provides SWC with robust resistance to interference, enabling more reliable and stable communication connections.

Expanded propagation medium: Surface waves can propagate on various surfaces, including curved surfaces, gapped surfaces, and more. Despite the discontinuities in the propagation surfaces, surface waves can still propagate and continue

sliding along the surface. This greatly expands the versatility of propagation surfaces. Therefore, surface waves have the potential to utilize discontinuous surfaces such as the ground or walls as the transmission medium, making them applicable in practical scenarios such as NLOS communication between indoor and outdoor environments.

By leveraging these advantages, SWC demonstrates great potential in various application scenarios and they will be further discussed subsequently.

2.5 Related Works

The previous sections have addressed several fundamental propagation characteristics of surface waves, emphasizing their advantageous features such as low loss and minimal signal interference. In recent years, the promising applications of surface waves in communication, sensing, and optics have garnered increasing interest and attention among researchers [3]. Consequently, there has been a growing emphasis on the manipulation and control of surface wave propagation. Drawing upon the existing knowledge and research accomplishments, this section aims to present recent advancements in the field of manipulating surface waves.

In the early stages of research, surface waves were investigated in different types of propagation surfaces, including flat surfaces [22], corrugated surfaces [21], elastic surfaces [26], step surfaces [27], and curved surfaces [1], etc., as mentioned in Section 2.3.3. When considering non-flat surfaces, the analysis of surface wave propagation encompasses not only the inherent characteristics of propagation but also the influences of surface irregularities. This is due to the fact that non-directed wavefronts impinging on uneven surfaces result in phenomena such as reflection and scattering, which impact the propagation, magnitude, and phase of surface waves [28, 29, 30]. These findings provide the theoretical groundwork for further designing intricate surface structures aimed at manipulating surface waves. By judiciously selecting appropriate surface structures tailored to specific application scenarios, the propagation performance of surface waves can be enhanced, effectively meeting the communication requirements of targeted applications.

Metasurfaces have emerged as a prominent research direction for manipulating surface waves. In the microwave frequency band, metasurfaces are designed with subwavelength structured units to control the interaction between incident electromagnetic waves and surface waves, thereby enabling precise control over surface wave propagation. The subwavelength units of metasurfaces provide the capability to manipulate important parameters such as phase, amplitude, and polarization, which play a crucial role in determining the propagation direction, scattering behavior, and refraction characteristics of surface waves [31, 32, 33]. For instance, in the case of a chessboard metasurface composed of complementary metallic patches, modifying the connectivity of the patches can establish predetermined pathways for guiding surface wave propagation [5, 34]. Chessboard metasurfaces can also exploit dual resonances and surface wave suppression properties to reduce the broadband radar cross-section, allowing for partial energy coupling of incident waves into surface waves and mitigating electromagnetic wave reflection, which holds potential for stealth applications [6, 35].

Furthermore, both isotropic and anisotropic metasurfaces offer means to manipulate surface waves [36, 37, 38]. Anisotropic metasurfaces, employing specific materials, can effectively minimize the scattering losses of surface waves occurring at sharp angles in physical environments [39, 40]. On the other hand, isotropic periodic metasurfaces printed on grounded dielectric substrates enable nearly perfect conversion of incident space waves into surface waves [41, 42, 7]. Additionally, by controlling the surface properties, it becomes possible to achieve perfect conversion from TM surface waves to TM leaky waves, which holds promise for the realization of ideal leaky wave antennas and similar devices [43].

Conversely, metasurfaces can also be employed to convert surface waves into space waves [44]. Moreover, 3D frequency-selective surfaces with periodic rectangular frameworks can be used as planar filters for surface waves, effectively restricting the transmission channels of surface waves. This structure supports the propagation of parallel-polarized surface waves in specific channels within a desired frequency range, exhibiting excellent band-pass frequency response [45]. There-

fore, it can be seen that metasurfaces offer significant potential for achieving directed propagation, suppressing scattering, transforming wave characteristics, and enabling frequency selectivity of surface waves. Their applications span various domains, including communication, radar, and antenna systems.

Another research direction involves the utilization of metasurfaces as auxiliary devices to enhance the transmission performance of surface waves. Reconfigurable intelligent surfaces (RIS) have garnered significant attention, showcasing their potential in the context of sixth-generation (6G) mobile communications [46, 47, 48]. Serving as programmable propagation medium, RIS not only augment signals through reflection but also function as intelligent beamformers, directing signals towards specific receiving devices to improve signal quality and transmission efficiency [49, 50, 51]. Moreover, RIS deployment costs are relatively low, while exhibiting remarkable coverage performance [52, 53]. The reconfigurability of RIS presents novel opportunities for its application in surface wave scenarios. On one hand, RIS can serve as a programmable propagation medium, thereby mitigating path loss and enabling more controllable communication. It enables the adjustment of surface wave propagation directions, optimization of signal transmission paths, and enhancement of coverage range and transmission rates. On the other hand, RIS can function as an intelligent reflective beamformer, dynamically adjusting the direction and phase of surface waves to facilitate their directed propagation and improve transmission efficiency [1, 2]. RIS, in synergy with surface waves, can be flexibly deployed across diverse environments, including urban building walls, indoor desktops, and various other application scenarios. This flexibility empowers wireless communication systems with multiple options for deployment and coverage. Leveraging intelligence and reconfigurability, RIS can dynamically configure and optimize the propagation direction of surface waves, adapting to different channel conditions and user requirements, as elaborated in Section 2.6.

Surface waves can also be employed in the design of metasurface antennas that interact with surface waves [54, 55]. Among these, the most common are leaky wave antennas at millimeter wave (mmWave) implemented by printing elec-

tric patches or slotting on a planar grounded dielectric substrate [56, 57, 58, 59]. In such antennas, surface waves serve as the radiation mechanism for leaky waves. Leaky wave antennas are typically designed with slots in the top dielectric layer to radiate signals in one direction while minimizing radiation in other directions. And the slot varies spatially to achieve the desired customized leaky wave effects. In certain applications, the signal radiated by the antenna can leak through the dielectric layer and propagate in the form of surface waves along the surface of the dielectric. By incorporating specific slot designs in the dielectric layer, the generation and direction of surface wave propagation can be controlled in the physical structure. Furthermore, this design allows surface waves to radiate into free space as space wave. [60, 61]. Therefore, Leaky wave antennas enables control over surface waves at certain directions, and also make the adjustment of surface wave dispersion characteristics [62] and directional gain [63, 64].

Additionally, leaky wave antennas can be guided by integrating them with substrate-integrated waveguides (SIW) [65, 66] or embedding them within the surface, forming structures such as surface wave horn antennas. These antennas radiate at the transmitter end, allowing leaky wave antennas to function as independent units and expand their application domains [67]. The integration of surface waves and leaky wave antennas through this design approach enables more flexible and efficient electromagnetic wave radiation and beam control. In a traditional sense, SIW represents a waveguide design technological approach. It realizes the amalgamation of microstrip lines and waveguides through the creation of a structured waveguide on the substrate of a microwave circuit [68, 69, 70]. This diverges distinctly from gap waveguide technology, characterized as a gap waveguide methodology that introduces intricate structures within the interstitial space between two conductor plates, thereby facilitating the transmission of guided waves [71, 72]. In comparison to the two technologies above, the modification of the substrate structure in SIW holds greater potential for conceptualization as a platform facilitating the propagation of surface waves. Its intrinsic potential lies in drawing inspiration from the internal design principles of SIW and utilizing them to internally guide

these surface waves.

Furthermore, surface wave fluid antennas have emerged as a new type of antenna design based on the principles of surface wave propagation and fluid control [73, 74]. These antennas exploit the characteristics of fluid material and the propagation mechanism of surface waves to achieve the radiation and control of electromagnetic waves. In surface wave fluid antennas, fluid material are used as the radiating medium, replacing traditional solid materials. By introducing specific structures or fine-tuning the properties of the fluid medium's surface, the excitation and control of surface waves can be achieved. These structures can be periodic, directive, or specially designed to generate the desired radiation effects and beam characteristics [75].

In the high-frequency mmWave and optical spectrum, the study of surface waves has also attracted extensive interest. In the field of high-frequency, surface waves are commonly known as surface plasmon polaritons (SPPs), which arise from the coupling between electromagnetic waves and the interface of metal surfaces or metal nanostructures, and it itself is also a coupling of electromagnetic waves and plasmonic waves [76, 16]. It should be noted, as discussed in 2.2, the ZSW can propagate on both conductive and non-conductive surfaces, while SPP primarily occurs on the surface of conductive materials, typically metals. When considering structural design and control of surface waves in dielectric layers, the primary focus remains on ZSW. The control and utilization of surface waves in the optical spectrum can be achieved through specific surface structures and control methods [77, 78]. For instance, spatiotemporal modulated metasurfaces have been proposed to achieve nonreciprocal beam control, where incident light beams are reflected into forward-scattered far-field radiation and backward-scattered into near-field surface waves [79, 80]. Additionally, embedding a parabolic reflector redirects surface leaky waves into forward waves, enhancing the bandwidth of holograms and enabling wideband beam scanning [81, 82, 83, 84, 85]. These techniques offer new possibilities for directional control and broadband applications of optical waves. On the other hand, in the optical frequency range, transformation optics [86, 87] and

stacked Eaton lenses [88, 89, 90] have been utilized to control the characteristics of surface waves. By manipulating refraction in the terahertz regime, these approaches enable directional control and focusing effects of optical waves, providing new solutions for imaging and optical communication applications [91, 92]. Moreover, surface waves find potential applications in flexible transient photonics and surface wave biosensors. Flexible transient photonics exploit the transmission properties of surface waves on curved and deformable materials, enabling the development of flexible and stretchable photonic devices [93]. Surface wave biosensors utilize the sensitivity of surface waves to the interaction between metal surfaces and biological molecules, facilitating highly sensitive detection and analysis of biomolecules [94]. These studies on surface waves open up new avenues for innovation and applications in the field of optics, with potential implications in optical communication and biomedical research.

In recent years, there has been a notable increase in the widespread application of surface waves in various domains. In network-on-chip systems, surface waves have been proposed as a viable option for high-speed communication and data transmission. By incorporating miniature antenna units on chips, surface waves can be excited and propagated on the substrate, enabling the establishment of flexible node-to-node transmission paths [9, 10, 95, 96]. Surface waves find utility in wireless communication and sensing in wearable devices and body networks. Placing surface wave antennas on wearable devices or the human body's surface facilitates the transmission and reception of information between the body surface and the surrounding environment [11, 12, 97]. These applications offer novel solutions for intelligent health monitoring, the Internet of Things, and personal communication. The emergence of surface wave fluid antennas as a novel antenna technology, which combines fluid metal with surface waves, is noteworthy. By controlling the properties and flow state of the fluid medium, surface waves can be excited, manipulated, and radiated, thereby expanding the functionality and scope of antenna applications [13, 14]. This antenna technology holds potential for applications in communication, radar, and wireless sensing domains. Moreover, in industrial environments,

surface waves are being explored as an alternative to cables to reduce the overall lifecycle costs. Leveraging surface waves for signal and energy transmission in industrial equipment and systems can diminish the usage and maintenance costs associated with cables while enhancing system reliability and flexibility [15].

To summarize, the control and manipulation of surface waves through metasurfaces or reconfigurable surfaces enable the regulation of their propagation characteristics, transmission paths, and radiation effects, thereby expanding their applications in communication, sensing, optics, and other fields. These studies provide new insights and solutions for future wireless communication systems, antenna designs, and optical applications.

2.6 Potential Application Scenarios

2.6.1 Outdoor Communication with Reconfigurable Intelligent Surface

One potential application scenario for surface waves is their use as carriers for outdoor communication along walls, as demonstrated in Fig. 2.6. This innovative scheme, where surface waves and RIS collaborate, distinguishes itself from the prevailing focus on passive RIS. When the base station emits space waves that reach the RIS-installed wall, two propagation modes are expected to emerge. On the one hand, the RIS can act as a reflective surface, manipulating the space wave's reflection direction for direct reception at the user receiver (illustrated by the blue line). On the other hand, by seamless switching, the RIS can convert the space waves into surface waves, which then propagate along the RIS-installed wall, resulting in a reduced path loss significantly. And surface waves can exhibit strong adherence to the wall as above sections mentioned, causing significant attenuation of waves away from the wall. Therefore, the interference from the surrounding air will be considerably diminished and the possible interference concerns predominantly confined to close proximity to the wall. And then, the RIS is expected to re-emit the wave to reach the user receiver (illustrated by the black line). The simultaneous application of these two propagation modes, combining the utilization of space waves and

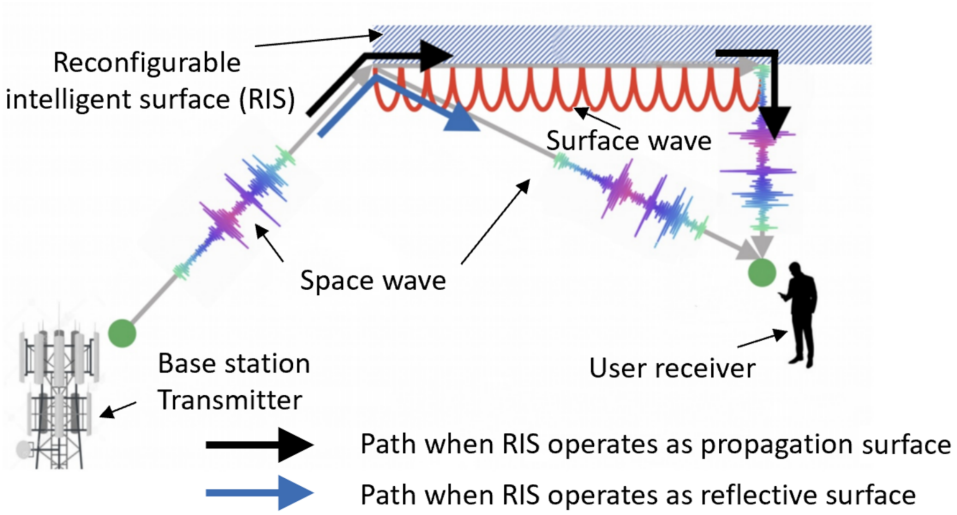

Figure 2.6: A communication scheme utilizing RIS-installed walls acting as both a reflective surface and a propagation surface, to enable seamless switching between space wave and surface wave propagation modes in outdoor environments [1].

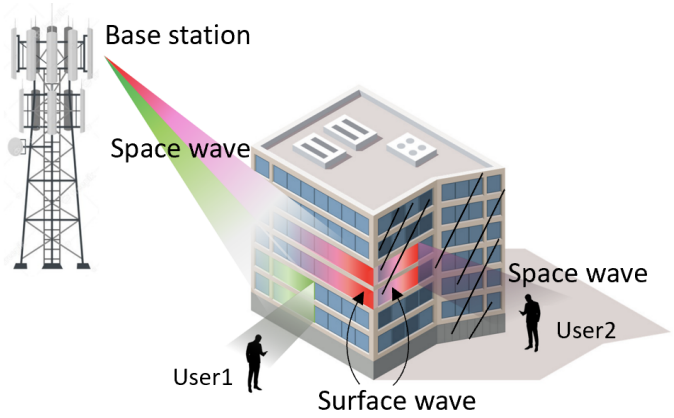

Figure 2.7: An architectural model featuring RIS-installed walls to achieve NLOS communication and multi-user communication [1].

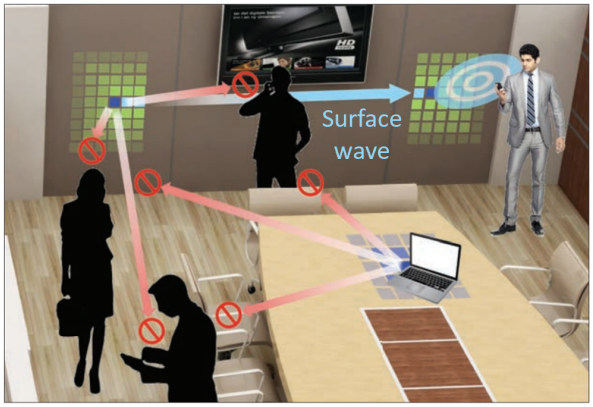

Figure 2.8: The deployment of RIS on indoor walls and desktops to achieve secure communication indoors [2].

surface waves, can enhance signal strength effectively at the user receiver.

And Fig. 2.7 showcases an architectural model featuring RIS-installed walls in outdoor environments. In scenarios where multiple user receivers are in close proximity to the building walls, space waves from the base station reach the wall, propagate along its length as the surface waves, and then emerge to reach user 1. Simultaneously, surface waves can traverse discontinuous walls to reach the backside of the building, propagating along the back wall to reach user 2. By circumventing obstacles and overcoming line-of-sight limitations, this approach will empower the reliable NLOS communication. Furthermore, this communication scheme also facilitates multi-user communications on the same time-frequency resource by partitioning their signals, resulting in expanded communication coverage and enhanced reliability in complex scenarios.

2.6.2 Indoor Communication and Secure Transmission

In existing indoor smart communication solutions, communications relying on space waves often unintentionally occupies the entire indoor space, as space waves naturally propagate and disperse in various directions. And along different propagation pathways, the reflection and diffraction of space wave from objects further complicate interference patterns. In contrast, the utilization of surface waves will offer a more simplified solution by confining signals primarily to the surface and

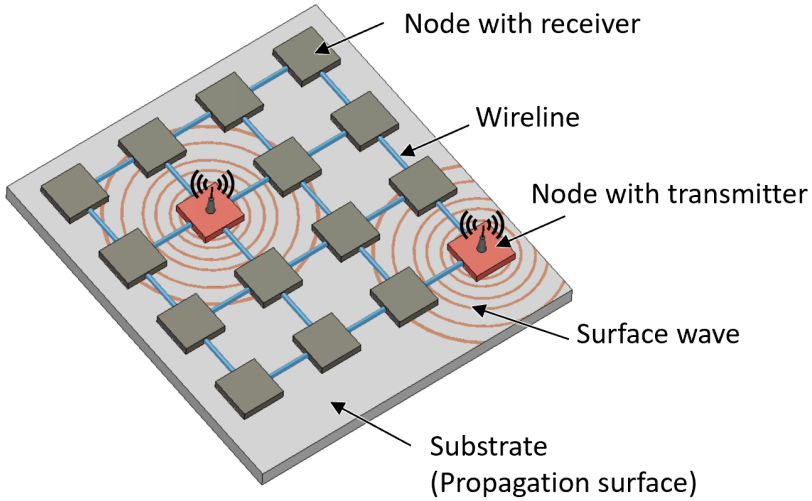

Figure 2.9: A surface wave-based hybrid wired NoC to improve energy efficiency.

providing more predictable behavior. Fig. 2.8 illustrates the deployment of RIS on indoor walls and desktops indoors. And numerous miniature antennas can be deployed on these surfaces and devices, enabling directional control of signals emitted by transmitters towards multiple indoor surfaces. By localizing all users relative to the RIS infrastructure, optimal and efficient communication paths can be determined in this system.

This approach can significantly reduce the distance between surfaces with transmitters and receiving users, while directional propagation of surface waves can also minimize vulnerability to interference indoors. Furthermore, this communication scheme can enhance security by containing signals within close proximity to the users, establishing secure zones. Notably, the reduced wireless communication distance associated with surface waves allows for lower transmission power, posing greater challenges for eavesdroppers at a distance.

2.6.3 Network-on-Chip Based on Surface Waves

In small size application scenarios, Fig. 2.9 illustrates a surface wave-based hybrid wired NoC, which offers a potential alternative solution to address the scalability and performance limitations inherent in traditional wired NoC systems. Conventionally, wireline transmission is employed in NoC for information transfer, but

this approach demands significant wired signal transmissions accompanied by additional thermal loss to ensure communication reliability, thereby amplifying the overall power consumption of the system. To mitigate this challenge, the surface wave-based hybrid wired NoC integrates miniature single oscillator antennas at specific transmitter nodes, generating surface waves that propagate within a 2D substrate. When two distant on-chip nodes necessitate communication, they can bypass multiple wired interconnects and directly transmit information through surface waves, establishing direct communication with remotely configured receiving nodes. This scheme of transmission not only markedly diminishes power consumption but also reduces dependence on intricate wired network architectures and routing algorithms, ultimately augmenting system scalability and performance. Consequently, the utilization of surface waves opens new avenues for the advancement of NoC architecture.

2.7 Conclusions

The low-loss and interference-resistant propagation characteristics of surface waves make them a promising carrier for highly intelligent wireless communication systems, potentially addressing the challenges posed by complex channel environments and massive device connectivity. Compared to traditional wireless communication, surface waves present stable propagation near the surface closely, expanding the application scenarios of SWC. They are expected to work with RIS in new intelligent communication environments such as outdoor NLOS communication, indoor communication, and NoC architectures. In these scenarios, surface architectures play a crucial role in dynamically controlling the propagation pathways on the surface. This allows for flexible selections of transmitting and receiving nodes while reducing surface wave crosstalk. Recent research has demonstrated the feasibility of designing internal or on-chip structures on the surface architecture to manipulate surface waves, which is an exciting development. However, the demand for reconfigurable propagation pathways requires dynamic or digital control of surface waves through adjusting surface structure instantaneously. This also adds to the challenges

of further considering complexity and flexibility on the surface.

Chapter 3

Reconfigurable Surface Wave Platform and Mathematical Model

3.1 Introduction

This chapter is dedicated to discussing a novel reconfigurable surface wave platform, with a focus on its geometric structure, working mechanism, and the mathematical model used to analyze its propagation characteristics. The platform introduces a porous architecture that enables dynamic manipulation and control of surface wave propagation pathways. To enhance adaptability and flexibility in complex communication environments, the platform also incorporates fluid metal and microfluidics techniques. The mathematical analysis model considers multiple surface wave rays following different paths and accounts for scenarios involving multiple reflections and transmissions at the wall. It provides expressions for the cumulative field strength within and beyond the metal wall pathway at specific measurement points on the surface. To validate the effectiveness of the model, the theoretical values obtained from the mathematical calculations are compared with the corresponding simulation values. By utilizing this model, it becomes possible to predict signal attenuation in both short and long-distance transmission scenarios on the platform. Furthermore, the study investigates the influence of surface materials, metal wall material, pathway width on the propagation characteristics.

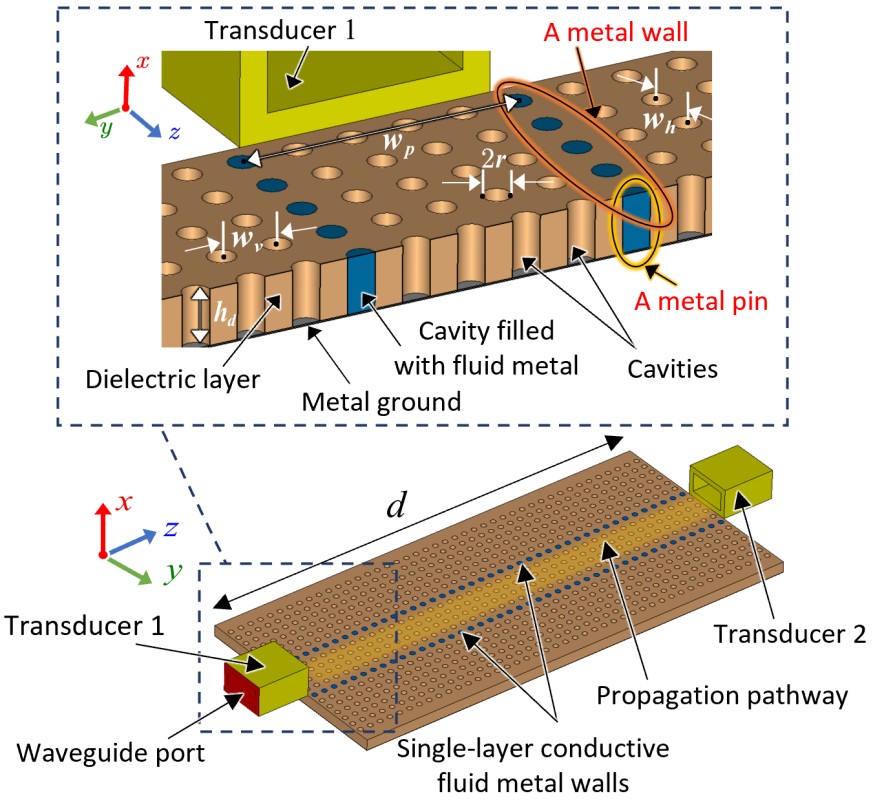

Figure 3.1: A reconfigurable surface wave platform with evenly distributed cavities that can be filled with conductive fluid metal.

3.2 Reconfigurable Surface Wave Platform

3.2.1 The Proposed Surface Geometry

A proposed reconfigurable surface wave platform, designed to create dynamically directed propagation pathways, is illustrated in Fig. 3.1. The platform consists of a porous structure comprising a top dielectric layer firmly adhered to a conductive metal ground. The dielectric layer is characterized by small-sized cylindrical cavities uniformly distributed across a 2D surface, with each cavity having a radius of r and a height of h_d. Notably, the height of the cylindrical cavities matches that of the dielectric layer. The spatial arrangement of the cavities is determined by the distances denoted as w_h and w_v, which represent the separation of the center points in the horizontal and vertical direction, respectively.

To guide and isolate surface waves, conductive fluid metal is utilized to fill the

cavities from the bottom of the metal ground. A cavity filled with fluid metal is referred to as a "metal pin," and a column of pins forms a metal "wall" within the dielectric layer. By forming two columns of metal walls, a dedicated propagation pathway is created with a pathway width denoted as w_p, representing the distance between the two metal walls. It is important to note that the term "wall" here does not indicate a physical structure protruding from the top of the dielectric surface. Thus, after the liquid metal fills the cavities and forms the metal walls, the entire dielectric surface remains flat without any protrusions. This allows for the flexible placement of electrical elements, such as transducers, on the surface without disrupting the formation of dynamic pathways within the dielectric layer by fluid metal. This significantly increases the flexibility in the positioning of the transmitting and receiving ends in the physical environment, which will be discussed in Section 4.3. And fluid metal exhibits low adhesiveness and high fluidity and will be described in in Section 3.2.3. Furthermore, this surface platform also suggests that this surface has the potential to work in synergy with other electric elements. For instance, the compact-sized reflection units in RIS can be embedded on the upper layer of the surface to capture and release space waves at arbitrary angles into the surface, as discussed scenarios in Section 2.6. It also can be seen that two transducers are positioned at opposite ends of the pathway to emit and receive surface wave. This configuration forms the fundamental structure for the directed propagation of surface wave along the pathway.

In fact, as confirmed by simulation results, the pin structures guiding surface waves can adopt uniform rectangles, circles, or other regular shapes, and even irregular forms, showcasing a high degree of flexibility. The preference for circular pins is mainly because arranging them in the laboratory environment allows for versatile combinations, as described in Section 4.3. Furthermore, as discussed in Section 2.5, the design of the cavity draws inspiration from the internal design principles of SIW and utilizes them to internally guide surface waves. In traditional SIW, there is a classical design approach. Due to the discontinuity of SIW's vertical walls, radiation leakage may potentially flow between the through-cavities. Therefore, it is

crucial to determine the geometric proportions of the through-cavities to minimize leakage and ensure overall transmission quality [70]. Considering that the metal pins with the diameter $2r$ needs to mimic the behavior of a continuous metal wall, and in comparison to the diameter, the spacing w_v and w_h between the through-cavities must be kept relatively small (assuming it is a uniform porous surface, $w_v = w_h$). The diameter should be smaller than the wavelength λ of the operating frequency, and a validated empirical formula for this adjustment is as follows [69]:

$$\begin{cases} w_v \text{ and } w_h \ \leq 4r \\ 2r \leq \dfrac{\lambda}{5}. \end{cases} \tag{3.1}$$

In designing the cavity structure for this thesis, it primarily referred to the regularities of this formula. Simulation results indicate minimal leakage waves, almost negligible, validating the formula's appropriateness in the context of surface waves. It is worth noting that although SIW provides inspiration for the design of cavity, such a porous structure confines surface waves within pathways composed of metal pins. However, the propagation and attenuation characteristics of surface waves differ from those guided by SIW. The most fundamental difference lies in the fact that electromagnetic waves in SIW are confined to transmit within the SIW structure, with both upper and lower layers being metallic. In contrast, surface waves propagate along the open surface of the dielectric layer. Additionally, surface waves are radiative, even though they rapidly attenuate in the direction perpendicular to the surface. Moreover, as cylindrical waves, the attenuation mechanism of surface waves differs from normal spherical waves, as demonstrated in Appendices A.1. And the decay, field strength and propagation pathway characteristics of surface waves will be elaborately discussed in subsequent sections. As for other surface parameters, such as dielectric height h_d and pathway width w_p, each of these factors influences the propagation of surface waves. They will be further discussed.

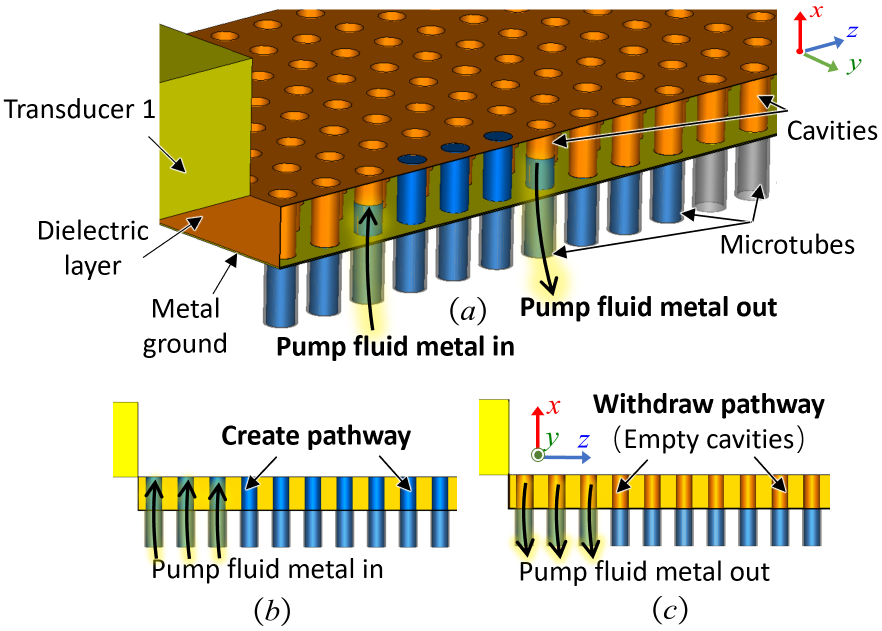

Figure 3.2: Illustration of the working mechanism of the proposed reconfigurable surface: (a) The fluid metal is pumped in or out of the cavities from the bottom adhesive microtubes to (b) create or (c) withdraw the dedicated surface wave pathway.

3.2.2 Working Mechanisms

Fig. 3.2 illustrates the working mechanism of the proposed reconfigurable surface platform, showcasing its flexibility in guiding surface wave propagation. The porous surface features cavities extending from the dielectric layer to the metal ground, with interconnected microtubes located at the bottom, as depicted in Fig. 3.2(a). Selected microtubes are employed for the controlled introduction of conductive fluid metal into the corresponding cavities, dynamically filling within the dielectric layer. To demonstrate the creation of a pathway, Fig. 3.2(b) exemplifies the simultaneous filling of a columnar arrangement of cavities with conductive fluid metal, resulting in the formation of a coherent columnar metal wall. Concurrently, the remaining cavities, except for those explicitly designated for pathway creation, remain unoccupied. Surface waves subsequently propagate along the pathway through internal reflections from the two columns of metal walls, effectively guided by this pathway configuration. Conversely, Fig. 3.2(c) illustrates the pathway's withdrawal by systematically pumping the fluid metal out of the cavities via

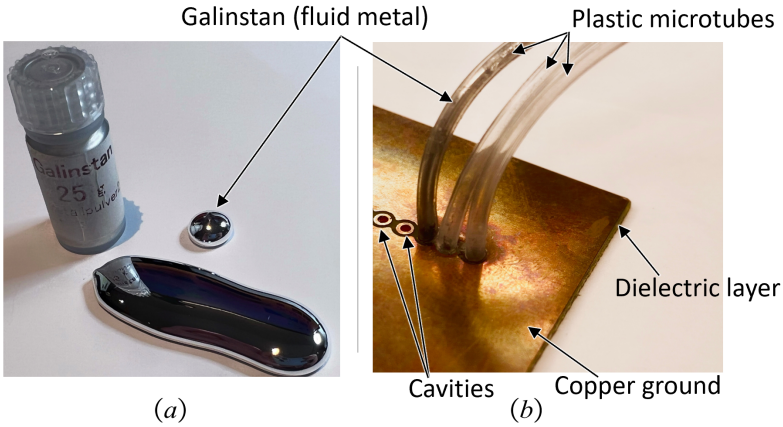

Figure 3.3: A sample of (a) conductive fluid metal, Galinstan, and (b) its use in a surface prototype.

the microtubes. This approach enables the creation of diverse surface wave propagation pathways by arranging fluid metal pins in columnar configurations, facilitating the formation of cohesive fluid metal walls. Such flexibility holds promise for various applications in the field of surface wave manipulation.

3.2.3 Fluid Metal and Galinstan

As introduced above, this reconfigurable surface utilizes fluid metal to create dynamic pathways. Fluid metal offers several advantages due to its low melting point, including excellent thermal and electrical conductivity, low adhesiveness, and high fluidity [98]. These properties make it suitable for a wide range of applications such as flexible electronics [99], wearable electronics [100] and fluid pumps [101]. Fig. 3.3(a) provides an example of Galinstan (a type of fluid metal alloy composed of gallium, indium, and tin) exhibiting a fluid state and good electrical conductivity $\sigma_g = 3.46\times10^6$ S/m at room temperature. And Table 3.1 from [102] presents a comparison of different materials at room temperature. It is evident that Galinstan possesses the advantages of both high electrical conductivity and a low freezing point. Additionally, when compared to other liquid metals, Galinstan exhibits several advantages for laboratory use. In comparison to mercury and mercury-containing alloys, Galinstan is characterized by low toxicity. Relative to sodium-potassium alloys, Galinstan is more stable and less sensitive to air and water, demonstrating

Table 3.1: Comparison of different materials. All measures at room temperature (Eutectic Gallium-Indium (EGaIn) is a homogeneous alloy that consists of approximately 25% indium and 75% gallium)

Non-Metallic	ε_r	**Freezing point** (C)
Water	78	0
Salt water (5%)	65	-2.5
Water 5% ethanol	77	-3
Metallic	**Conductivity** (S/m)	**Freezing point** (C)
Mercury	10^6	-39
eGain	3.42×10^6	16
Galinstan	3.46×10^6	-19

excellent oxidation resistance. In comparison to other fluid metals containing lead and thallium, Galinstan significantly reduces potential environmental and health risks.

In summary, Galinstan strikes a balance between electrical conductivity and malleability. Subsequent analyses in this thesis will utilize Galinstan as a representative case study for fluid metals. As depicted in Figure 3.3(b), this thesis envisions introducing Galinstan into the plastic microtubes of a porous surface prototype and controlling the Galinstan to flow within a physical environment.

3.2.4 Microfluidics and Pumps

Furthermore, as shown in Fig. 3.4 (a), the reconfigurable surface integrated with fluid metal is expected to be operated in combination with a multichannel programmable pump. They are connected via microtubes that are filled with fluid metal. By applying microfluidic technology, precise manipulation and control of small volumes of fluid metal at the microscale can be achieved [103]. By adjusting the flow rate and pressure of the pump, dynamic control of the fluid metal entering and exiting the cavity can be achieved. And then through the design of multiple channels, precise delivery and distribution of the fluid metal into multiple distinct cavities can be realized, enabling dynamic adjustments of the metal wall in a reconfigurable surface. Fig. 3.4 (b) illustrates two examples of a multichannel peristaltic programmable pump [104] and a syringe pump [105]. These multichannel pumps allow for simultaneous control of fluid delivery in multiple channels.

Table 3.2 [104] provides the characteristics of a commercial multichannel peri-

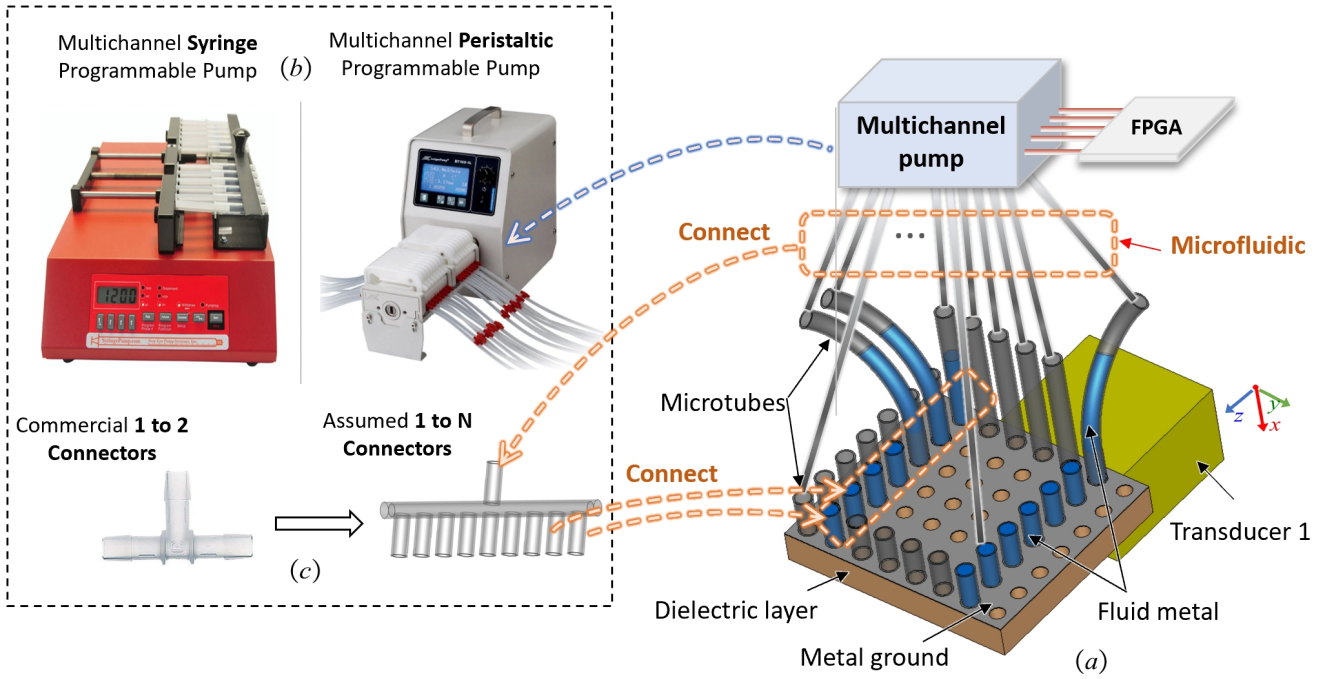

Figure 3.4: (a) The combined operation of the reconfigurable surface and microfluidics involves the use of flow-controlling fluid metal between a multichannel pump and microtubes located at the bottom of the surface. (b) Two examples of multichannel peristaltic programmable pump and syringe pump and (c) the microtube connectors.

Table 3.2: The characteristics of a commercial multichannel peristaltic programmable pump (Darwin Microfluidics: YZ1515X-A)

Characteristics	**Multichannel pump**
Flow rates	2 µL/min to 366.7 mL/min
Flow control and resolution	Digital operation
Channel	Up to 24 simultaneously
Graphic LCD	Control pump parameters and running state
Power supply	AC 110V 50/60Hz or AC 220V 50/60Hz
Power consumption	< 50W
Tubing compatibility	Can be compatible with multi-dimensional channels
Silicone Microtubes	Optional inside and outside diameters, the inner diameter can reach 0.5mm

staltic programmable pump (Darwin Microfluidics: YZ1515X-A). This pump offers programmable operation modes and parameter settings. For instance, flow rates can be set from $2\,\mathrm{L/min}$ to $366.7\,\mathrm{L/min}$, and it can maintain up to 24 channels simultaneously. In the envisioned scenario, these channels, i.e., Silicone microtube interfaces, as shown in Fig. 3.4 (c), connect to an ideal 1 to N Silicone connector. This connector links to one column of cavities on the porous surface. By connecting every two channels to the connector by microtubes, the system can control the flow of fluid metals into two columns of cavities, influencing the generation of a surface wave propagation pathway.

A recent research [14] introduces novel adaptive strategies with fluids. In this approach, non-metallic solutions (typically ionic water or electrolytes) are injected at both ends of a short segment of fluid metal. Additional direct current circuits are applied at the ends to generate signals controlling the position of the metal within the microtube. This method inspires the possibility of controlling the propagation pathway with electrical signals. To achieve this, connecting the programmable pump to a field-programmable gate array (FPGA) [106], a programmable logic device, can convert the desired pathway into digital signals to control the pump's channels. However, research on microfluidics and digital pumps is a complex and ongoing process. The methods described in this section are in the early stages and require further exploration. The subsequent chapters of this thesis will focus on the structural aspects of reconfigurable surfaces and the electromagnetic properties

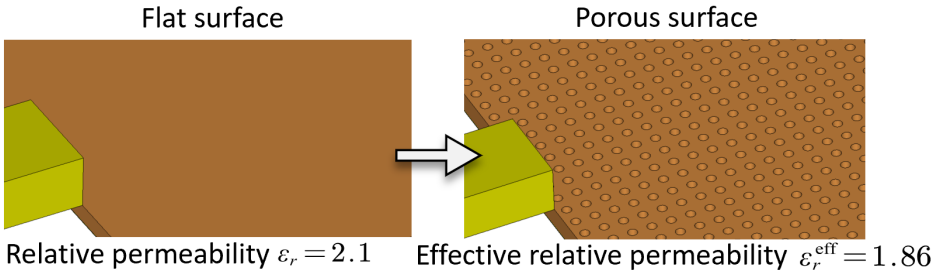

Figure 3.5: The transformation from the flat surface to the porous surface by introducing even cavities.

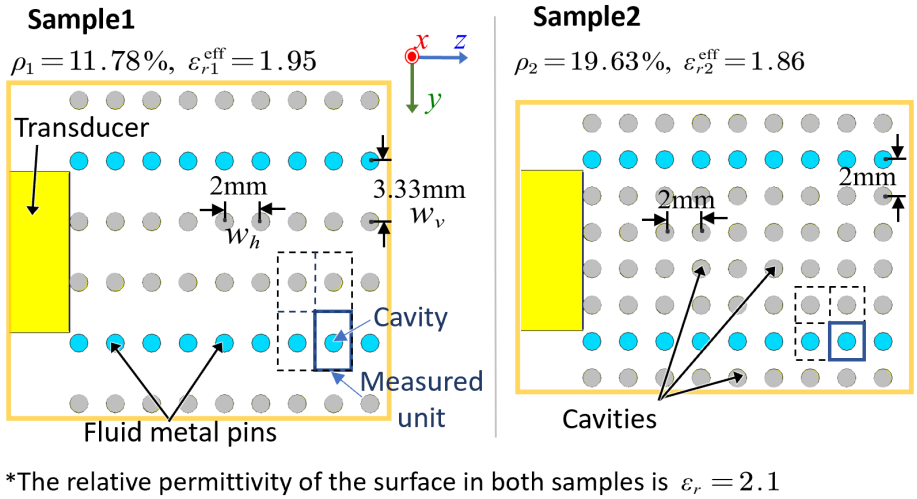

Figure 3.6: Two samples of porous surfaces, each having different densities of cavity distribution, i.e., porosity.

of surface waves. Experimental details, as described in Chapter 4, involve the use of 3D-printed surfaces for a quick and straightforward evaluation of surface wave propagation characteristics.

3.2.5 The Porosity of the Dielectric Layer

Furthermore, porosity serves as a fundamental parameter in the design of this reconfigurable surface wave platform. The variation in porosity, also referred to as cavity distribution density, can potentially impact the propagation of surface wave. Fig. 3.5 illustrates the transformation from a flat surface to a porous surface by introducing evenly distributed cavities and Fig. 3.6 presents two surface samples with different porosity form the top view. Here the values of porosity ρ is defined as $\rho = S_{\text{cavity}}/S_{\text{measured-unit}}$ where S_{cavity} denotes the top area of each cavity and

$S_{\text{measured-unit}}$ is the top area of the measured unit (i.e., the rectangular area marked in the figure). In the proposed porous surface with uniform cavity distribution, the porosity will change the relative permittivity of the dielectric layer ε_r and it can be estimated to be an effective value $\varepsilon_r^{\text{eff}}$ as [107]

$$\varepsilon_r^{\text{eff}} = \frac{\varepsilon_r \left[1 + 3\varepsilon_r + 3\rho(1-\varepsilon_r)\right]}{1 + 3\varepsilon_r + \rho(\varepsilon_r - 1)}, \tag{3.2}$$

It can be seen that in sample 1 and 2, the porosities are $\rho_1 = 11.78\%$ and $\rho_2 = 19.63\%$, respectively. And their corresponding permittivities are $\varepsilon_{r1}^{\text{eff}} = 1.95$ and $\varepsilon_{r2}^{\text{eff}} = 1.86$, respectively. Additionally, when calculating the surface reactance in (2.6) of Section 2.3.2, it is necessary to consider $\varepsilon_r^{\text{eff}}$ effected by the porosity to replace ε_r as

$$X_s = \omega\mu_0 \left(\frac{\varepsilon_r^{\text{eff}} - 1}{\varepsilon_r^{\text{eff}}} h_d + \frac{\Delta}{2} \right). \tag{3.3}$$

Based on (3.2) and (3.3), the effects of different porosity on the surface wave signal will be further discussed in Section 4.3.1.4.

3.2.6 Simulation Results

To visually demonstrate the ability of the proposed reconfigurable surface to guide surface waves along dedicated pathways using two rows of fluid metal walls, Fig.3.7(b) presents the simulation result of a 3D electromagnetic simulation of this surface in guided wave model in computer simulation technology (CST) software. It can be seen that surface waves are excited by Transducer 1, which takes the form of a standard rectangular waveguide (WR). And then surface waves propagate along the surface-air interface in an open environment until reaching Transducer 2 at the right end, with the propagation direction denoted as the $+z$-direction. And it is evident that most of the surface waves are concentrated inside the created pathway consistently.

In contrast, Fig.3.7(a) depicts the non-guided model where the surface wave spreads across the entire surface where the cavities remain empty. To quantify the improvement, the E-field power density is normalized at a reference point located

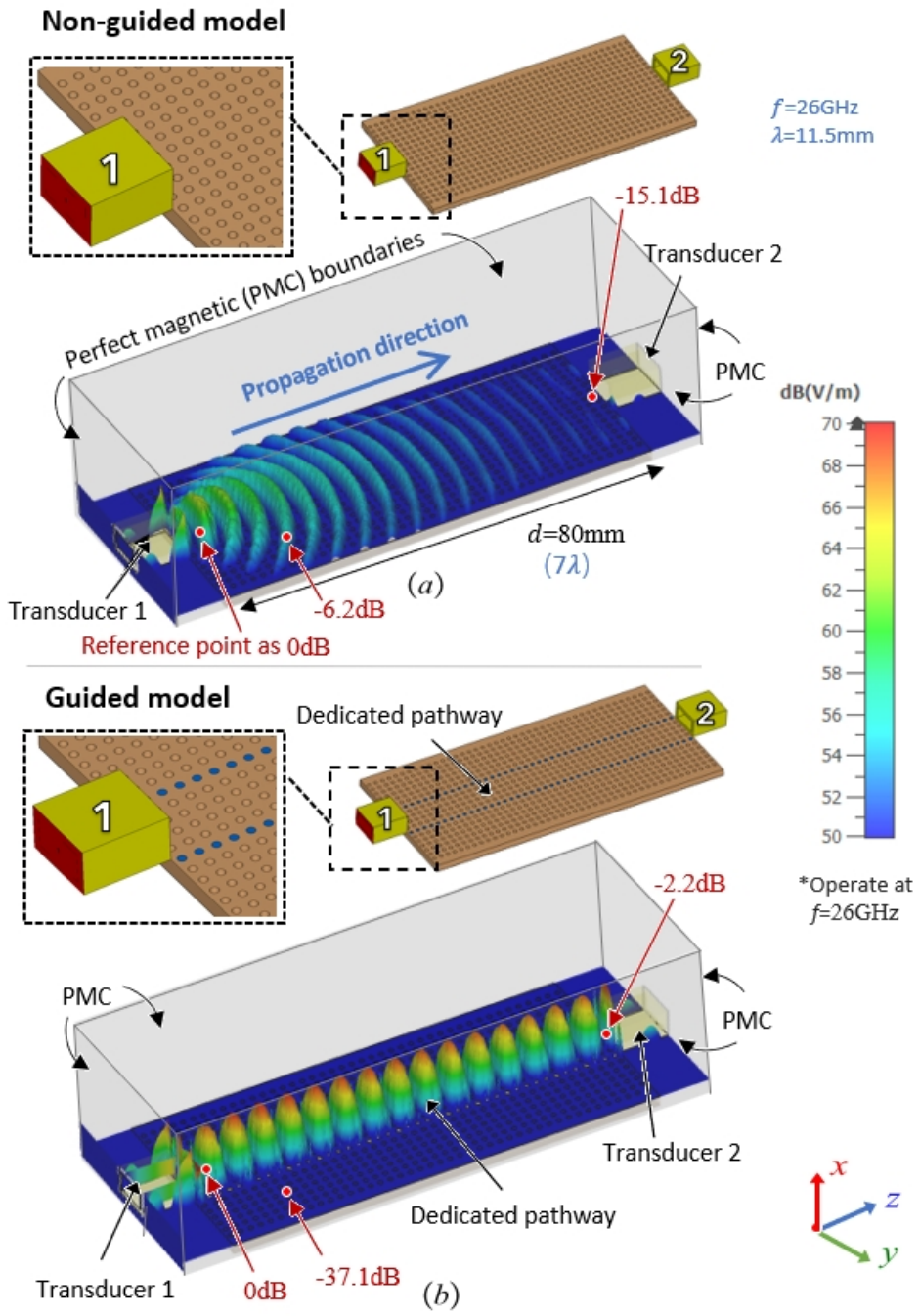

Figure 3.7: The E-field contour of (a) a non-guided surface model, illustrating that the surface wave spread over the entire surface, and (b) a guided model where the surface wave is guided along a straight dedicated pathway by two columns of fluid metal walls in the reconfigurable surface geometry in Fig. 3.1 in CST at 26 GHz.

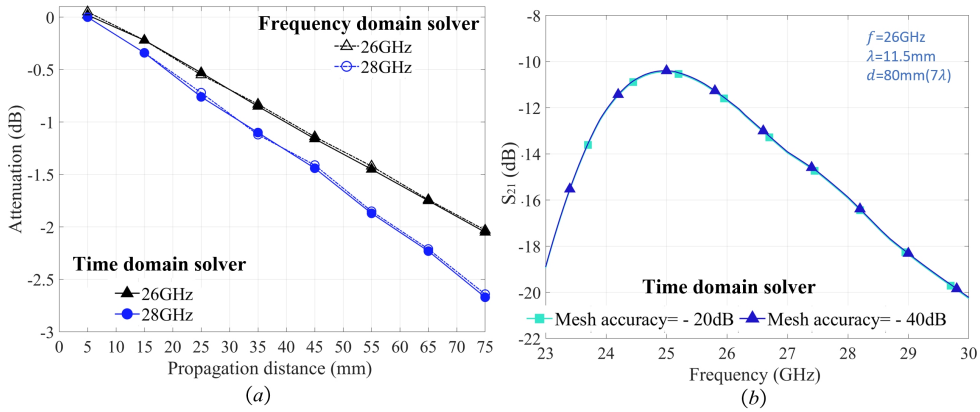

Figure 3.8: (a) The simulation results of time- and frequency-domain solver in CST at 26 GHz and 28 GHz. (b) The results of mesh accuracy from −20 dB to −40 dB in a broadband.

5 mm (0.4λ) in front of the aperture of Transducer 1, set as value of 0 dB. The results demonstrate that the surface wave decays to −2.2 dB at the aperture of Transducer 2 along the straight pathway, with a propagation distance of 80 mm (7λ), while it diminishes to −15.1 dB in the non-guided case. The concentration of the E-field within the fluid metal-filled cavities along the straight pathway is clearly observed. Moreover, the power outside the pathway is kept to be a low value of −37.1 dB, in contrast to the higher value of −6.2 dB observed at the same position in the non-guided scenario. This observation strongly suggests that the proposed reconfigurable surface is capable of creating an isolated propagation pathway to guide surface waves and facilitate efficient SWC.

In CST, it is common to utilize both time-domain and frequency-domain solvers to address the Maxwell equation system. The time-domain solver is primarily based on a hexahedral grid, simulating the behavior of devices across the entire broadband frequency range. Meanwhile, the frequency-domain solver allows the option of either Hexahedral or adaptive grids, specifically useful for the design and analysis of narrowband antenna problems. Opting for a finer grid can enhance model accuracy but comes with an increased computational time cost. Therefore, when determining the level of grid refinement, striking a balance between computational precision and efficiency is essential. In CST, the default recommendation often leans towards Hexahedral, setting for providing better numerical stability and

efficiency, especially when dealing with regular geometric structures. Additionally, CST provides the option to adjust grid precision using the Accuracy setting.

Fig.3.8 (a) provides simulation results for the guided pathway model in Fig.3.7 (b) by using CST in both time-domain and frequency-domain solvers, with the frequency set at a narrow band at $f = 26\,\text{GHz}$ or $28\,\text{GHz}$, a sampling period of $10\,\text{mm}$, and a mesh accuracy of $-20\,\text{dB}$ (CST default recommendation). It is evident that the results obtained from both solvers are essentially consistent. Additionally, Fig.3.8 (b) illustrates wideband simulation results for the time-domain solver applied to the model in Fig.3.7 (b), with the frequency range set at $f = 23\,\text{GHz} - 30\,\text{GHz}$ and mesh accuracy set at both $-20\,\text{dB}$ and $-40\,\text{dB}$ (simulation time longer, approximately 1.5 times that of $-20\,\text{dB}$). A comparative analysis reveals that the results at $-20\,\text{dB}$ and $-40\,\text{dB}$ are nearly identical, indicating that $-20\,\text{dB}$ is sufficient to achieve reasonably accurate simulation results. Subsequent analyses in this thesis will consider the performance of surface structures across a wide frequency range, and therefore, all simulation results are primarily based on the time-domain solver with Hexahedral mesh accuracy=$-20\,\text{dB}$.

3.3 Mathematical Analysis Model

3.3.1 The Geometry of Straight Guided Pathway

To evaluate the path loss of surface waves along the dedicated pathway in this surface wave platform, a corresponding mathematical analysis model is proposed to derive the theoretical power distribution at specific measurement points within the surface wave propagation pathway. For facilitating the analysis, the pathway is conceptually simplified by substituting two complete metal walls for the columns of cylindrical metal pins, as depicted in Fig. 3.9. This idealized model aims to effectively focus the surface wave propagation along a specific pathway and restricts its spreading beyond the boundaries of the pathway. The investigation is primarily concerned with the interface between the air and dielectric layer, precisely the $y-z$ plane where $x = 0$. The bottom center point of Transducer 1, serving as the source of surface waves, is set as the origin $(0,0,0)$ of the xyz coordinate system. And within

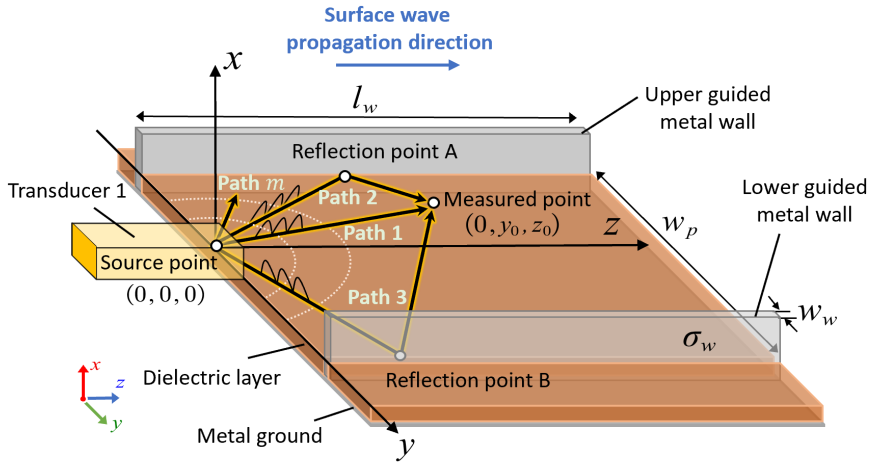

Figure 3.9: The geometry of the straight guided pathway created by two complete metal walls embedded into the surface for analyzing the surface wave rays in different propagation paths from the source point $(0,0,0)$ to the measured point $(0, y_0, z_0)$.

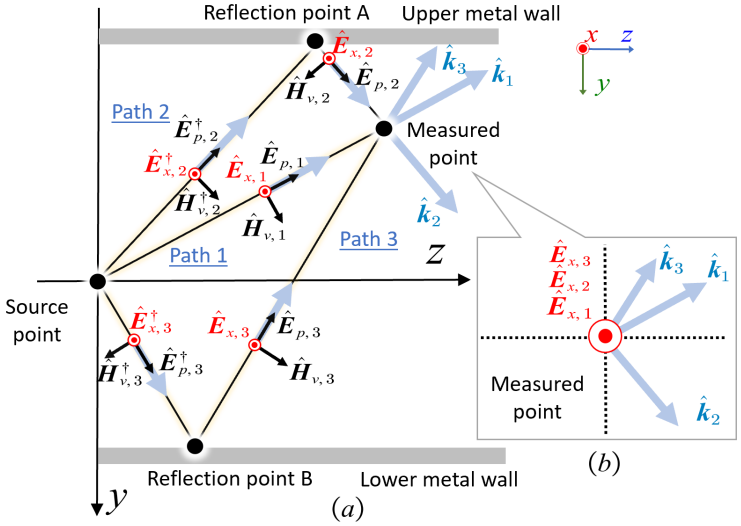

Figure 3.10: (a) The distribution of the field strengths of surface wave rays in paths $1-3$ within the two layers of metal walls and (b) their $\hat{\boldsymbol{E}}_{\boldsymbol{x}}$ at the measured point.

the pathway, a targeted measured point is set as $(0, y_0, z_0)$. Two parallel columns of metal walls are embedded in the dielectric-metal surface, extending along the $+z$-direction and aligning parallel to the transducer. They can be modeled as metal plates with a electrical conductivity of σ_w, possessing a length of l_w and a width of w_w. The bottom of the metal walls maintains contact with the metal ground. And the vertical separation between these two metal walls, denoted as w_p, characterizes the width of the guided pathway. To ensure the accuracy of subsequent simulation findings, the height of the metal walls can be slightly increased beyond the height of the dielectric layer. This adjustment can mitigate the introduction of extraneous boundary conditions that may impact the electromagnetic field strength at the interface of the air-dielectric layer. Additionally, the left initial ends of the metal walls are aligned with the $y = 0$ axis, thus eliminating any gaps between the metal walls and the emission aperture of the transducer along the $+z$-direction, consequently precluding additional leakage of surface waves from gaps.

Theoretically, at the $y - z$ plane with $x = 0$, surface wave rays are excited by transducer 1 from the source point $(0, 0, 0)$ within a semicircular region centered around the transducer. The propagation trajectory is denoted as the path m ($m \in \mathbb{N}^+$) [1] where the surface wave ray travels from the source point to the measured point. The communication modeling method employed here is known as ray tracing, which analyzes and optimizes the performance of communication systems by simulating the propagation of light rays in the environment [108]. Typically, ray tracing is utilized to predict the signal propagation paths, multipath effects, reflections, refractions, and attenuations under various environmental conditions. It can also find applications in indoor positioning [109, 110]. In this model, m is an integer tending towards positive infinity, indicating an infinite number of paths in the ray tracing model. As shown in Fig. 3.9, it can be observed that the formation of a unique direct surface wave path, path 1, extending from the source to the measured point as a direct line-of-sight communication path. In addition to path 1, all

[1] For the sake of clarity, 'path' refers to the trajectory of the surface wave ray excited by the transducer from the source point to the measured point, while the term 'pathway' refers to the specific channel created by the guided metal walls for surface wave propagation in this thesis.

other surface wave rays in paths will undergo reflection between the two layers of metal walls before reaching the measured point. For instance, considering single reflection, surface waves in path 2 and path 3 from the source point will reflect at the inner sides of the upper and lower metal walls, respectively, at reflection points A and B, and then reach the measured point.

And Fig. 3.10 depicts the surface wave rays of paths $1-3$ within the two layers of metal walls, illustrating the distribution of the field strengths. As discussed in Section 2.3.1, surface waves propagate in the TM mode, possessing E-field components both in the vertical and parallel directions to the wave propagation. Given that the wave propagation direction in each path is not solely in the $+z$-direction anymore, the equation in (2.1) for field strengths should be adjusted accordingly. Here, the E-field component $\hat{\boldsymbol{E}}_{\boldsymbol{p}}$ is defined as the component along the direction of wave propagation, while $\hat{\boldsymbol{H}}_{\boldsymbol{v}}$ represents the H-field component. And it is crucial to note that the direction of $\hat{\boldsymbol{E}}_{\boldsymbol{x}}$ remains unchanged, still aligned with the $+x$-direction. Thus, for any surface wave in path m, their field strengths should be written as

$$\begin{cases} \hat{\boldsymbol{H}}_{\boldsymbol{v}} = \hat{\boldsymbol{v}} \dfrac{1}{\sqrt{d_m}} A e^{-\gamma_p d_m} e^{-\gamma_x x} e^{j\omega t} Q_m \\ \hat{\boldsymbol{E}}_{\boldsymbol{x}} = \hat{\boldsymbol{x}} \dfrac{\gamma_p}{\sqrt{d_m} j\omega\varepsilon_0} A e^{-\gamma_p d_m} e^{-\gamma_x x} e^{j\omega t} Q_m \\ \hat{\boldsymbol{E}}_{\boldsymbol{p}} = -\hat{\boldsymbol{p}} \dfrac{\gamma_x}{\sqrt{d_m} j\omega\varepsilon_0} A e^{-\gamma_p d_m} e^{-\gamma_x x} e^{j\omega t} Q_m \,. \end{cases} \tag{3.4}$$

where d_m represents the surface wave ray propagation distance in each path m. A is an initial amplitude constant, which can be set as 1 for convenience in calculations. $\hat{\boldsymbol{v}}$, $\hat{\boldsymbol{x}}$, and $\hat{\boldsymbol{p}}$ denote the corresponding unit vectors for the field strengths. The parameter γ_p represents the propagation coefficient along the direction of wave propagation, which is equivalent to γ_z in (2.1). On the other hand, γ_x remains the same as the one in (2.3) in the $+x$-direction. $e^{j\omega t}$ is the complex exponential function and can be omitted in subsequent derivations. It should be noted that Q_m is defined as a set factor that accounts for the influence of multiple reflections along path m from the source to the measured point on the values of field strengths. It is evident that, for each path m, the phase and magnitude of the field strengths are

influenced by only two variables, namely d_m and Q_m. Further discussion will be conducted to determine the specific values of these variables.

From Fig. 3.10(a), it can be observed that in the direct path 1 and the reflected paths 2 and 3, surface wave rays with different phases and magnitudes converge at the measured point and undergo superposition of field strengths. Here, $\hat{\boldsymbol{k}}_1$, $\hat{\boldsymbol{k}}_2$ and $\hat{\boldsymbol{k}}_3$ represent the direction of the wave vector. In general, the magnitude of $\hat{\boldsymbol{E}}_{\boldsymbol{x}}$ is much larger than that of $\hat{\boldsymbol{E}}_{\boldsymbol{p}}$, which is determined by the values of γ_p and γ_x. Therefore, in this ray tracing model and subsequent simulations, the power of $\hat{\boldsymbol{E}}_{\boldsymbol{x}}$ in dB can be approximately considered as the power of the surface wave. Furthermore, as shown in Fig. 3.10(b), since the field strength of $\hat{\boldsymbol{E}}_{\boldsymbol{x}}$ always aligns along the x-axis rather than varying in the $y-z$ plane like $\hat{\boldsymbol{E}}_{\boldsymbol{p}}$ and $\hat{\boldsymbol{H}}_{\boldsymbol{v}}$ with respect to path m, the analysis focusing on the superposition of $\hat{\boldsymbol{E}}_{\boldsymbol{x}}$ can ignore the wave decomposition in the $y-z$ plane, significantly simplifying the mathematical analysis. And then the vector notation can be omitted, and subsequent analysis will focus on x-axis only and consider E_x as a scalar directly.

3.3.2 Signal Superposition Within the Pathway

$n(n \in \mathbb{N})$ is defined as the number of reflections experienced by a surface wave ray propagating along a specific path between the upper and lower guiding metal walls, from the source point to the measured point. Fig. 3.11 illustrates several examples of paths ranging from $n = 0$ to infinity in the $y-z$ plane. Let w_1 and w_2 represent the distances from the source point $(0,0)$ to the lower and upper metal walls, respectively, where $w_1 + w_2 = w_p$. As mentioned before, it can be observed that when $n = 0$, there is only one path, i.e., path 1, from $(0,0)$ to (y_0, z_0) with a propagation distance of $d_1 = \sqrt{y_0^2 + z_0^2}$ as shown in Fig. 3.11(a). As n increases when $n \geq 1$, there are precisely two distinct surface wave propagation paths, labeled as $2n$ and $2n+1$, emerge as depicted in Fig. 3.11$(b)-(f)$. For example, when $n = 1$, only paths 2 and 3 are present, and for $n = 2$, paths 4 and 5 are the only ones that exist. This pattern persists for higher values of n due to the fixed incident angles θ_{2n} and θ_{2n+1} for any path $2n$ and path $2n+1$ from $(0,0)$ to (y_0, z_0), corresponding to a given value of n. Additionally, apart from the incident angles, each path has specific propagation

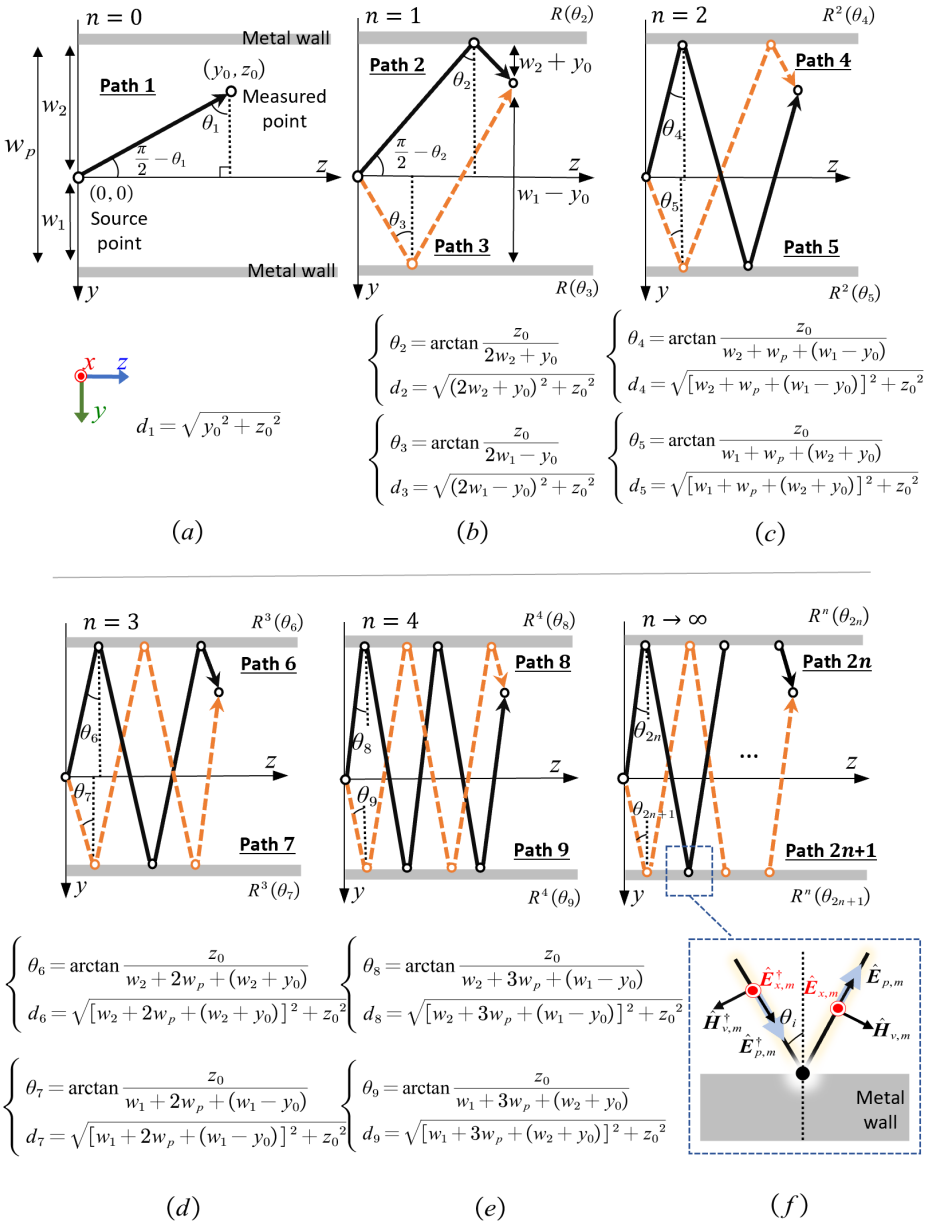

Figure 3.11: The illustration of the surface wave rays in propagation paths within the metal wall after (a) 0, (b) 1, (c) 2, (d) 3, (e) 4 and (f) n times reflection and its E-field and H-field components distribution at a reflection point.

distances that can be determined using trigonometric functions as shown in each figure. Therefore, it can be concluded that for any positive integer value of n, the equations of incident angles and propagation distances for the corresponding paths $2n$ and $2n+1$ can be derived as follows

$$\begin{cases} \theta_{2n} = \arctan \dfrac{z_0}{w_2 + (n-1)\, w_p + (n \bmod 2)\, (w_2 + y_0)} \\ \qquad\qquad \dfrac{1}{+ (n - 1 mod\ 2)\, (w_1 - y_0)} \\ d_{2n} = \sqrt{\left[w_2 + (n-1)\, w_p + (n \bmod 2)\, (w_2 + y_0) \right.} \\ \qquad \sqrt{\left. + (n - 1 mod\ 2)\, (w_1 - y_0) \right]^2 + z_0^2}, \quad n \geq 1, \end{cases} \tag{3.5}$$

and

$$\begin{cases} \theta_{2n+1} = \arctan \dfrac{z_0}{w_1 + (n-1)\, w_p + (n - 1 mod\ 2)\, (w_2 + y_0)} \\ \qquad\qquad \dfrac{1}{+ (n \bmod 2)\, (w_1 - y_0)} \\ d_{2n+1} = \sqrt{\left[w_1 + (n-1)\, w_p + (n - 1 mod\ 2)\, (w_2 + y_0) \right.} \\ \qquad \sqrt{\left. + (n \bmod 2)\, (w_1 - y_0) \right]^2 + z_0^2}, \quad n \geq 1, \end{cases} \tag{3.6}$$

where the symbol mod represents the modulo operation. The incident angles θ_{2n} and θ_{2n+1} are constrained to the range $(0, \frac{\pi}{2})$. It should be noted that as n approaches infinity, these angles tend towards infinitesimally small values, while the propagation distances d_{2n} and d_{2n+1} tend towards infinity. Fig. 3.11(f) illustrates the distribution of incident and reflected E- and H-field field components of the surface wave ray on the metal wall during single reflection. By applying the boundary conditions, the equation for the reflection coefficient R of the TM mode surface wave can be derived as

$$R\left(\theta_i, \sigma_w\right) = \frac{\cos\theta_i - \sqrt{\varepsilon_w/\varepsilon_0 - \sin^2\theta_i}}{\cos\theta_i + \sqrt{\varepsilon_w/\varepsilon_0 - \sin^2\theta_i}}, \varepsilon_w = -j\frac{\sigma_w}{\omega}, \tag{3.7}$$

where θ_i represents the common incident angle, and ε_w denotes the permittivity of the metal walls, which is defined by its electrical conductivity σ_w. It can be observed that the reflection coefficient R is primarily dependent on the incident

angle and the electrical conductivity of metal walls.

Previously, it is mentioned that the surface wave rays are excited from the source point of the transducer within a semicircular region. Theoretically, the field strength of the surface wave ray is variable along different propagation directions from the transducer, i.e., $\frac{\pi}{2} - \theta_i$. The magnitude variation coefficient C can be found in [25] as

$$C(\theta_i) = \cos \frac{9 w_a (\pi - 2\theta_i)}{14\lambda}, \tag{3.8}$$

where λ is the wavelength of working frequency and w_a denotes the aperture width of a rectangular transducer.

Then, the equation for E_x in (3.4) at the measured point (y_0, z_0) can be reformulated within this ray tracing model considering multiple surface wave rays. For $n = 0$, $E_{x,1}$ exists in path 1. For $n \geq 1$, $E_{x,2n}$ and $E_{x,2n+1}$ exist in path $2n$ and path $2n+1$, respectively. Furthermore, the set factor $Q_m = R^n C$ is also taken into account. Therefore, the following equations are obtained as

$$\begin{cases} E_{x,1} = A \dfrac{\gamma_p}{j\omega\varepsilon_0} \dfrac{1}{\sqrt{d_1}} C(\theta_1)\, e^{-\gamma_p d_1} e^{-\gamma_x x}, \quad n = 0 \\ E_{x,2n} = A \dfrac{\gamma_p}{j\omega\varepsilon_0} \dfrac{1}{\sqrt{d_{2n}}} C(\theta_{2n})\, R^n(\theta_{2n}, \sigma_w)\, e^{-\gamma_p d_{2n}} e^{-\gamma_x x}, \quad n \geq 1 \\ E_{x,2n+1} = A \dfrac{\gamma_p}{j\omega\varepsilon_0} \dfrac{1}{\sqrt{d_{2n+1}}} C(\theta_{2n+1})\, R^n(\theta_{2n+1}, \sigma_w)\, e^{-\gamma_p d_{2n+1}} e^{-\gamma_x x}, \quad n \geq 1, \end{cases} \tag{3.9}$$

where R^n represents the factorial of R raised to the power of n, indicating the cumulative impact of n successive reflections on the surface wave ray within the bilateral metal walls.

Furthermore, the E-field strength $E_{x,c}$ at the measured point is a superposition of the $E_{x,m}$ for all rays that arrive at the measured point along different paths m in this surface wave model as follows

$$E_{x,c} = E_{x,1} + \sum_{n=1}^{\infty} \left(E_{x,2n} + E_{x,2n+1} \right), \tag{3.10}$$

The number of reflections n will approach positive infinity ∞ numerically, resulting in infinitely small incident angles θ_{2n} and θ_{2n+1}, as well as infinitely large propagation distance d_{2n} and d_{2n+1}, as shown in (3.5) and (3.6). Additionally, these infinitely large propagation distances give rise to an infinite decay in path loss, causing the E-field values to diminish significantly and become negligible. As a consequence, as n tends to positive infinity, the cumulative E-field strength $E_{x,c}$, which represents the summation of individual E-fields, will converge to a specific value.

To derive the general relationship between the propagation distance d and the cumulative E-field strength $E_{x,c}$ for the surface wave as a whole, the scenario is considered where the source and measured points are both positioned along the central line of the metal walls in the y-axis. The values are then changed to $w_1 = w_2 = \frac{w_p}{2}$, $y_0 = 0$, and $z_0 = d_1 = d$. By substituting these values into (3.5) and (3.6), the desired relationship can be obtained as

$$\begin{cases} \theta_{2n} = \theta_{2n+1} = \arctan \dfrac{d}{\sqrt{n^2 w_p^2 + d^2}} \\ d_{2n} = d_{2n+1} = \sqrt{n^2 w_p^2 + d^2}, \end{cases} \tag{3.11}$$

Furthermore, (3.9) can be rewritten as

$$\begin{cases} E_{x,1} = A \dfrac{\gamma_p}{j\omega\varepsilon_0} \dfrac{1}{\sqrt{d}} e^{-\gamma_p d} e^{-\gamma_x x}, \quad n = 0 \\ E_{x,2n} = E_{x,2n+1} = A \dfrac{\gamma_p}{j\omega\varepsilon_0} \dfrac{1}{\sqrt[4]{n^2 w_p^2 + d^2}} C\left(\arctan \dfrac{d}{\sqrt{n^2 w_p^2 + d^2}}\right) \\ \quad \times R^n\left(\arctan \dfrac{d}{\sqrt{n^2 w_p^2 + d^2}}, \sigma_w\right) e^{-\gamma_p \sqrt{n^2 w_p^2 + d^2}} e^{-\gamma_x x}, \quad n \geq 1, \end{cases} \tag{3.12}$$

Finally, substituting (3.12) into (3.10), the desired general cumulative E-field strength $E_{x,c}$ can be obtained as

$$
\begin{aligned}
E_{x,c} &= E_{x,1} + 2\sum_{n=1}^{\infty} E_{x,2n} \\
&= A\frac{2\gamma_p}{j\omega\varepsilon_0}\left[\frac{1}{2\sqrt{d}}e^{-\gamma_p d} + \sum_{n=1}^{\infty} \frac{1}{\sqrt[4]{n^2w_p^2+d^2}} \times C\left(\arctan\frac{d}{\sqrt{n^2w_p^2+d^2}}\right)e^{-\gamma_p\sqrt{n^2w_p^2+d^2}}\right. \\
&\left.\times R^n\left(\arctan\frac{d}{\sqrt{n^2w_p^2+d^2}}, \sigma_w\right)\right] e^{-\gamma_x x}.
\end{aligned}
\tag{3.13}
$$

It can be observed that the cumulative E-field strength $E_{x,c}$, i.e., total E-field, at a specific measured point within the pathway exhibits a significant correlation with the propagation distance. Furthermore, the characteristics of the propagation surface and the metallic material and width of the pathway exert notable influences on the E-field. These factors will be further elucidated in the subsequent results of Section 3.4.

3.3.3 Signal Superposition Beyond the Pathway

On the other hand, in this guided pathway analysis model, the signal of surface waves outside the metal wall can also be calculated. Fig. 3.12(a) illustrates the placement of the measured point (y_0, z_0) outside the wall, where it is observed that the surface wave ray in path 1 directly traverses the lower metal wall from the source point to reach the measured point. And in Fig. 3.12(b), the ray in path 2 undergoes single reflection at the wall and continues its propagation through the transmission to reach the measured point. n ($n \in \mathbb{N}$) is also defined as the number of reflections, and Fig. 3.12$(c)-(f)$ provide the equations for the incident angles and propagation distances for different surface wave paths.

It is significant to emphasize that outside the metal wall, each value of n only corresponds to single propagation path rather than two, determined by trigonometric functions, in contrast to the scenario within the confines of the metal wall discussed in the previous section. Furthermore, Fig. 3.12(f) presents the distribution of the

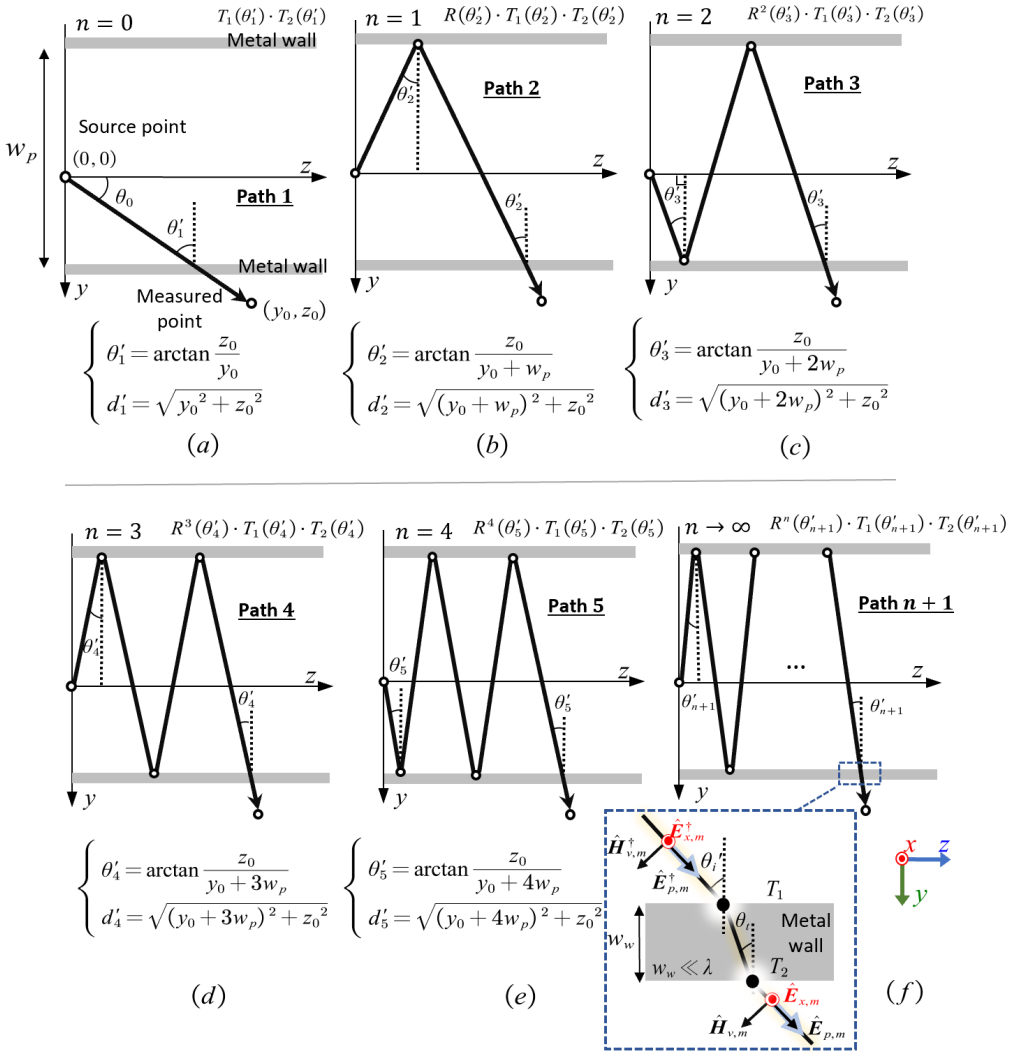

Figure 3.12: The illustration of the transmitting surface wave rays in propagation paths outside the metal wall after (a) 0, (b) 1, (c) 2, (d) 3, (e) 4 and (f) n times reflection and its E-field and H-field components distribution at a transmission point.

E-field and H-field components at the transmission point on the wall. It can be observed that the incident surface wave undergoes two refractions before traversing the metal wall and reaching the measured point. The transmission coefficients for twice refractions can be denoted as T_1 and T_2. Typically, the width of the wall, denoted as w_w, is much smaller than the wavelength, thereby permitting its negligible influence on practical calculations of propagation distance. And the following equation can be get

$$\begin{cases} \theta'_{n+1} = \arctan\dfrac{z_0}{y_0 + nw_p} \\ d'_{n+1} = \sqrt{\left(y_0 + nw_p\right)^2 + z_0^2}, \quad n \geq 0, \end{cases} \tag{3.14}$$

And as shown in Fig. 3.12(f), the transmission angle θ_t can be determined using Snell's law, given by

$$\theta_t = \arcsin\left(\sqrt{\frac{\varepsilon_0}{\varepsilon_w}}\sin\theta'_i\right), \varepsilon_w = -j\frac{\sigma_w}{\omega}, \tag{3.15}$$

Then, based on the electromagnetic boundary conditions, the transmission coefficients T_1 and T_2 for the first and second transmission of this surface wave ray can be obtained as

$$\begin{cases} T_1\left(\theta'_i, \sigma_w\right) = \dfrac{2\cos\theta'_i}{\cos\theta'_i + \sqrt{\frac{\varepsilon_w}{\varepsilon_0} - \sin^2\theta'_i}} \\ T_2\left(\theta'_i, \sigma_w\right) = \dfrac{2\cos\theta_t}{\cos\theta_t + \sqrt{\frac{\varepsilon_0}{\varepsilon_w} - \sin^2\theta_t}}, \end{cases} \tag{3.16}$$

It can be observed that both T_1 and T_2 can be written as equations involving the incident angle θ_i and the electrical conductivity of the metal walls σ_w. Consequently, the equation for $E'_{x,m}$ in Path $n+1$ at the measured point, after n reflections and two transmissions, can be given by

$$E'_{x,n+1} = A\frac{\gamma_p}{j\omega\varepsilon_0}\frac{1}{\sqrt{d'_{n+1}}}C\left(\theta'_{n+1}\right)R^n T_1 T_2\left(\theta'_{n+1}, \sigma_w\right)e^{-\gamma_p d'_{n+1}}e^{-\gamma_x x}, \quad n \geq 1, \tag{3.17}$$

And the cumulative E-field strength $E'_{x,c}$ for all rays that arrive at the measured point along different paths can be written as

$$E'_{x,c} = \sum_{n=0}^{\infty} E'_{x,n+1}\,, \tag{3.18}$$

In Fig. 3.12(a), θ_0 is defined as the tilted angle included between the z-axis and the line connecting the source and target points. Subsequently, the values $z_0 = d\cos\theta_0$ and $y_0 = d\sin\theta_0$ can be substituted into equations (3.16) and (3.17). By simplifying the E-field strength $E'_{x,c}$ in (3.18), the following equation can be obtained as

$$\begin{aligned} E'_{x,c} &= \sum_{n=0}^{\infty} E'_{x,n+1} \\ &= A\frac{\gamma_p}{j\omega\varepsilon_0}\sum_{n=0}^{\infty} \frac{1}{\sqrt[4]{\left(d\sin\theta_0+nw_p\right)^2+d^2\cos^2\theta_0}} \\ &\times C\left(\arctan\frac{d\cos\theta_0}{d\sin\theta_0+nw_p}\right) e^{-\gamma_p\sqrt{\left(d\sin\theta_0+nw_p\right)^2+d^2\cos^2\theta_0}} \\ &\times R^n T_1 T_2\left(\arctan\frac{d\cos\theta_0}{d\sin\theta_0+nw_p}, \sigma_w\right) e^{-\gamma_x x}\,. \end{aligned} \tag{3.19}$$

Similarly, the value of $E'_{x,c}$ at the measured point outside the pathway is also influenced by factors such as propagation distance d. And the comparison of E-fields between the interior and exterior pathways will be discussed in subsequent results.

3.4 Results and Discussion

3.4.1 Inside Pathway in Short-Distance Transmission

The above derived equations regarding E_x are expected to be validated through 3D electromagnetic simulations conducted using CST software in this section. For the simulations, a targeted operating frequency of 26 GHz is set, and WR-34 rectangular waveguides with dimensions of height $h_a = 4.318$ mm and width $w_a = 8.636$ mm are used as transducers. Fig. 3.13(a) illustrates that Transducer 1 is the transmit-

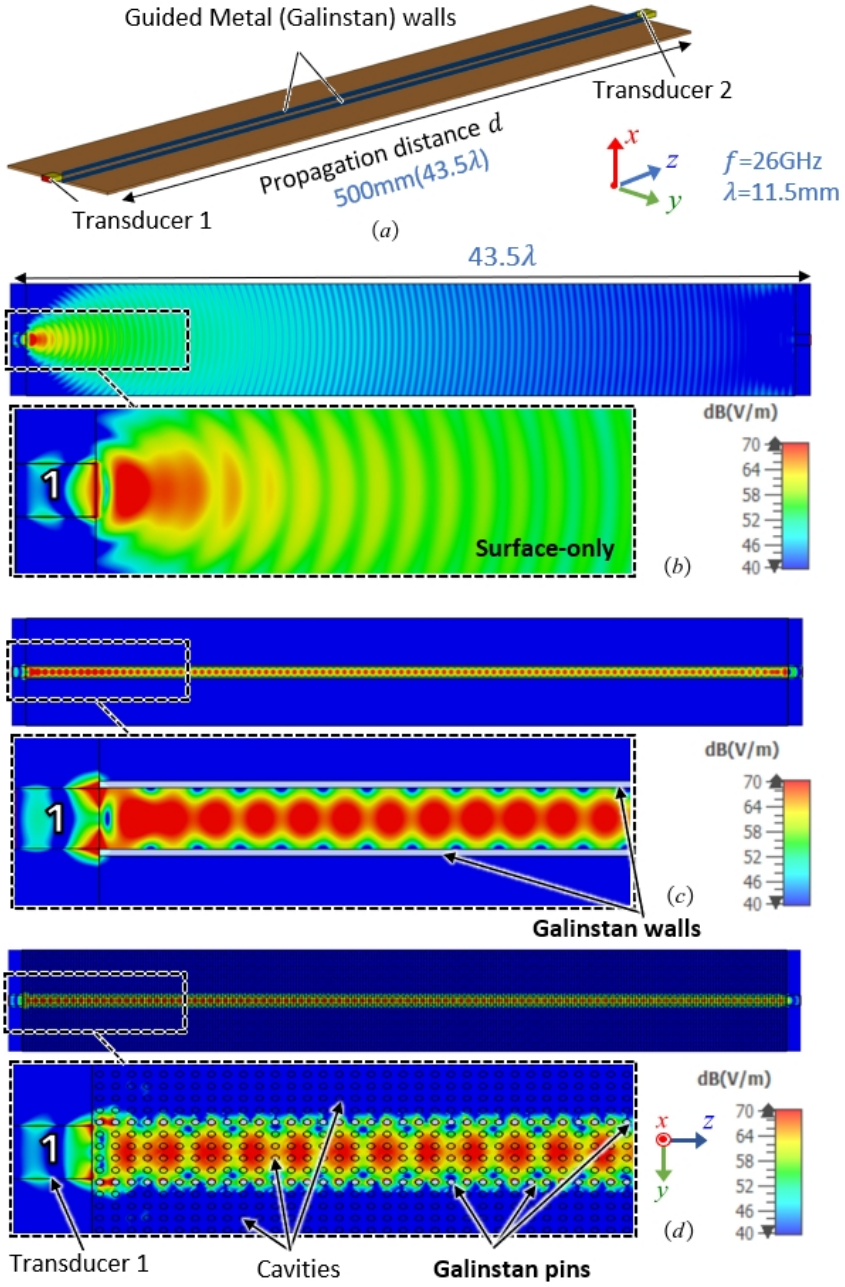

Figure 3.13: (a) A surface geometry featuring the guided metal walls and the simulation results for a range of surface configuration models including the (b)surface-only, (c)Galinstan wall pathway and (d)Galinstan pin pathway.

ter, while Transducer 2 acts as the receiver, both placed at opposite ends of the dielectric-metal surface. A copper plate with a thickness of $h_m = 0.05\,\text{mm}$ serves as the metal ground.

To investigate the impact of different dielectric layers on surface wave propagation, low-loss PTFE ($\varepsilon_{r1} = 1.8$, $\tan\delta = 0.00005$ at 26 GHz) and lossy PTFE ($\varepsilon_{r2} = 2.1$, $\tan\delta = 0.0002$ at 26 GHz) are chosen as the dielectric layers. To ensure consistency, their thicknesses are set to $h_{d1} = 2.95\,\text{mm}$ and $h_{d2} = 2.50\,\text{mm}$ to achieve the same surface impedance Z_s of $j270\,\Omega$, as determined by equation (2.6). This impedance value can theoretically enhance the excitation efficiency of surface waves [25]. And please note currently the surface is not porous. Additionally, two parallel metal walls with a width of $w_w = 1\,\text{mm}$ are integrated into the surface to guide the propagation of surface waves. Different wall materials, including perfect electric conductor (PEC, $\sigma_p = \infty$), copper ($\sigma_c = 59.6 \times 10^6$ S/m), and Galinstan (as fluid metal, $\sigma_g = 3.46 \times 10^6$ S/m), are investigated to examine their influence on surface wave propagation. And initially, the pathway width w_p between the metal walls is set to 9 mm and later adjusted to 11 mm and 13 mm for comparative analysis. The E_x values are measured using multiple sampling probes along the central axis in the $+z$-direction of the propagation pathway. The measured range, referred to as the propagation distance d, spans from 100 mm to 2000 mm (2 m), with the position at 100 mm serving as the normalized reference point. The parameter values used in the simulations are summarized in Table 3.3.

For visual comparison, Fig. 3.13 presents simulation results for a range of surface configurations, demonstrating the propagation characteristics of surface waves in a surface composed of surface-only, Galinstan wall pathway, or Galinstan pin pathway (proposed platform using porous surface). The surface-only model, as depicted in Fig.3.13(b), shows the diffusion of surface waves across the entire surface, accompanied by a gradual attenuation of the field strength magnitude as the propagation distance d increases. Conversely, Fig. 3.13(c) demonstrates that the pathway formed by Galinstan walls effectively concentrates the propagation of surface waves within the pathway while preventing their transmission beyond the Galinstan walls.

Table 3.3: Parameters used in mathematical models and simulations

Parameter	Value
operating frequency, f	26 GHz
transducer (WR-34) frequency band, f_b	22 – 33 GHz
height of transducer aperture, h_a	4.318 mm
width of transducer aperture, w_a	8.636 mm
relative permittivity of the dielectric layer, ε_r	1.8 , 2.1
thickness of the dielectric layer, h_d	2.95 mm, 2.50 mm
surface impedance, Z_s	$j270\,\Omega$
loss tangent, $tan\delta$	0.00005, 0.0002
pathway width, w_p	9, 11, 13 mm
thickness of the metal ground, h_m	0.05 mm
length of the metal wall, l_w	same with d
width of the metal wall, w_w	1 mm
time of reflection, n	10000
tilted angle, θ_0	5°
propagation distance, d	100 – 2000 mm, 0.1 – 50 m
radius of cavities/ metal pins, r	0.5 mm
cavities center-to-center separation, w_c	2 mm
electrical conductivity of PEC, σ_p	∞
electrical conductivity of copper, σ_c	59.6×10^6 S/m
electrical conductivity of Galinstan, σ_g	3.46×10^6 S/m
permittivity of free space, ε_0	8.854×10^{-12} F/m
permeability of free space, μ_0	$4\pi\times10^{-7}$ H/m

Similarly, in Fig. 3.13(d), the pathway composed of Galinstan pins exhibits comparable behavior. These findings highlight the analogous electromagnetic interaction between solid metal walls in this ray tracing model and metal pins in the proposed reconfigurable surface wave platform, in terms of surface wave propagation in the simulation results.

Fig. 3.14(a) illustrates the simulated values of E_x obtained from the sampling probes along the PEC, copper, and Galinstan wall pathways in the low-loss PTFE surface. Additionally, the theoretical values computed using the aforementioned ray tracing model in Matrix Laboratory (MATLAB) are presented for comparison. The results from simulations indicate that at a distance of 2000 mm (corresponding to $173.3\,\lambda$ at the operating frequency of 26 GHz), the surface wave in the Galinstan wall pathway (with electrical conductivity $\sigma_g = 3.46\times10^6$ S/m) experiences only a

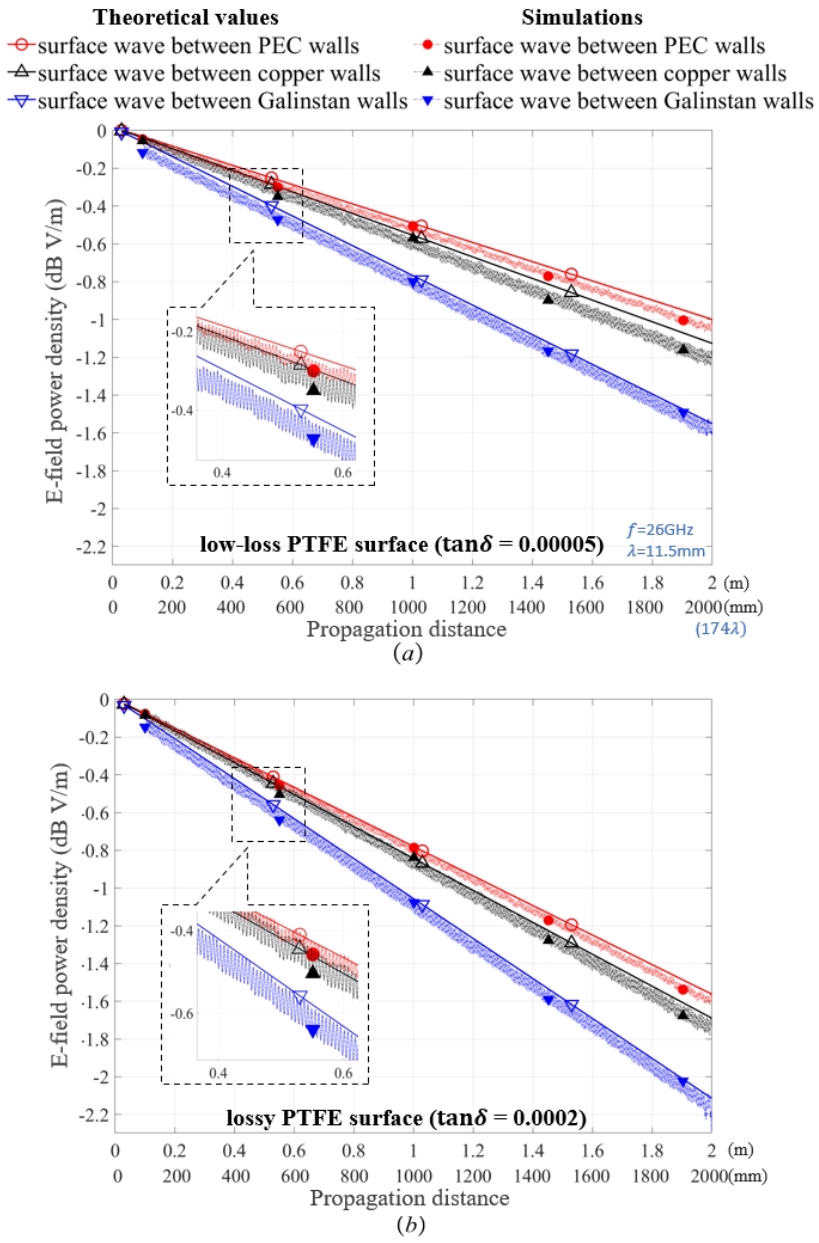

Figure 3.14: Mathematical theoretical values and simulation results for surface waves guided by the PEC, copper, or Galinstan wall pathway in the (a) low-loss PTFE surface or (b) the lossy PTFE surface within a short propagation distance d from 100 mm to 2000 mm.

loss of 1.6 dB, resulting in a path loss of 0.8 dB/m. Moreover, employing PEC walls ($\sigma_p = \infty$) results in a path loss of 0.5 dB/m, while using copper walls ($\sigma_c = 59.6 \times 10^6$ S/m) leads to a path loss of 0.6 dB/m. It is evident that the path loss of the surface wave in the pathway is inversely proportional to the electrical conductivity of metal walls. Nevertheless, the differences in path losses among the different wall materials are negligible. Therefore, the influence of wall material on path loss can be disregarded for short-distance transmissions. In addition, by comparing Fig. 3.14(a) and (b), it is obvious that the utilization of low-loss tangent PTFE ($\tan\delta = 0.00005$) leads to reduced path loss in each metal wall pathway compared with lossy PTFE ($\tan\delta = 0.0002$). This observation suggests that the selection of a low-loss dielectric layer can effectively optimize path loss.

It should be noted that in the calculation of mathematical theoretical values, the number of reflections n is set to 10000 to ensure a sufficiently number of surface wave paths for the convergence of the cumulative E-field strength $E_{x,c}$. It is evident that the theoretical curve exhibits a slight elevation of up to 0.05 dB/m compared to the simulation values. This discrepancy can be attributed to the presence of standing waves in the simulation, which leads to a slightly lower field strength. Additionally, in the simulation environment, the transducers deviate from the ideal point sources described in the surface wave ray tracing model, resulting in minor disparities between the two sets of results. However, these discrepancies are deemed negligible.

Moreover, it is evident that the theoretical curves align closely with the simulation curves, thus validating the effectiveness of the ray tracing model and the reliability of the calculated theoretical values. This confirmation establishes that the model can be utilized to predict surface wave path loss at various scales, particularly over long distances, such as the further discussed 50, m in Section 3.4.3 where current simulation software, such as CST, often encounters challenges in providing precise outcomes in scenarios involving long-distance propagation. In some cases, these software may even fail to produce results in a simulated environment with extensive distances. Additionally, the implementation of mathematical calculation tools like MATLAB enables nearly instantaneous computation time for the ray trac-

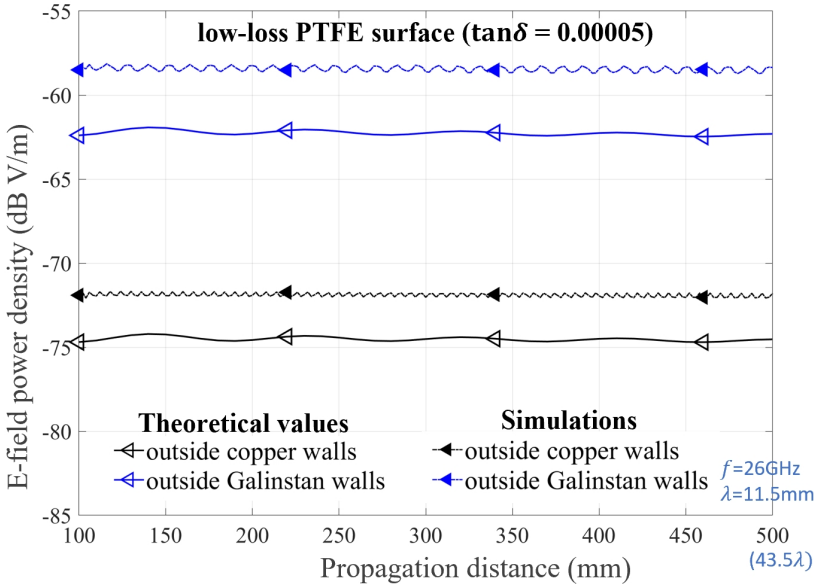

Figure 3.15: Mathematical theoretical values and simulation results for surface waves beyond the copper and Galinstan wall pathways with a titled angle $\theta_0 = 5°$ in 500 mm.

ing model, while performing equivalent simulations in CST to gather similar results would demand a significantly longer duration. This can underscore the advantages associated with the adoption of the ray tracing model.

3.4.2 Outside Pathway in Short-Distance Transmission

Regarding the field value outside the pathway, Fig. 3.15 depicts the theoretical values and simulation results for the measuring line with a clockwise tilted angle of 5° as specified in equation (3.19), where sampling probes are positioned outside the metal walls. The simulations reveal that the recorded E-field values outside the copper wall pathway reach approximately −71 dB, while for the Galinstan walls, the values are around −58 dB. Notably, these field strength values outside the pathway are significantly lower, exhibiting a difference of approximately 50 dB compared to the values within the pathway in last section. This observation highlights the metal wall pathway's capability to effectively concentrate and guide surface wave propagation, resulting in notable gains along the propagation pathway. The significant attenuation of the surface wave signal on the outer surface of the copper wall underscores its strong shielding capability. On the other hand, the Galinstan wall, with

its lower electrical conductivity, demonstrates a relatively higher level of surface wave leakage. This indicates the potential to select wall materials based on specific application requirements, enabling the achievement of either complete blockage or controlled leakage of surface waves. Furthermore, it is worth mentioning that the mathematical theoretical values are slightly lower, approximately 3 dB, compared to the simulation results. This discrepancy can be attributed to the consideration of wave reflections in the simulations, leading to an increase in received power at the receiver. In conclusion, these findings provide evidence for the practical feasibility and utility of metal walls in effectively preventing surface wave propagation in undesired directions. This, in turn, ensures the desired signal integrity while minimizing interference.

3.4.3 Mathematical Prediction in Long-Distance Transmission

As in the above results, the consistency between the prediction of surfae wave ray tracing model and the simulation results for short-distance propagation distances has already demonstrated the effectiveness of the model in predicting surface wave values. On the other hand, Fig. 3.16 illustrates the variations in the E-field within the PEC, copper, and Galinstan wall pathways calculated by the ray tracing model over a range of long-distance transmissions from 0.1 m to 50 m. As depicted in Fig. 3.16(b), when ideal low-loss PTFE ($\tan\delta = 0.0002$) is used as the dielectric layer, the E-field attenuation within the PEC, copper, and Galinstan wall pathways reaches approximately -16 dB, -21 dB, and d attenuation of 80 dB. Additionally, the surface-only model, which considers only surface waves, demonstrates an E-field attenuation of 58 dB. In contrast, the attenuation of space waves is more pronounced, exceeding 90 dB.

Furthermore, Fig. 3.16(a) and (c) compare the theoretical E-field values based on lossless ($\tan\delta = 0$) and lossy PTFE ($\tan\delta = 0.00005$), respectively. It is evident that the metal walls still provide significant gains. However, as the propagation distance increases, the path loss becomes notably higher and can no longer be neglected as in short-distance scenarios. Nevertheless, the path loss within the surface wave pathway remains significantly lower compared to space wave propagation and

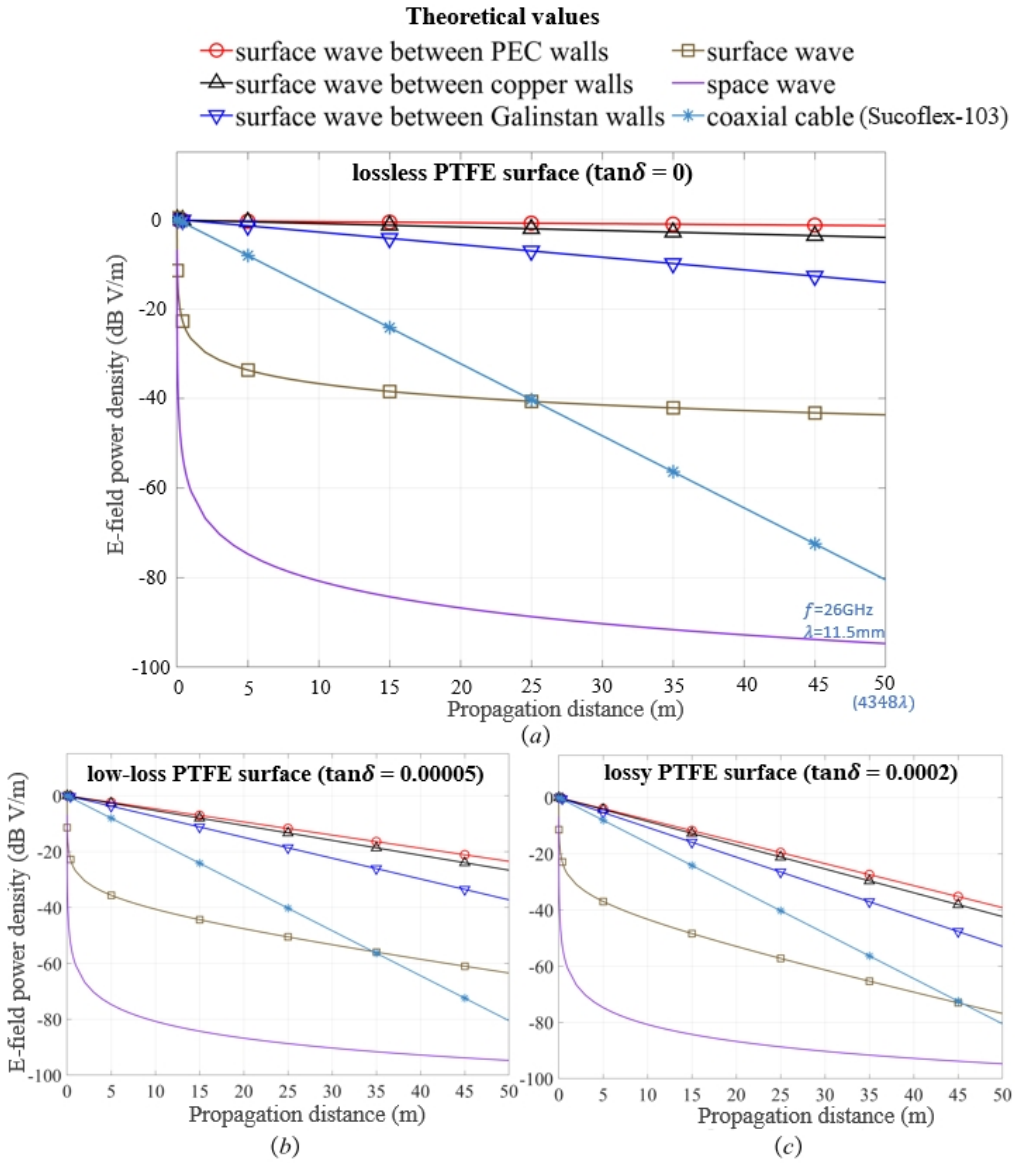

Figure 3.16: Mathematical theoretical values for surface waves within the PEC, copper or Galinstan walls in (a) the lossless PTFE surface with $\tan\delta = 0$, (b) the low-loss PTFE surface with $\tan\delta = 0.00005$ or (c) the lossy PTFE surface with $\tan\delta = 0.0002$ in a long propagation distance, e.g., 50 m. Also, the comparison curves are drew such as space wave, coaxial cable and surface wave in the surface-only model.

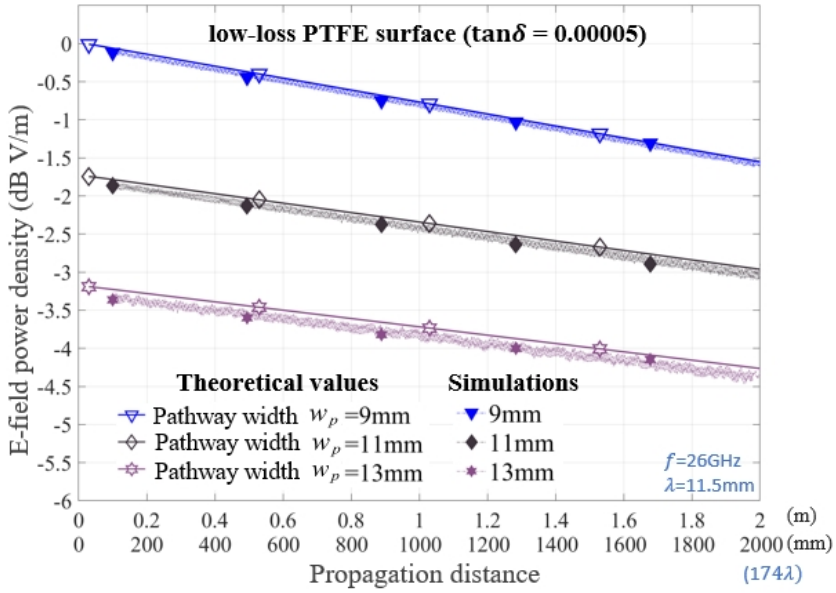

Figure 3.17: The comparison results of surface waves within the Galinstan wall pathway with a pathway width (a) $w_p = 9\,\text{mm}$, (b) $w_p = 11\,\text{mm}$ and (c) $w_p = 13\,\text{mm}$ in the theoretical values and simulations.

coaxial cable transmission. In conclusion, the consistency between the predictions of the surface wave ray tracing model and the simulation results, along with its performance in long-distance transmission scenarios, further validates the metal wall pathway's ability to achieve lower propagation losses compared to other transmission methods.

3.4.4 Effect of Pathway Width

And the pathway width w_p between the metal walls also affects the concentration of surface wave propagation, as depicted in Fig. 3.17. It can be observed that the variation in different pathway width will lead to similar attenuation levels of surface waves within different pathways from 100 mm to 2000 mm, at an approximate magnitude of 1.5 dB. However, distinct initial attenuations are observed across the pathways. For example, with $w_p = 9\,\text{mm}$, the initial attenuation is 0 dB at 100 mm, which acts as the normalized reference point. When $w_p = 11\,\text{mm}$, the initial attenuation increases to 1.7 dB, and while for $w_p = 13\,\text{mm}$, the initial attenuation increases to 3.3 dB. These findings demonstrate that narrower pathways effectively concentrate surface wave propagation, thereby mitigating the initial attenuation at the start-

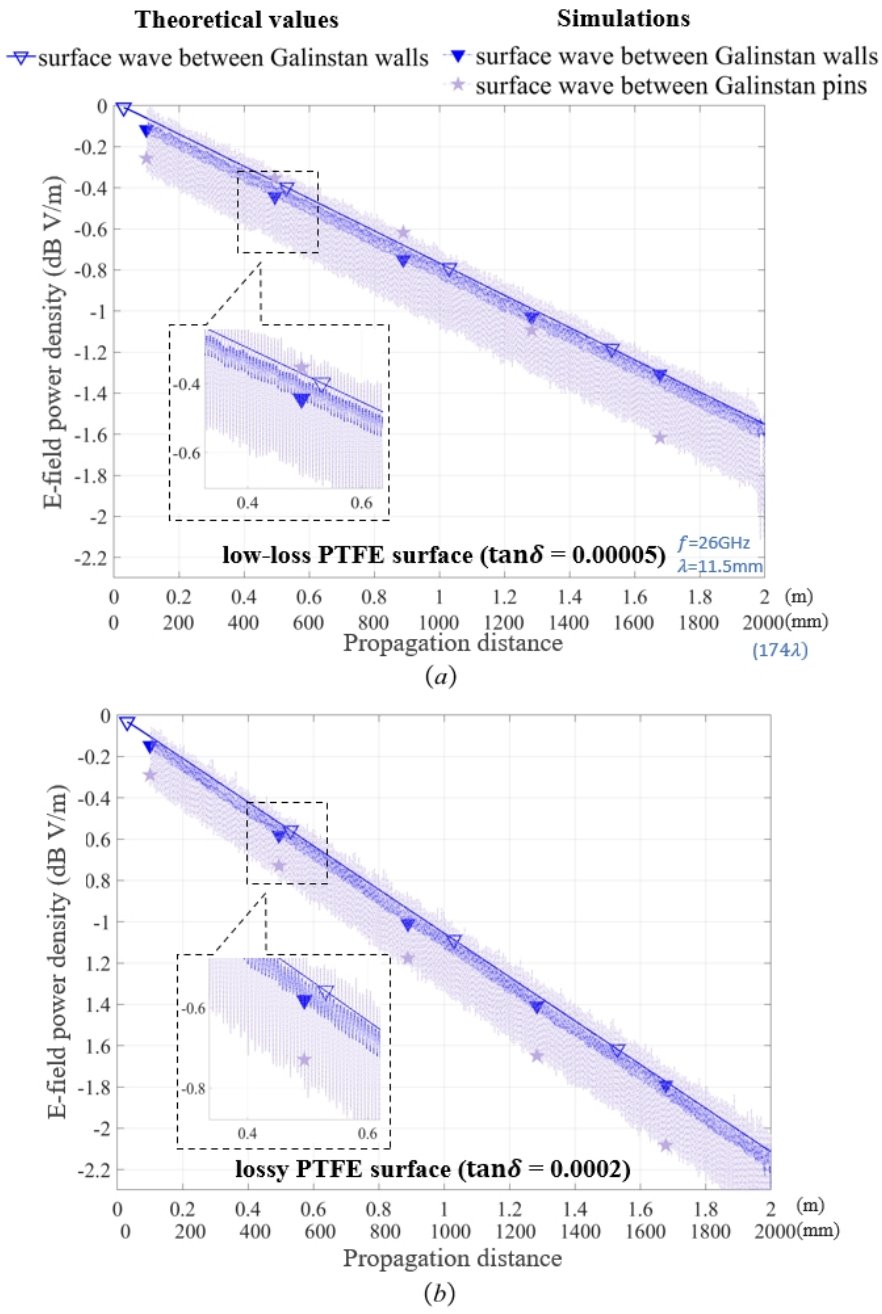

Figure 3.18: The comparison results of surface waves isolated between the Galinstan wall or Galinstan pin pathway in (a) the low-loss PTFE surface or (b) the lossy PTFE surface in the theoretical values and simulations.

ing position. This behavior arises due to the confinement of surface waves within narrower pathways, resulting in a more focused propagation. However, it is to note that excessively reducing the pathway width is not a viable strategy for achieving higher gains in the pathway. Overly narrow pathway widths lead to heightened diffraction losses, exacerbating the attenuation of surface waves. Hence, selecting an appropriate pathway width, preferably one that approximates or slightly exceeds the transducer aperture width denoted as w_a, ensures concentrated surface wave propagation while minimizing excessive attenuation losses.

3.4.5 Metal Wall and Metal Pin Pathways

Finally, as discussed before, the applied ray tracing model for surface wave rays on metal wall surfaces is a fundamental theoretical study aimed at predicting field strength values for surface wave propagation within or beyond predefined pathways. And this model can also be used to simulate scenarios involving the utilization of liquid metal-filled cavities to achieve reconfigurable surface pathways in the proposed surface wave platform. As Fig. 3.18 illustrated, the field decay characteristics are observed in Galinstan wall pathways and Galinstan pin pathways using low-loss PTFE and lossy PTFE surfaces, respectively. In the case of low-loss PTFE, the path loss for Galinstan pin pathways with cavities is approximately 1.70 dB, exhibiting a slight increase of approximately 0.15 dB compared to the path loss for Galinstan wall pathways of approximately 1.55 dB. This difference can be attributed to a minor leakage of surface waves beyond the pathway boundaries due to gaps between the cavities in this reconfigurable surface wave platform. Nevertheless, the observed difference is negligible and can be disregarded. Moreover, the behavior observed in lossy PTFE follows a similar trend to that of low-loss PTFE. The decay curves obtained from all field simulations align well with the mathematical theoretical calculations for metal walls, confirming the effectiveness of the surface wave ray tracing model in accurately capturing path loss within reconfigurable surface pathways. Leveraging this ray tracing model facilitates efficient investigations into the influence of surface characteristics, such as loss tangent, dielectric constant, and thickness, on surface wave propagation. Such analyses enable the determination of

appropriate surface materials and dimensions, which play a critical role in optimizing the design and application of reconfigurable surfaces.

3.5 Conclusions

In conclusion, the proposed reconfigurable surface wave platform offers a promising solution for the manipulation and control of surface wave propagation. By integrating a porous structure, fluid metal, and microfluidic techniques, the platform enables the creation of dynamic pathways, allowing for flexible control of surface waves in various communication environments. The connection with programmable logic devices and pumps further enhances the platform's capabilities by enabling programmable and dynamic pathway configurations.

The effectiveness of the surface wave ray tracing model used in this chapter is validated through the close agreement between the calculated theoretical values and the simulated attenuation curves. The model is utilized to analyze the impact of surface characteristics, such as loss tangent, dielectric constant, and pathway width, on surface wave propagation. This analysis provides valuable insights for selecting suitable surface materials and dimensions. Specifically, dielectric materials with low dielectric loss and high surface impedance are identified as optimal choices for reducing path losses. Additionally, selecting a pathway width that closely matches or slightly exceeds the transducer aperture width ensures focused surface wave propagation while minimizing leakage losses. And the surface wave ray tracing model of surface wave demonstrates accurate predictions of field strength variations in short-distance transmission scenarios, where surface wave attenuation can be seen as negligible. And the findings can also be extrapolated to long-distance transmission scenarios. Furthermore, the platform's metal wall pathway exhibits superior performance in mitigating propagation losses compared to other transmission modes, confirming its favorable characteristics. It should be noted that the ray tracing model is highly parameter-dependent. Before every calculation, careful adjustments of the model are necessary to obtain accurate results. While the ray tracing model can intuitively model multipath and yield relatively positive results,

such as the surface wave straight pathway described in this chapter, it becomes considerably complex and challenging to model in more intricate application scenarios, such as the reconfigurable pathways introduced later in this thesis. This complexity implies that the model may not be suitable for simulating all communication environments.

In conclusion, the innovative design and modeling presented in this chapter hold the promise of opening new avenues for the exploration of the platform's applications in SWC.

Chapter 4

Reconfigurable Pathway on the Reconfigurable Surface Wave Platform

4.1 Introduction

This chapter provides comprehensive results of the experimental measurements conducted on the reconfigurable pathway within the reconfigurable surface wave platform, employing a 3D-printed prototype and a lossy PTFE surface.

In the straight pathway, the primary objective is to analyze the path loss in the physical environment, enabling a better understanding of signal attenuation at various propagation distances and operating frequencies. By doing so, the key factors influencing signal attenuation can be identified. Furthermore, practical aspects such as different pathway widths and the number of metal wall layers are measured and evaluated to determine the optimal structure for the surface wave pathway. Additionally, the impact of surface porosity is explored on surface wave propagation, providing further insights into the relationship between surface wave signal transmission and distinctive surface geometries.

In the turn pathway, a T-shaped reconfigurable surface with an adjustable junction is designed to enable the directional switching of surface wave propagation between a straight pathway and a 90° turn pathway. The attenuation characteristics of surface waves propagating along these two distinct pathways are measured and

compared. Furthermore, various corner configurations are studied within the 90° turn pathway, and the optimal shape with minimal turn insertion losses is identified. This contributes positively to reducing the overall losses incurred by multiple surface wave turns on the surface.

To ensure the reliability of the obtained data from the reconfigurable surface wave platform in the physical environment, all experimental results are compared with their corresponding simulation outcomes.

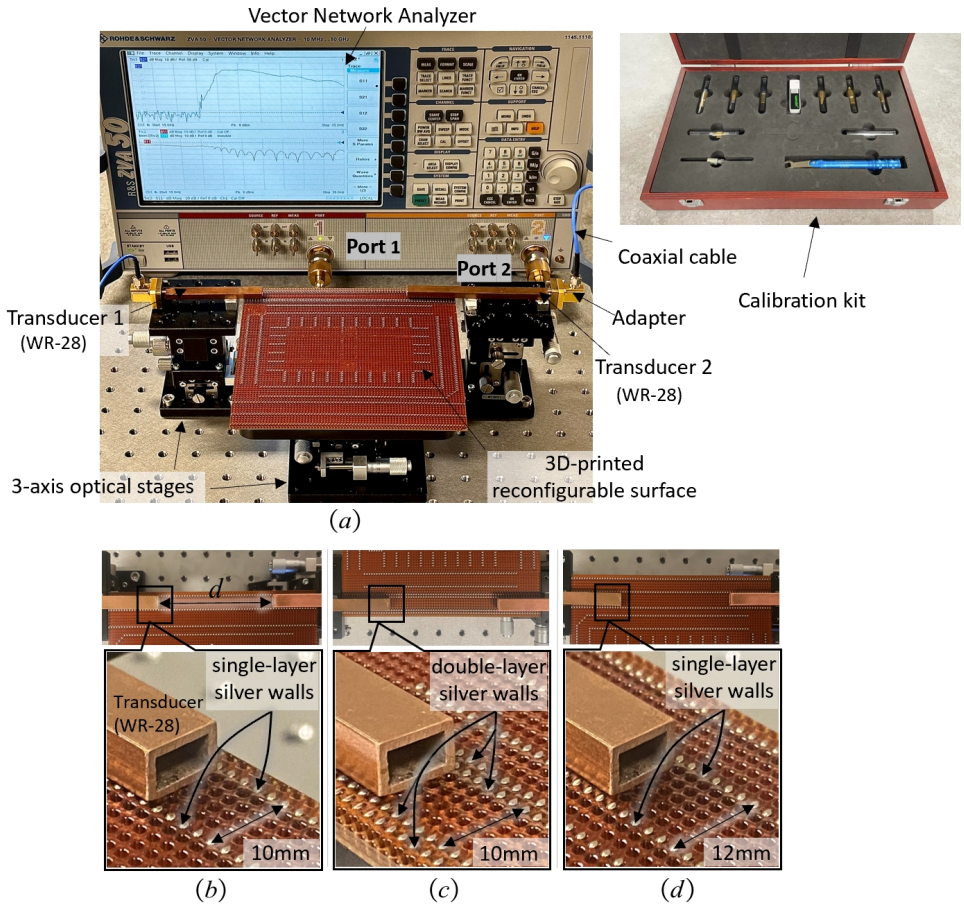

Figure 4.1: The measurement setup for (a) a 3D-printed reconfigurable surface wave platform prototype where the straight surface wave pathway is formed by (b) the single-layer silver walls or (c) double-layer silver walls with a pathway width of 10 mm or (d) single-layer silver walls with a pathway width of 12 mm. It also show the vector network analyzer (VNA) and the calibration kit.

4.2 Measurement Setup

4.2.1 Operation of Experimental Equipment

Firstly, Fig. 4.1(a) illustrates the experimental setup of the proposed reconfigurable surface wave platform prototype connected to a Vector Network Analyzer (VNA). Here, the dual-port VNA serves as the signal generator—an instrument meticulously designed for thorough microwave scanning across a wide frequency spectrum within electromagnetic systems. The VNA excels in providing precise measurements of signal transmission and reflection characteristics. Its functionality revolves around the synthesis of a sweeping frequency, allowing for the direct

Table 4.1: Parameters in the measurements and simulations for straight pathways.

Parameter	Value
operating frequency, f	$26, 28, 30\,\text{GHz}$
transducer (WR-28) frequency band, f_b	$21 - 42\,\text{GHz}$
height of transducer aperture, h_a	$3.566\,\text{mm}$
width of transducer aperture, w_a	$7.112\,\text{mm}$
thickness of transducer, l_a	$1\,\text{mm}$
WR-28 to 2.92mm coaxial adaptor,	$26.5 - 40\,\text{GHz}$
	VSWR: 1.2:1 (Typ.)
relative permittivity of PTFE layer, ε_r	2.1
effective permittivity of PTFE layer, $\varepsilon_r^{\text{eff}}$	1.86
loss tangent of low-loss PTFE, $\tan\delta$@26 GHz	0.00005
loss tangent of PTFE, $\tan\delta$@26 GHz	0.006
thickness of PTFE layer, h	$3\,\text{mm}$
relative permittivity of 3D-print resin layer, ε_r	2.8
effective permittivity of 3D-print resin layer, $\varepsilon_r^{\text{eff}}$	2.4
loss tangent of 3D-print resin, $\tan\delta$@26 GHz	0.0155
thickness of 3D-print resin layer, h	$2\,\text{mm}$
pathway width, w_c	$10, 12\,\text{mm}$
radius of cavity, r	$0.5\,\text{mm}$
center-to-center separation between cavity, w_s	$2\,\text{mm}$
surface porosity, ρ	19.63%
propagation distance, d	$50 - 150\,\text{mm}$
thickness of the metal ground, h_m	$0.05\,\text{mm}$
electrical conductivity of silver ink, σ_s	3.15×10^6 S/m
electrical conductivity of Galinstan, σ_g	3.46×10^6 S/m
vacuum permittivity, ε_0	8.854×10^{-12} F/m
surface impedance in the freq. band, Z_s	$j240 - j330\Omega$

computation of crucial network parameters, notably the input reflection coefficient (S_{11}) and transmission coefficient (S_{21}) [111]. Port 1 functions as the transmitting terminal, while Port 2 operates as the receiving terminal.

Notably, the S_{21} parameter is ascertained by the VNA through the transmission of a known test signal, followed by the measurement of the corresponding output signal. This computational process reveals the transmission loss and phase variation of the signal traversing from Port 1 to Port 2. The formula governing the computation of S_{21} in the VNA is articulated by the $S_{21} = 20\log_{10}\left(\frac{V_{\text{out}}}{V_{\text{in}}}\right)$. In subsequent experimental section of this thesis, S_{21} measurements obtained from the VNA are predominantly leveraged to scrutinize the attenuation and insertion loss incurred by

electromagnetic signals propagating as surface waves on a substrate. These empirical measurements are subsequently juxtaposed with S_{21} curves derived from simulation software CST to authenticate the experimental findings.

Furthermore, the experiments conducted in this thesis are all within a near-field environment using the VNA, where errors introduced by connectors, cables, adapters, or other components may impact measurement accuracy. This is due to the potential variability in the physical states of these components over time, influenced by factors such as temperature. Therefore, performing calibration before each usage ensures that the instrument can consistently provide reliable measurement results across different environments and conditions. The calibration process involves adjustments to the VNA using a calibration kit, as illustrated in Fig. 4.1(a), encompassing open, short, and load calibrations to establish an accurate baseline. Open calibration is performed using unconnected ports, short calibration involves shorting the ports, and load calibration employs a known impedance load.

By executing these calibrations, the instrument can accurately compensate for systematic errors during actual measurements, thereby improving the reliability and precision of the measurements. In the subsequent sections of this chapter, the experiment's actual S_{21} measurement data is presented. A meticulous comparison with S_{21} data obtained from a completely ideal CST simulation environment is conducted, revealing an agreement between the experimental and simulated result curves, with an overall error not exceeding 0.3 dB. This attests to the high accuracy of the actual S_{21} measurement data, establishing it as a trustworthy foundation.

4.2.2 Selection of Working Frequency Point

In the majority of experiments and simulations conducted in this thesis, the frequency point of 26 GHz has been chosen as the primary analytical frequency. This selection aligns with the current European deployment of 5G in millimeter-wave bands. According to specifications from the European Telecommunications Standards Institute (ETSI), particularly in ETSI TR 138 913 [112], the millimeter-wave frequency bands, especially the 26 GHz band, are deemed to possess ample spectrum resources capable of supporting larger bandwidths, thereby providing higher

data transmission speeds. The 26 GHz band has also received corresponding spectrum allocation in Europe, offering regulatory and spectral support for its deployment in 5G networks [113].

Furthermore, the choice of 26 GHz over other 5G frequency bands, such as 3.5 GHz, is motivated by the fact that the 26 GHz electromagnetic waves, being in the high-frequency range, have a smaller wavelength of 11.5 mm. This allows for the design of smaller surface dimensions in the laboratory to meet the measurement requirements of 10-30 times the wavelength, facilitating easier and more cost-effective testing in a lab environment. The dimensions of the 3D-printed surface in this experiment are 160 mm × 160 mm (14λ in@26 GHz), a size deemed sufficient to measure the performance of surface waves in a laboratory setting.

4.2.3 3D-Printed Surface and Experimental Environment

The measured prototype is manufactured using a high lossy 3D-printed dielectric resin ($\varepsilon_r = 2.8$ and $\tan\delta = 0.0155$@26 GHz) and silver ink ($\sigma_s = 3.15 \times 10^6$ S/m) [114]. It should be noted that the resin surface, with significantly high loss tangent, is solely used for sample measurements in this study. For practical application scenarios, it is recommended to employ a low-loss commercial PTFE surface with a loss tangent value of 0.00005 to effectively reduce losses, as discussed in Section 3.4.3. To demonstrate the concept and simplify the peripherals, columnar silver ink is utilized as the fluid metal, as shown in Fig.4.1$(b)-(d)$, and is printed into the dielectric layer and connected to the ground silver layer. The electrical conductivity of the silver ink is approximately 8.9% lower than that of Galinstan. Nevertheless, as shown in Section 3.4.1, different electrical conductivity of metal pins or walls have negligible impact on the short-distance transmission. The center-to-center separation between two silver columns is defined as the pathway width w_p of the straight pathway. To match the pathway width in this study, two commercial WR-28 rectangular waveguides with a thickness of 1 mm are chosen as transducers, positioned at both ends of the pathway. The transducers are mounted on three-axis optical linear stages, allowing for precise movement to change the propagation distance d. The VNA is connected to the transducers via coaxial cables. It should be noted that there

is a gap of approximately 0.5 mm and the bottom thickness of the WR-28, which can result in significant insertion loss close to 8 dB. This issue can be effectively addressed by incorporating a specially designed waveguide to achieve tight coupling to the surface, as described in [25]. And this chapter focuses more on the propagation characteristics of surface waves on the reconfigurable surface rather than the matching issue. The complete physical dimensions of this 3D-printed reconfigurable surface are presented in Table 4.1.

4.3 Measurement and Simulation Results

4.3.1 Straight Pathway

4.3.1.1 Path Loss in the Physical Environment

As shown in Fig.4.1, the position of Transducer 2 can be adjusted by shifting the optical linear stage to measure the received power at different distances from Transducer 1. Fig.4.2 presents the measured and simulated S_{21} results for a straight pathway with a width of w_p = 10 mm created by a single-layer of silver walls. The results cover a propagation distance d ranging from 50 mm to 150 mm with a sampling interval of 20 mm. The 3 dB half-power bandwidth of S_{21} is approximately 3.5 GHz, ranging from around 23.7 GHz to 27.2 GHz, with the peak occurring at 25 GHz as seen in Fig. 4.2.

The results indicate that S_{21} decays as the frequency increases, as the surface impedance deviates from the optimal value for efficient surface wave excitation [25]. The loss tangent of the dielectric material also increases with frequency, leading to higher E-field losses at higher frequencies. Additionally, it can be observed that the measurement and simulation results are generally consistent. However, the measured S_{21} values are slightly lower than the simulation results below approximately 25 GHz. This could be attributed to the cut-off frequency of the coaxial-to-waveguide adapters used in the measurements [115], while in the simulations, the waveguide ports are directly connected to the transducers. Furthermore, the set of S_{21} curves gradually decreases as the distance increases across the bandwidth.

At 26 GHz, the S_{21} value steadily decreases from −13.7 dB at a propagation

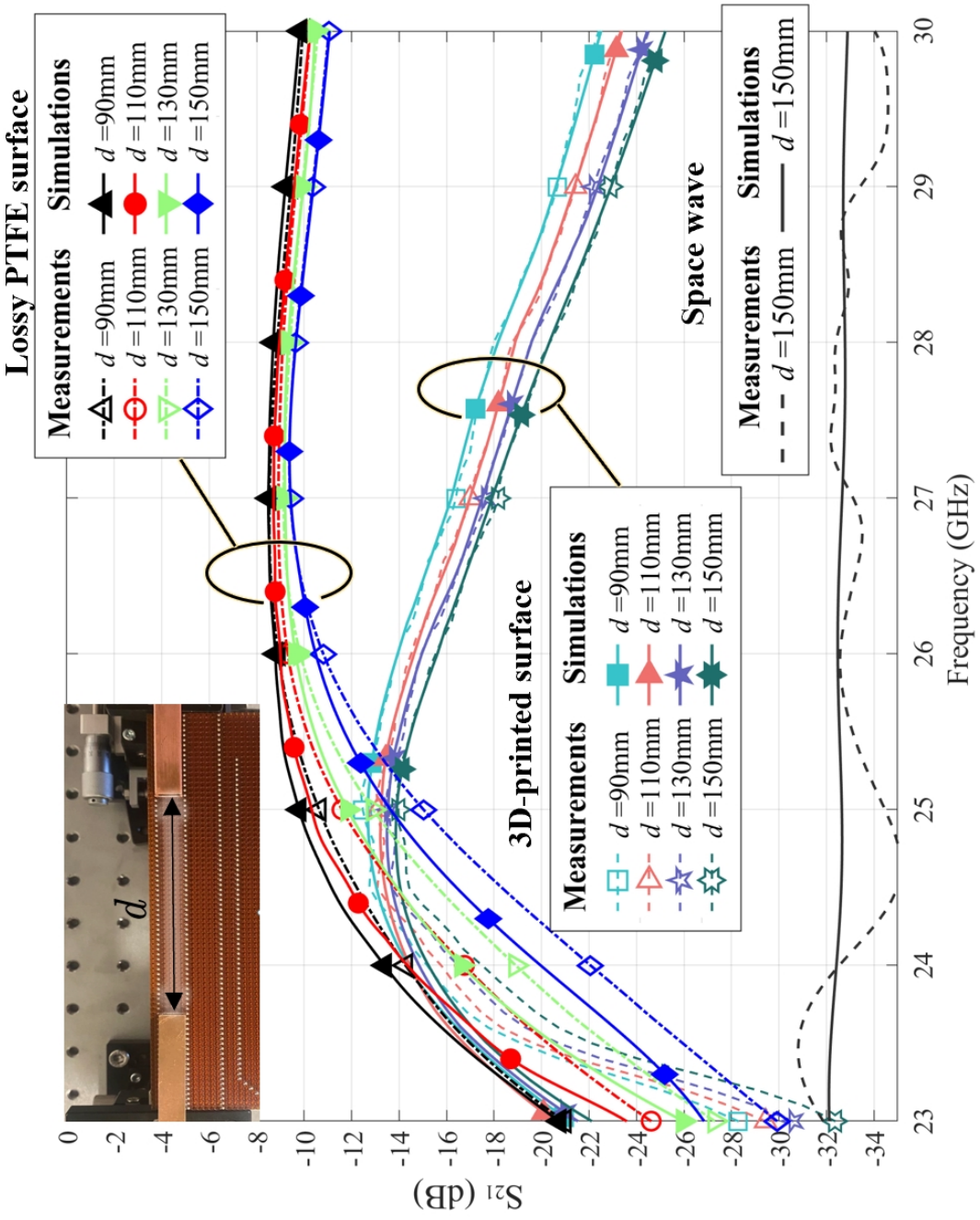

Figure 4.2: S_{21} results for measurement and simulation inside the straight pathway for various propagation distance d from 50 mm to 150 mm.

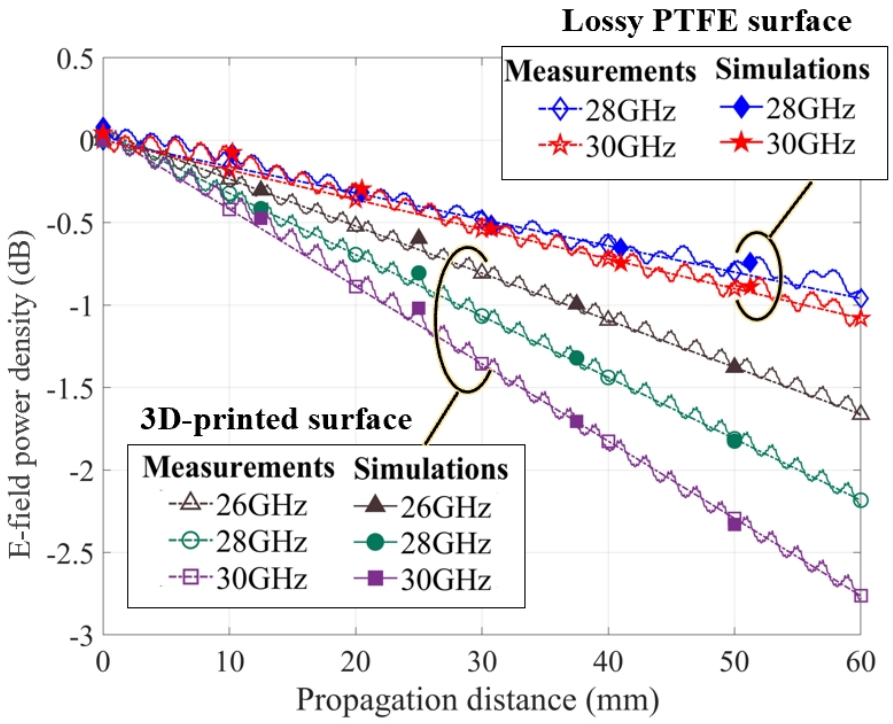

Figure 4.3: The E-field power density in a straight pathway against the propagation distance for different frequency.

distance of 50 mm to −16.5 dB at 150 mm, resulting in a total attenuation of 2.8 dB over a distance of 100 mm. The normalized results (assuming the initial reference point at $d = 50$ mm) are plotted in Fig. 4.3, where the measurement and simulation results are compared. And results at 28 GHz and 30 GHz are also included for reference.

In Fig.4.1, the adjustability of Transducer 2 is achieved by shifting the optical linear stage in the $+z$-direction, facilitating the measurement of S_{21} at varying propagation distances from Transducer 1. Moving to Fig.4.2, it illustrates both measured and simulated S_{21} results for straight pathways with common PTFE and 3D-printed resin. The pathways, featuring a width of 10 mm and single-layer silver walls, span a propagation distance d from 90 mm to 150 mm with a 10 mm sampling interval.

The presented results in Fig. 4.2 demonstrate a decay in S_{21} for both common PTFE and 3D-printed surfaces within the frequency range of 23 GHz to 30 GHz, corresponding to the proposed 5G millimeter-wave frequency band. Two primary

reasons contribute to this decay. Firstly, the surface impedance deviates from its optimal value for efficient surface wave excitation at different frequencies, with common PTFE exhibiting lower susceptibility due to its lower dielectric constant. This is evident in the wider 3-dB half-power frequency bandwidth of common PTFE compared to the 3.5 GHz bandwidth (23.7 to 27.2 GHz) provided by the 3D-printed surface. Secondly, the dielectric loss tangent increases with frequency, resulting in lower S_{21} at higher frequency bands. Notably, the loss tangent of the 3D-printed surface shows a more frequency-sensitive decay, with an optimal frequency around 25 GHz to 26 GHz, corresponding to the peak of the S_{21} curve.

Examining the gradient of the lines, it is evident that the loss tangent of the 3D-printed surface exhibits a faster decay with increasing frequency. Despite generally consistent measurement and simulation results, experimental S_{21} values are slightly lower than simulations below approximately 25 GHz. This difference may be attributed to the cut-off frequency of the two coaxial-to-waveguide adapters (Table 4.2) connected to the transducers in measurements [115], while in simulations, waveguide ports are directly connected to the transducers. Additionally, the set of S_{21} curves gradually decreases as the distance increases across the frequency band.

At 28 GHz, the S_{21} value of the PTFE-platform steadily decreases from -9.22 dB at a propagation distance of 90 mm to -10.13 dB at 150 mm, resulting in a total attenuation of 0.91 dB over a distance of 60 mm, equating to 0.15 dB per 10 mm. In Fig. 4.3, normalized results (assuming the initial reference point at $d = 150, \text{mm}$) are presented, comparing measured results and CST simulation. Results at 30 GHz are also included for reference. Once again, the measurement and simulation results exhibit excellent agreement with negligible discrepancies. Therefore, the validity of the measurement results is demonstrated by the above findings.

Additionally, Fig. 4.4 illustrates the simulation results at 26 GHz. The simulation assumes a straight pathway of 2 m and normalizes the results at a distance of 0.1 m. The pathway is formed by using Galinstan walls with different dielectric surfaces: low-loss PTFE ($\tan\delta = 0.00005$), lossy PTFE ($\tan\delta = 0.006$), and high

Table 4.2: Comparison of different transmission modes and path losses

Transmission mode	Substrate material / Type	Working frequency, f (GHz)	Loss tangent, $\tan\delta$	Path loss, L (dB/m)
Reconfigurable surface wave pathway	Low-loss PTFE [116]	26	0.00005	0.84
Reconfigurable surface wave pathway	Lossy PTFE	26	0.006	14.5
Reconfigurable surface wave pathway	Lossy printed resin	26	0.0155	28.1
Reconfigurable transmission line [5]	Roger 6010	26	0.0023	14.2
Controllable mode transmission line [117]	Roger 4003	4	0.0027	6.25
Transmission microstrip line [118]	Roger 4350B	24	0.0037	17.1
Coaxial cable [119]	Sucoflex-103	26	—	1.65
Coaxial cable [120]	MaxGain-130	26	—	2.56

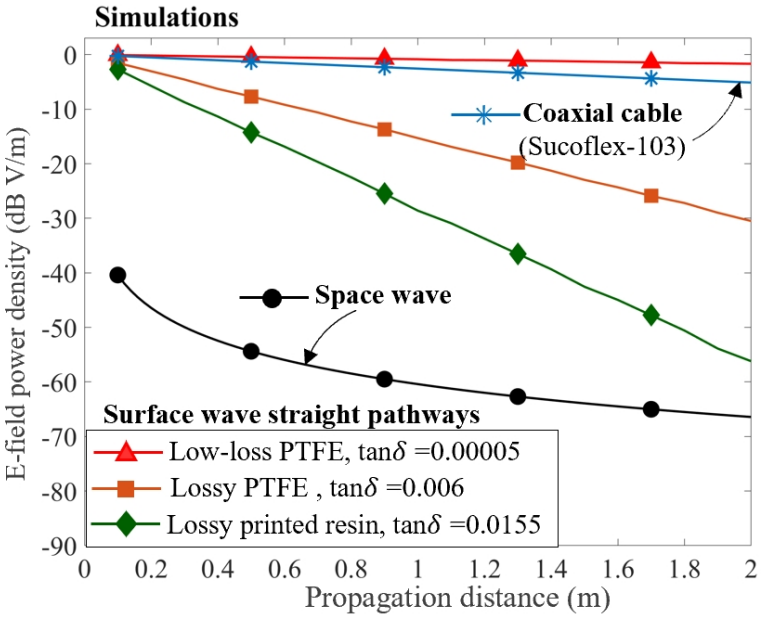

Figure 4.4: The E-field power obtained from the simulation results assumes a straight pathway of 2 m created by Galinstan walls, with different dielectric surfaces: low-loss PTFE ($\tan\delta = 0.00005$), lossy PTFE ($\tan\delta = 0.006$), or lossy 3D-printed resin ($\tan\delta = 0.0155$). A coaxial cable (Sucoflex-103) is also included for comparison.

lossy printed resin ($\tan\delta = 0.0155$). A coaxial cable (Sucoflex-103) is also included for comparison. It can be observed that selecting a surface with a lower loss tangent effectively reduces the path loss in the reconfigurable surface wave pathway. Table 4.2 presents the path loss values for different surfaces with varying loss tangents in the surface wave pathway, namely 0.84 dB/m, 1.32 dB/m, and 28.1 dB/m. Furthermore, the path losses for the reconfigurable transmission line ($\tan\delta = 0.0023$) and the transmission microstrip line ($\tan\delta = 0.0037$) are 14.2 dB/m and 17.1 dB/m, respectively. It is evident that surfaces with lower loss tangents, such as PTFE, effectively mitigate path losses. Therefore, reconfigurable surfaces based on surface waves hold potential for applications in short-distance network-on-chip communication and long-distance relay outdoor wall communications, as discussed in Section 2.6.

Due to the convenience of directly incorporating silver pins into the pathway of 3D-printed substrates, creating diverse surface structures becomes more experimentally accessible. Subsequent experimental analyses will be mainly based on the utilization of 3D-printed substrates.

4.3.1.2 Effect of Multi-Layer Metal Walls

The effect of using multi-layer metal walls to form the pathway are further investigated. Firstly, the setup with double-layer metal walls is considered, as shown in Fig.4.1(c), and the measurement and simulation results at several distances, including 50 mm, 110 mm and 150 mm for different frequencies are presented in Fig.4.5. It can be observed that the overall trend of S_{21} for the double-layer and single-layer configurations is very similar, with a slight increase of approximately 0.1 dB in S_{21} for the double-layer case. This indicates that the double-layer setup slightly outperforms the single-layer in confining the signal within the pathway, as the additional layer enhances the boundary's ability to block signal leakage.

And then Fig. 4.6 illustrates the relationship between E-field power decay and distance, including the simulation results for three-layer and four-layer metal walls. It can be seen that the power decay for three-layer and four-layer metal walls is very close to that of the double-layer walls, with a difference of less than 0.05 dB.

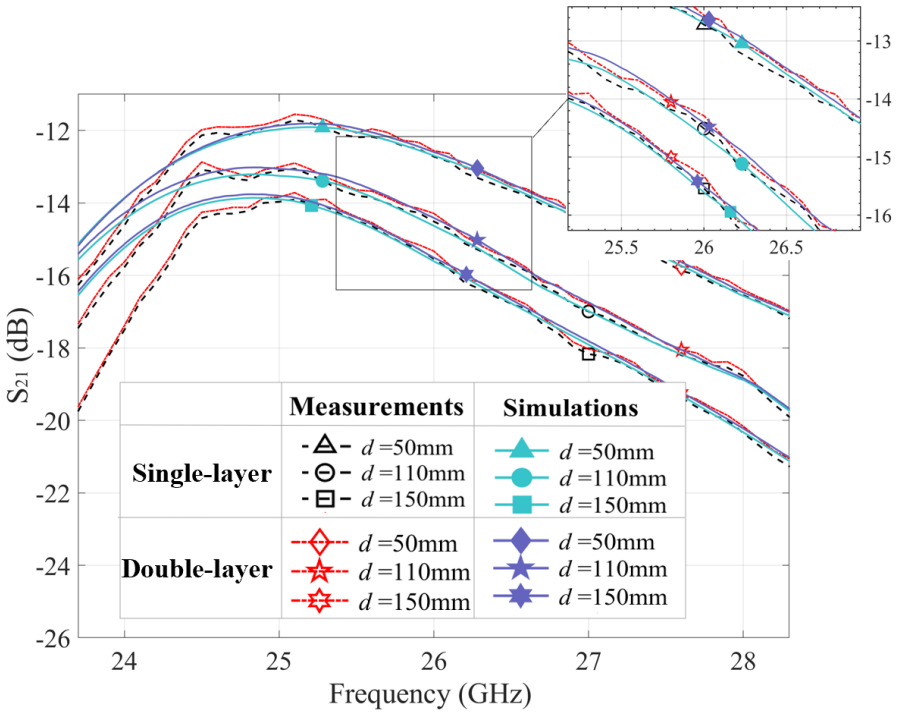

Figure 4.5: The S_{21} results in a straight pathway formed by single-layer or double-layer silver walls in the measurements and simulations with a propagation distance $d = 50\,\text{mm}$, $110\,\text{mm}$ and $150\,\text{mm}$.

This suggests that the signal improvement achieved by adding more layers is minimal. Finally, based on above measurement and simulation results, both single-layer and double-layer metal wall structures are capable of creating highly isolated pathways and effectively guiding surface waves. Adding additional layers beyond the double-layer configuration does not significantly enhance the signal performance. Therefore, for the design and manufacturing of reconfigurable surface pathways, it is sufficient to choose either a single-layer or double-layer metal wall structure, depending on the specific requirements and constraints. This simplifies the overall design and fabrication process.

4.3.1.3 Pathway Width and Operating Frequency

As shown in Fig.4.1(d), the pathway width w_p is increased from $10\,\text{mm}$ to $12\,\text{mm}$ using two single-layer metal walls. Fig.4.7 presents the measured and simulated S_{21} curves, along with the simulated results for $w_p = 14\,\text{mm}$ and $16\,\text{mm}$ at a fixed

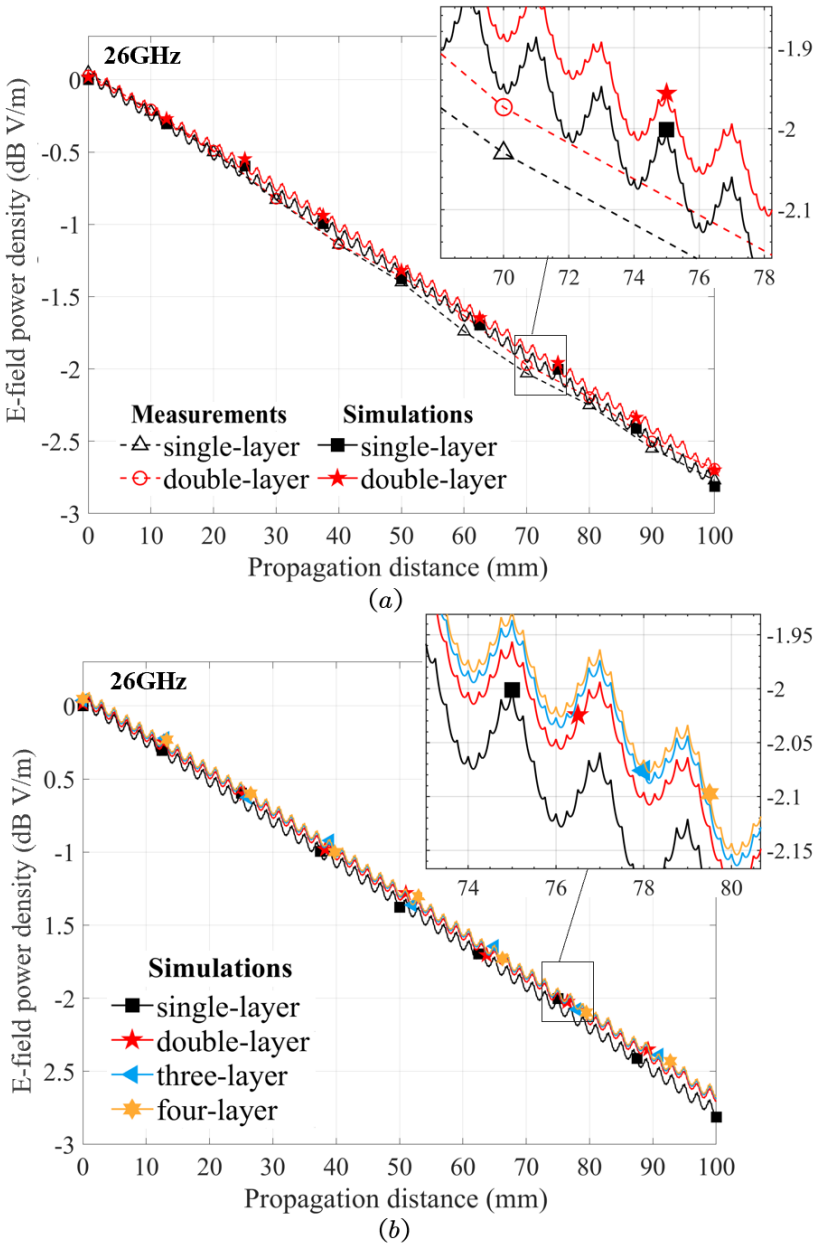

Figure 4.6: The E-field power in a straight pathway against the distance after normalization for the (a) measurements and simulations containing single-layer, double-layer and (b) multi-layer walls results at 26 GHz.

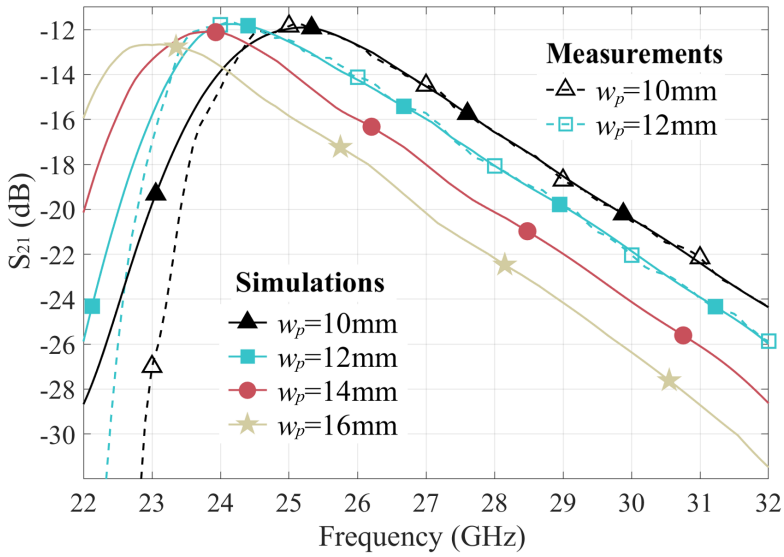

Figure 4.7: Measurement and simulation results in different pathway widths of 10 mm, 12 mm, 14 mm and 16 mm with a propagation distance $d = 50$ mm.

propagation distance of $d = 50$ mm. The results indicate that as the pathway width increases, the S_{21} curves shift to lower frequencies. The optimal operating frequency of the surface changes from 25 GHz at 10 mm to 24.2 GHz at 12 mm, then to 23.7 GHz at 14 mm and 23 GHz at 16 mm. This suggests a positive correlation between the appropriate pathway width and the signal wavelength.

Furthermore, the pathway width exhibits frequency selectivity properties for the surface wave. By changing the pathway width on this reconfigurable surface, it becomes possible to filter and split signals at different carrier frequencies. Additionally, a slight decrease in S_{21} can be observed as the pathway width increases, which may be attributed to signal leakage at the transducer-to-surface interface. Therefore, it is preferable for the pathway width to be closer to the width of the transducer (in this case, $w_a = 7.1$ mm) to minimize leakage. Overall, these findings highlight the significance of the pathway width in shaping the behavior of surface waves on the reconfigurable surface, including frequency selectivity and signal confinement.

4.3.1.4 Porosity of Surface

Moreover, the six porosity patterns with different porous geometry, referred to as Model 0 to Model 5, are considered in Fig. 4.8. The parameter w_v, which represents

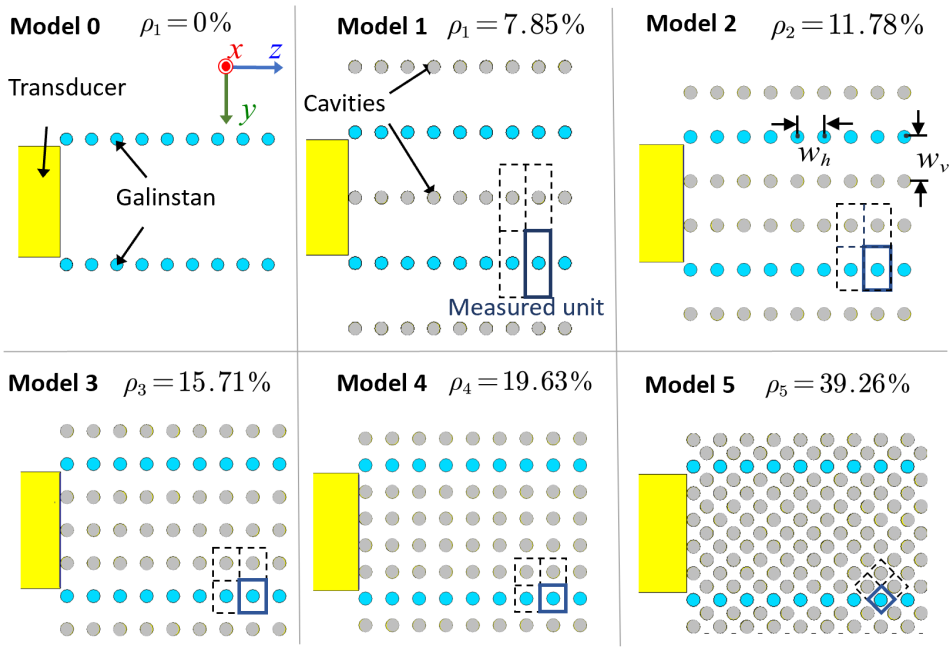

* Porosity is defined as $\rho = S_{\text{cavity}}/S_{\text{measured-unit}}$.

Figure 4.8: Models with different cavity distribution densities, i.e., porosity patterns.

the vertical center-to-center distance between adjacent cavities or metal pins, can be modified to determine different values of porosity, while the horizontal distance w_h keeps a same value. Porosity is defined as $\rho = S_{\text{cavity}}/S_{\text{measured-unit}}$, where S_{cavity} denotes the top area of each cavity and $S_{\text{measured-unit}}$ is the top area of the measured unit (the rectangular region marked in the figure). A type of lossy PTFE ($\varepsilon_r = 2.1$, $\tan\delta = 0.0002$) is used as the dielectric layer, and the effective relative permittivity $\varepsilon_r^{\text{eff}}$ of this surface will change with the porosity ρ and can be calculated according to 3.2. To maintain consistency, the surface impedance Z_s in all models is set to $j270\Omega$, which can achieve significant surface wave excitation efficiency. And then it can be accomplished by adjusting the thickness h_d of the dielectric layer appropriately to match different porosities while maintaining a fixed surface impedance. The corresponding parameter values are presented in Table 4.3.

Fig. 4.9 demonstrates a set of E-field distribution results over the surface of Model 0 – 5 inside the straight pathway localized by the Galinstan pins normalized based on mathematical theoretical value of Galinstan wall pathway in Section 3.3.2. The results show much fluctuation caused by standing wave reflection and diffrac-

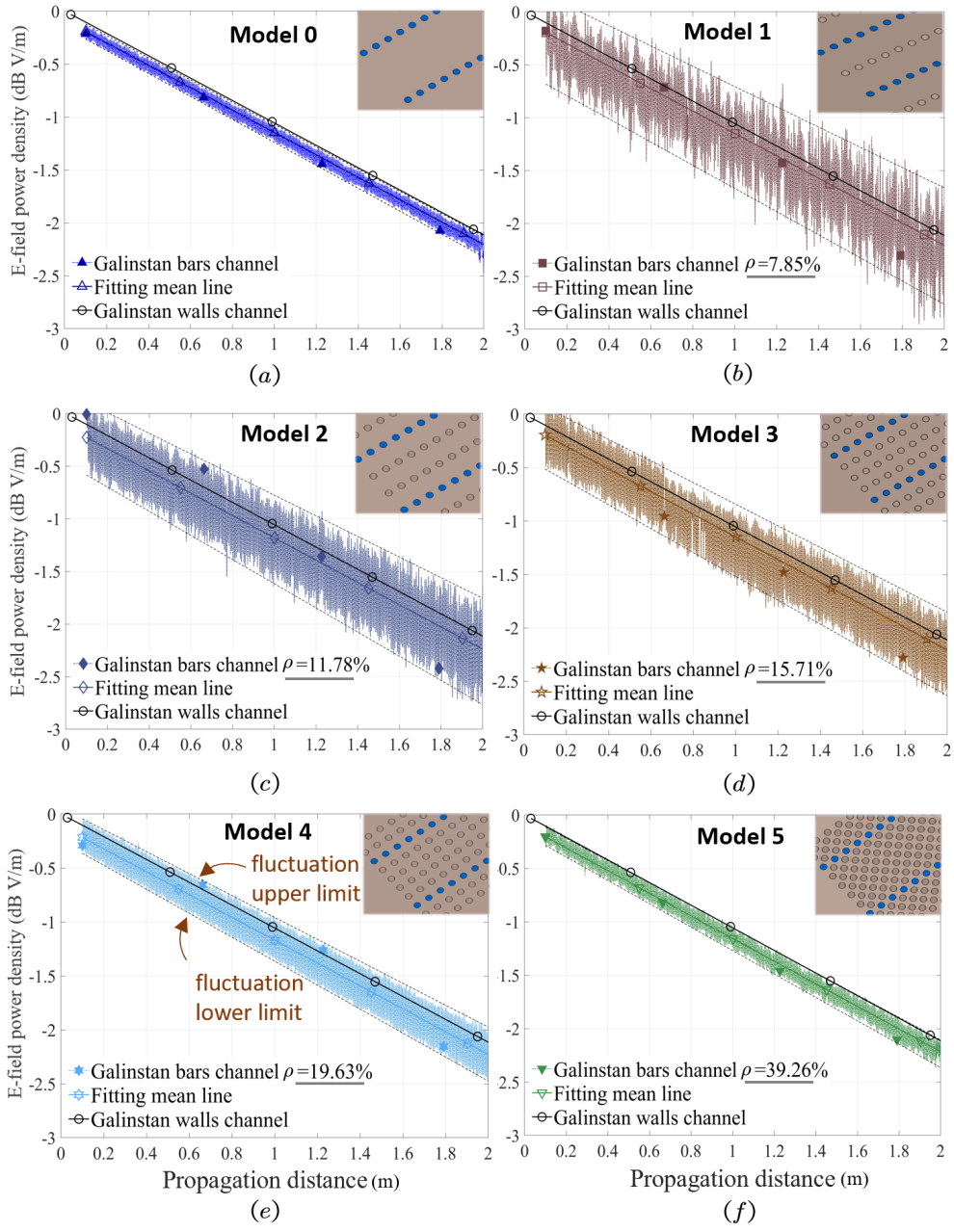

Figure 4.9: The E-field power results after normalization for the reconfigurable surface with (a) only the Galinstan pin pathway, (b) the Galinstan pin pathway with porosity $\rho = 7.85\%$, (c) $\rho = 11.78\%$, (d) $\rho = 15.71\%$, (e) $\rho = 19.63\%$, and (f) interleaved cavities with $\rho = 39.26\%$.

Table 4.3: Parameter variations in the comparative models

Model	Vertical separation w_v(mm)	Horizontal separation w_h(mm)	Porosity $\rho(\%)$	Effective permittivity $\varepsilon_r^{\text{eff}}$	Thickness h(mm)
0	–	–	0	2.10	2.50
1	5.00	2	7.85	2.00	2.63
2	3.33	2	11.78	1.95	2.69
3	2.50	2	15.71	1.91	2.77
4	2.00	2	19.63	1.86	2.85
5	1.41	2	39.26	1.63	3.40

tion from the cavities. To facilitate comparison with the case without the cavities shown in Fig. 4.9(a), all the numerical means lines of the Model $1-5$ are plotted as well. Table 4.4 provides the standard deviation (SD) of the E-field fluctuation, σ, and the path loss L of each model. It can be seen that as the porosity ρ increases, the fluctuation of the signal decreases. That is, the fluctuation SD, σ, decreases gradually from 0.297 to 0.070 from Model 1 to Model 5 as the surface porosity increases from 7.85% to 39.26%, suggesting that a surface with evenly denser cavities helps reduce the signal fluctuation in surface wave propagation, approaching closer to Model 0 which has a signal fluctuation SD of just 0.052. Additionally, the discrepancy in path losses in different models is below 0.05 dB in a 2000 mm (173.3λ at 26 GHz) propagation distance, indicating that potential loss caused by the porosity is negligible if the surfaces are kept at the same surface impedance. Particularly, It is noticed in Model 5 that the use of proposed reconfigurable interleaving porous surface with an even 1.41 mm cavity separation could be effectively instrumental to the subduction of E-field fluctuation. More cavity density means more combination possibilities and these staggered cavities filled with Galinstan could provide a more flexible pathway generation containing turns with different angles and positions for the realization of reconfigurable surface waves.

This section can be summarized by studying the broadband performance of the reconfigurable surface with interleaved cavities, i.e., Model 5. Fig. 4.10(a) shows the S_{11} and S_{21} results in the frequency range of 20 GHz to 35 GHz. The results

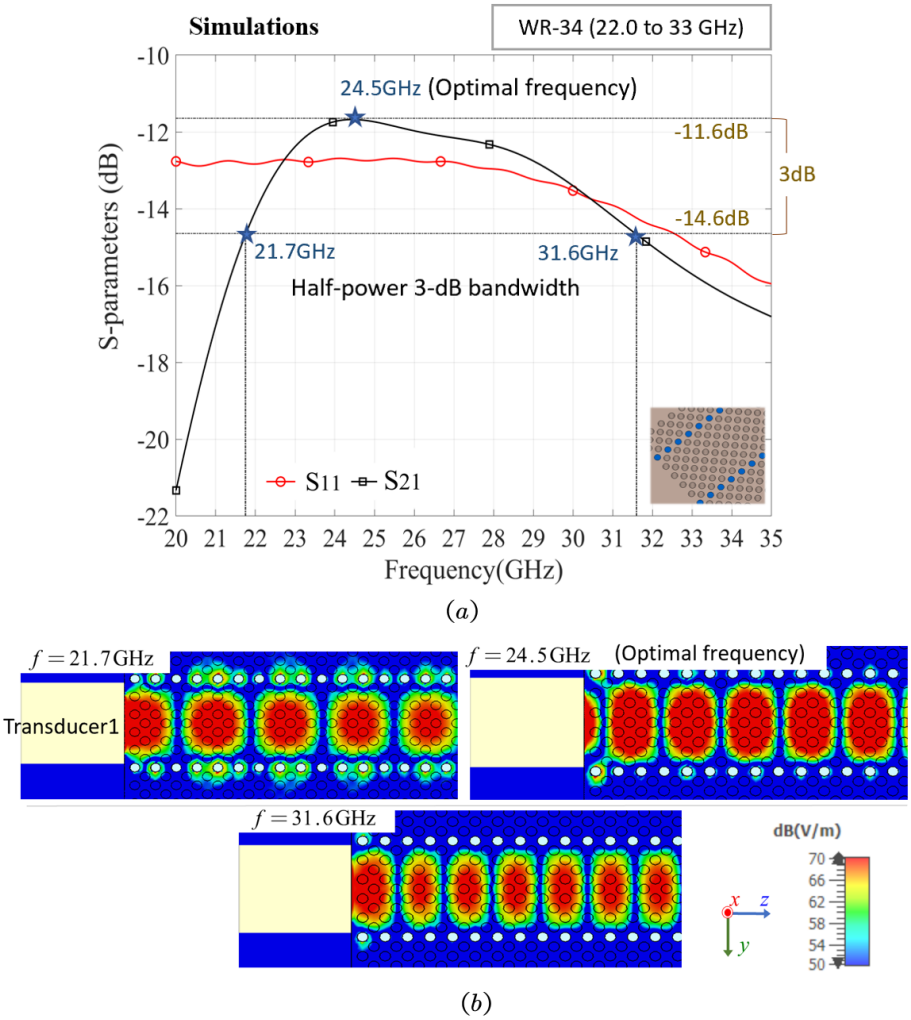

Figure 4.10: (a) The S_{11} and S_{21} simulation results for the interleaving porous surface operating in a wide frequency band from 21.7 GHz to 31.6 GHz and (b) the simulation results at 21.7 GHz, 24.5 GHz and 31.6 GHz.

indicate that the peak, corresponding to the optimal frequency, occurs at 24.5 GHz with S_{21} measured at -11.6 dB. Furthermore, the half-power 3-dB bandwidth is determined to be from 21.7 GHz to 31.6 GHz, which may be limited by cut-off frequency of the transducer at 22 GHz and 33 GHz. And as shown in Fig. 4.10(b), the simulation results demonstrate the capability of this pathway to guide surface waves at different frequencies. In summary, the porous reconfigurable surface operates in a broadband range, although it still requires adjustments in thickness to match the transducer's different operating frequencies in specific applications and maintain the appropriate surface impedance.

Table 4.4: Signal fluctuations and path losses of different models.

Model	Porosity, ρ(%)	Fluctuation SD, σ	Path loss, L(dB /m)
0	0	0.052	1.10
1	7.85	0.297	1.12
2	11.78	0.265	1.13
3	15.71	0.221	1.10
4	19.63	0.131	1.11
5	39.26	0.070	1.12

[1] SD is the standard deviation, $\sigma = \sqrt{\frac{\sum (x_i - \mu)^2}{n_t}}$.

[2] n_t is the number of data samples, x_i is the value of each sample and μ is the value of the local mean.

[3] Path loss L is measured using the numerical mean line in each model.

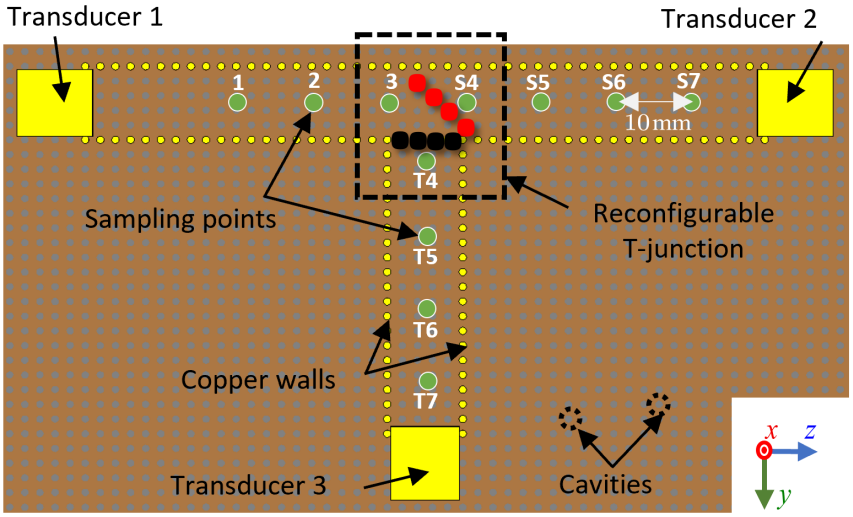

Figure 4.11: Illustration of a T-junction reconfigurable surface structure for guiding the surface wave along different propagation direction

4.3.2 Turn Pathway

4.3.2.1 Turn Pathway Model

The preceding chapter has examined the propagation characteristics of surface waves along the straight pathway. Building upon this, the current chapter delves into an investigation of the factors that impact surface wave propagation within the turn pathway on the reconfigurable surface wave platform. To provide a understanding of the turn pathway concept, the experimental setup employed in this chapter in-

corporates a 3D-printed surface, which is detailed in Section 4.2. Within the central region of the surface, where only cavities are present, copper ($\sigma_c = 59.6 \times 10^6$ S/m) pins with the same radius r as the cavities are directly utilized to create distinct propagation pathways for convenient evaluation of the surface's performance. Fig. 4.11 illustrates a T-shaped reconfigurable surface with an adjustable junction, enabling the positions of the metal pins to be altered, thereby switching the direction of surface wave propagation between a straight and a 90°-turn pathway.

In the simulation model, E-field sampling probes labeled as $1-$S7/T7, marked in green, are placed along the center lines of the straight and 90°-turn pathways. By inserting copper pins into the black-marked cavities, the surface wave propagates from Transducer 1 to 2, while being prevented from reaching Transducer 3, thereby forming a straight propagation pathway. Conversely, when the pins are repositioned along a red-marked 45° line to guide the signal at the T-junction, the surface wave can be directed from Transducer 1 to 3 through a 90°-turn, but it cannot reach Transducer 2, thereby establishing a turn propagation pathway.

4.3.2.2 Reconfigurable Pathways

The reconfigurable pathway in this surface is formed by adjusting the straight and the turn propagation pathway, as depicted in Fig. 4.12(a) and (b), respectively. It is evident that this T-junction effectively regulates the direction of surface wave propagation. The E-field curves exhibit a significant disparity of over 30 dB between the desired and undesired directions. These findings underscore the capability of the reconfigurable surface to efficiently guide a majority of surface waves towards the desired receiver through dynamic pathway selection, while minimizing power in undesired directions. It is noteworthy that the measurement results were obtained by systematically shifting the optic stages from the transducer to the probe locations for sampling.

This T-junction configuration serves as a proof-of-concept, and ideally the fluid metal pins on the surface can be further utilized to create multiple junctions that facilitate the manipulation of surface wave propagation directions or circumvent obstacles. Additionally, a direct comparison between the straight pathway and the

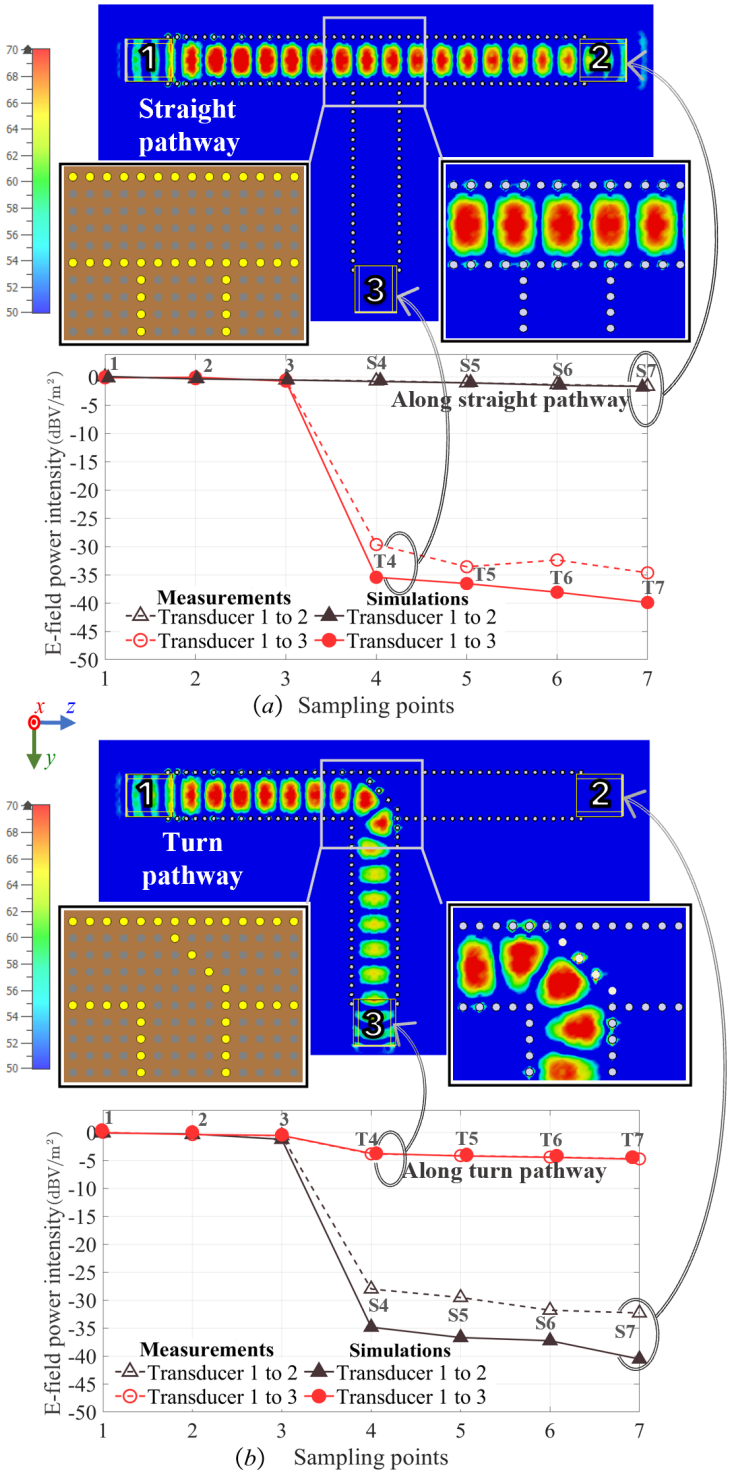

Figure 4.12: The measurement and simulation results for the surface waves along a (a) straight pathway from Transducer 1 to 2 or a (b) 90°-turn pathway from Transducer 1 to 3 by adjusting the shape of the T-junction.

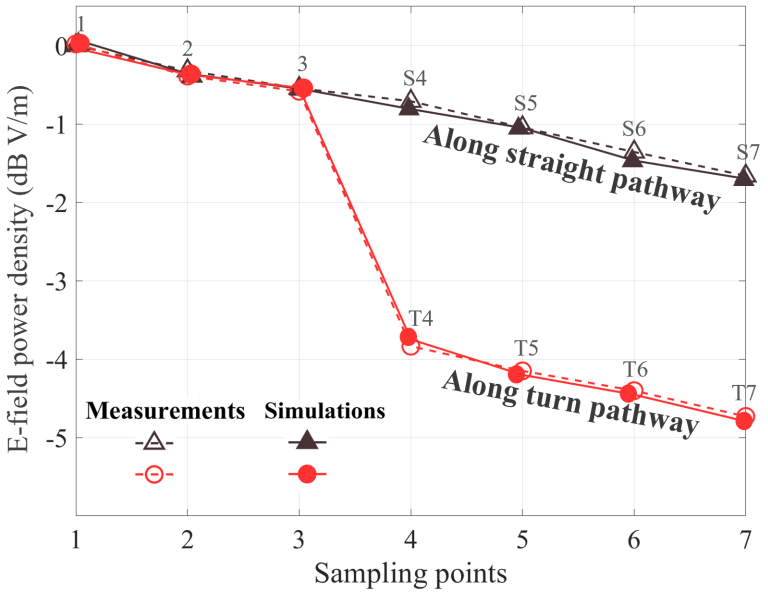

Figure 4.13: The comparison of the E-field power decay along the straight and 90°-turn pathway in measurement and simulation results.

90°-turn pathway can be made by analyzing the S_{21} results depicted in Fig. 4.13. The outcomes reveal an additional insertion loss of approximately 3.2 dB along the 90°-turn pathway, which is likely attributable to signal reflections at the turn. This phenomenon not only induces the formation of standing waves and amplifies signal fluctuations but also weakens the signal within the pathway. Furthermore, by adjusting the distribution of the metal pins in the junction to modify the corner geometry, it is possible to moderately reduce losses at the corners, as elaborated in the next section.

4.3.2.3 Corner Optimization

To study the losses associated with different corner configurations, the T-junction in Fig. 4.11 can be replaced with corners of varying shapes in a 90°-turn pathway for measurement, as illustrated in Fig. 4.14(a). Corner 0 is used as a standard right angle turn reference, consisting of inner and outer metal walls both at 90°. Corner 1 is similar to Corner 0, but with the outer vertex pin removed and the shapes of the pathway in Corner 0 and Corner 1 being the same, see the S_{21} results in Fig. 4.14(b). Here, the distance from the inner vertex pin O to the center point A of the outer wall BC is defined as the corner width w_t. The corner width decreases as the outer wall

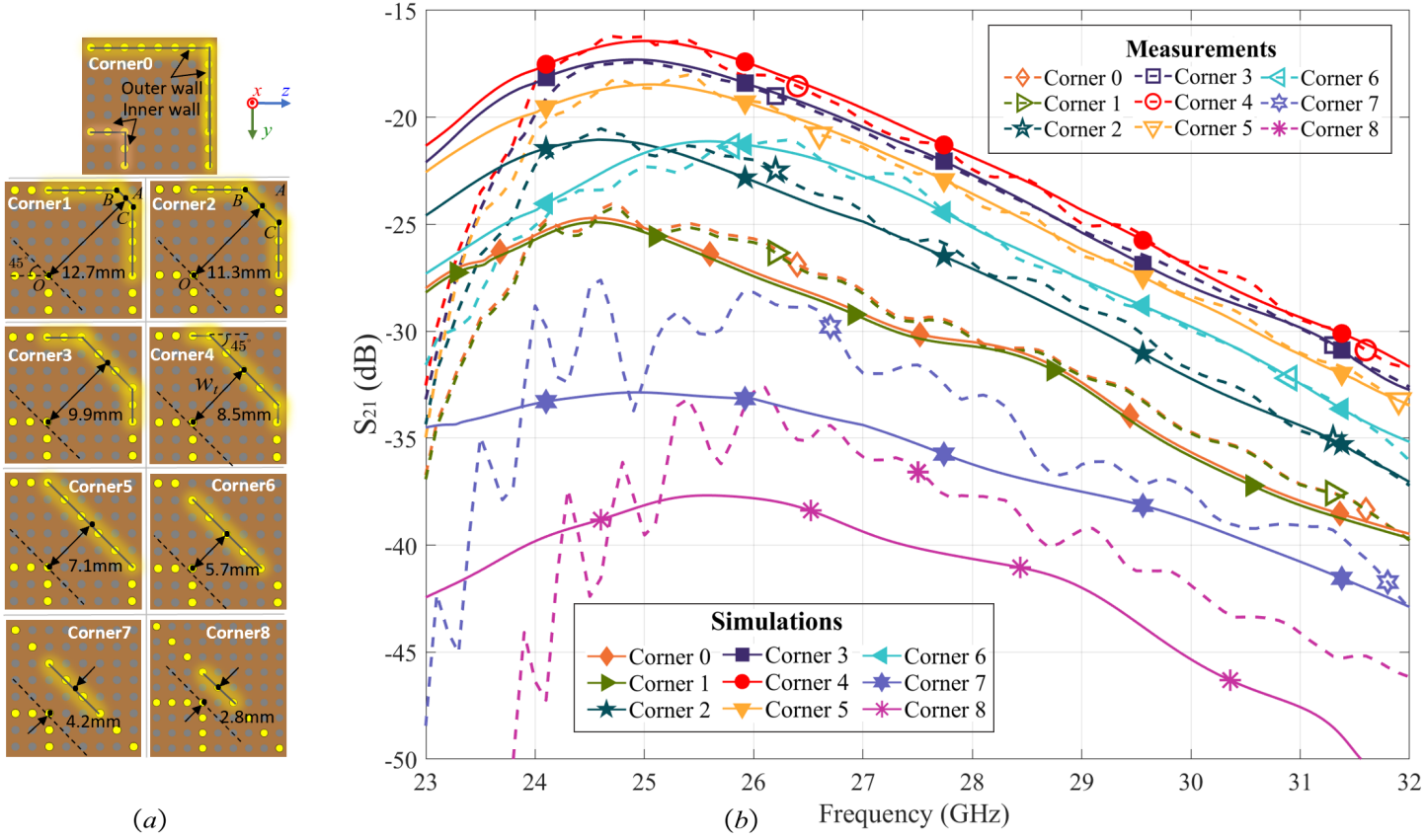

Figure 4.14: (a) A set of turn corners with different shapes and corner widths w_t by adjusting the outer metal wall location from Corner 1 to 8 and their (b) S_{21} measurement and simulation results.

Table 4.5: optimal frequencies of corners with different corner widths

Corner	1(0)	2	3	4	5	6	7	8
Corner width, w_t (mm)	12.7	11.3	9.9	8.5	7.1	5.7	4.2	2.8
optimal frequency (GHz)	24.4	24.5	24.9	25.0	25.1	25.6	26	26.1

BC gradually moves towards the inner wall from Corner 1 to 8.

The S_{21} results for these corners are shown in Fig. 4.14(b). The best-performing shape is Corner 4 ($w_t = 8.5\,\text{mm}$) with S_{21} of $-16.2\,\text{dB}$ at 25 GHz, which can be considered as the optimal operating frequency. This is followed by Corner 3 ($w_t = 9.9\,\text{mm}$) with S_{21} of $-17.4\,\text{dB}$ and Corner 5 ($w_t = 7.1\,\text{mm}$) with S_{21} of $-18.6\,\text{dB}$. All their corner widths w_t are close to the pathway width $w_p = 10\,\text{mm}$. It is also observed that the optimal operating frequency is 24.5 GHz in Corner 2 ($w_t = 11.3\,\text{mm}$) and 25.6 GHz in Corner 6 ($w_t = 5.7\,\text{mm}$), respectively. This discrepancy further illustrates the frequency selection characteristics that can be achieved by controlling the difference in pathway width. Therefore, signal separation based on frequency may be possible in different propagation directions at a junction or corner, which can be viewed as a signal filter. For Corner 7 ($w_t = 4.2\,\text{mm}$) with S_{21} of $-30\,\text{dB}$ and Corner 8 ($w_t = 2.8\,\text{mm}$) with S_{21} of $-33\,\text{dB}$, the attenuation looks much more significant. This is because the shrinking 45° outer wall results in more signal reflection and blockage due to the too small corner width. Note that in Corner 7 and 8, the E-field power is too small and similar to the level outside the pathway, leading to a larger discrepancy between measurement and simulation.

The optimal frequencies of corners with different corner widths are listed in Table 4.5. Fig. 4.15 shows the relationship between the corner width and the average S_{21} value in the half-power bandwidth based on their respective optimal frequency. It can seen that the S_{21} value of Corner 4 with $w_t = 8.5\,\text{mm}$ is higher than that of Corner 1 with $w_t = 12.7\,\text{mm}$ by over 15dB, indicating that the shape of the corner plays a significant role in guiding the surface wave around a 90°-turn. Moreover, Corner 4 performs slightly better than Corner 3 with $w_t = 9.9\,\text{mm}$, which is closer

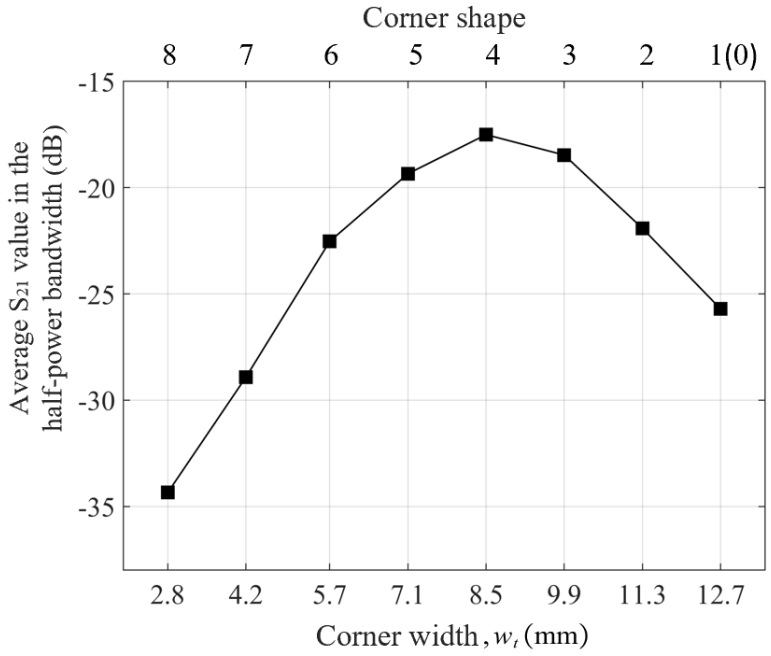

Figure 4.15: The relationship between corner width w_t and the average S_{21} value in the half-power bandwidth.

to the pathway width $w_p = 10\,\text{mm}$. This suggests that moderately decreasing the corner width, such as in Corner 4, will result in less loss under the premise of w_t approaching w_p in practice.

4.4 Conclusions

By conducting actual measurements on the reconfigurable surface wave platform using the 3D-printed prototype and lossy PTFE surface, this chapter offers valuable insights into the path loss characteristics of surface waves along the straight pathway across different frequencies. It reveals the existence of a minimum loss region near the optimal surface impedance, which corresponds to the optimal operating frequency. And at higher frequencies, the loss tangent of the dielectric material will increase, resulting in higher E-field power losses.

Besides, through a comparison of measurement and simulation results, it is found that both single-layer and double-layer metal wall structures provide highly isolated pathways, with the double-layer configuration slightly outperforming the

single-layer configuration. However, adding extra layers beyond the double-layer configuration does not significantly improve signal performance. Therefore, for the sake of simplifying the manufacturing process, it is recommended to choose either a single-layer or double-layer metal wall structure. Moreover, a positive correlation is observed between the appropriate pathway width and the signal wavelength, and the pathway width exhibits frequency selectivity characteristics for surface waves. The measured results show excellent agreement with the simulation results, with negligible discrepancies. Additionally, denser surface pore patterns are investigated as a means to reduce surface wave signal fluctuations.

Furthermore, the versatility of the reconfigurable T-shaped junction in enabling flexible surface wave propagation direction switching between a straight pathway and a 90° turn pathway is evident. Moreover, there is a substantial E-field disparity of over 30 dB observed between the desired and undesired directions, highlighting the pathway selection capability and crosstalk mitigation potential of the reconfigurable surface. Furthermore, the implementation of fluid metal on the surface facilitates the creation of multiple turns, enabling the manipulation of surface wave propagation direction and the circumvention of obstacles.

Moreover, varying corner configurations with different corner widths demonstrate distinct additional insertion losses, which play a crucial role in guiding surface waves through the turn pathway. The findings indicate that corners smaller than and closer to the pathway width minimize the insertion losses associated with each turn, resulting in an approximate value of 3.2 dB. It is anticipated that this value can be further diminished in future studies through the design of more suitable surface geometry.

The findings of this chapter preliminarily provide comprehensive analysis and confirmation of the effective operation of the proposed reconfigurable surface wave platform in the physical environment, supported by measurements conducted on the 3D-printed prototype. Furthermore, these results lay a foundation for subsequent research on different pathways and their characteristics.

Chapter 5

Distribution Pathway on the Reconfigurable Surface Wave Platform

5.1 Introduction

This chapter presents the use of a reconfigurable T-junction on the surface wave platform to divide a surface wave signal into two parts along distribution pathways. Through extensive 3D electromagnetic simulations and experiments, the effectiveness of splitting and guiding surface waves in different directions with minimal interference is demonstrated. The impact of key physical parameters of the T-junction, such as splitting depth, splitting shape, and symmetry or asymmetry, is analyzed. The aim of this chapter is to understand how these parameters affect the performance of the surface wave divider. Additionally, the feasibility of achieving varying power ratios by utilizing the reconfigurable T-junction is investigated. The chapter also examines the frequency dependence of different asymmetric T-junctions and pathways. The study of the distribution pathway sets the foundation for the development of reconfigurable architectures that facilitate simultaneous communications among multiple devices on a shared surface wave communication network.

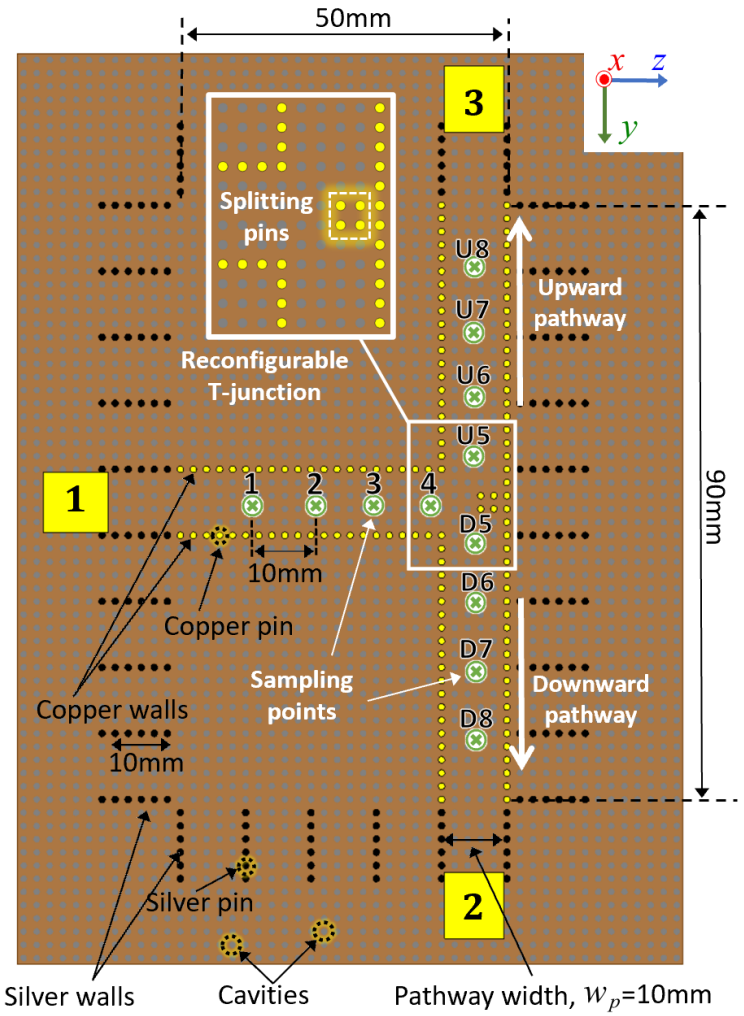

Figure 5.1: Illustration of the distribution pathway surface model with a reconfigurable T-junction where the sampling points, 1-4, U5-U8 and D5-D8, of a 10 mm interval are added along the upward and downward pathways.

5.2 Distribution Pathway Model

The surface geometry of the distribution pathway with a T-shaped junction is illustrated in Fig. 5.1, and the corresponding simulation results are presented in Fig. 5.2. In this configuration, Transducer 1 serves as the transmitter, while Transducers 2 and 3 act as the receivers positioned symmetrically at the two ends of the T-shaped distribution pathway. The surface waves, excited and guided along the straight pathway, reach the intersection point, i.e., the reconfigurable T-junction, where the splitting pins are located. At the junction, the surface waves will undergo a 90°-turn due

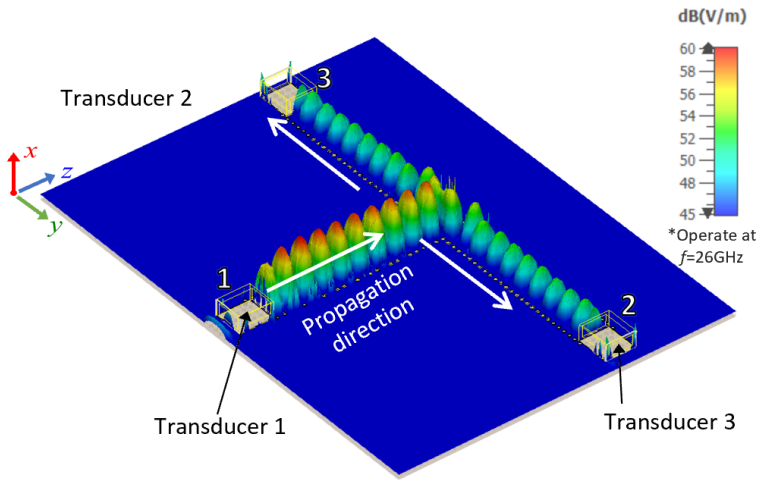

Figure 5.2: The simulation results for the distribution pathway at 26 GHz.

to the presence of the splitting pins, resulting in their division into two branches. Subsequently, the divided waves propagate towards Transducers 2 and 3 through the pathways in the $+y$ and $-y$ directions, respectively. The main focus of this chapter is to investigate how the arrangement of the splitting pins at the T-junction affects the power division. By adjusting the distribution of the pins and evaluating the S_{j1} parameter, where $j = 2$ or 3, the optimal surface wave distribution geometry can be determined.

In both simulation and measurement, E-field sampling points (indicated by green dots in Fig. 5.1) are placed along the centerline of the surface wave pathway from 1-4 to U/D5-8 in the distribution pathways. These sampling points are spaced at intervals of 10 mm. Points 1 and U/D8 are located more than 20 mm away from the transducers to minimize the influence of reflected waves. Moreover, longer waveguides are used as transducers in the experiment to reduce the impact of wave reflections occurring at the adapters connected to the end of the waveguides. Notably, points 4 and U/D5 at the T-junction are of particular interest as they are used to calculate and evaluate the insertion loss, which represents the loss incurred when the surface waves pass through the junction and are subsequently divided into the $+y$ (Transducer 2) and $-y$-directions (Transducer 3).

The measurement setup of the 3D-printed surface prototype, connected to a

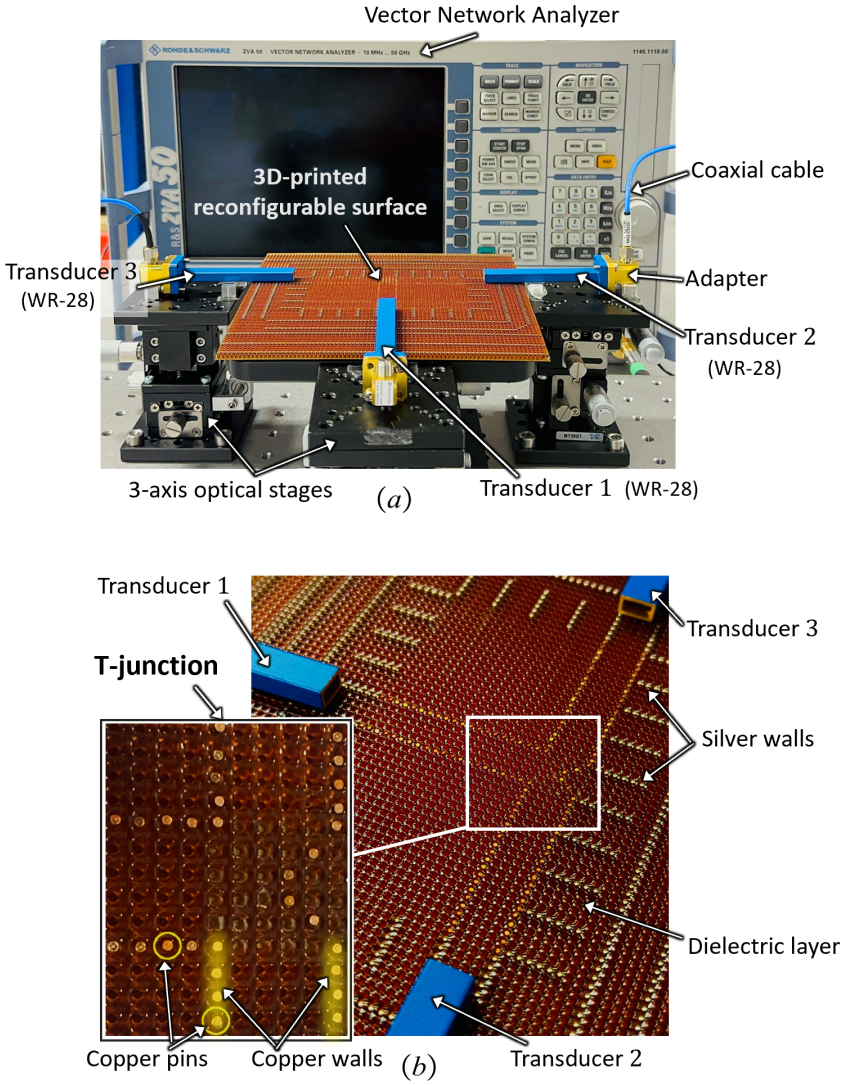

Figure 5.3: (a) The measurement setup of a 3D-printed surface prototype connected to a vector network analyzer and (b) the configuration of the reconfigurable T-junction.

Table 5.1: Parameters in the measurements and simulations for distribution pathways

Surface Parameters	Value
radius of cavity/metal pin, r	0.5 mm
center-to-center separation between cavities, w_s	2 mm
relative permittivity of the dielectric layer, ε_r	2.8
effective permittivity of the dielectric layer, $\varepsilon_r^{\text{eff}}$	2.4
thickness of the dielectric layer, h	2 mm
pathway width, w_c	10 mm
dielectric loss tangent, $\tan\delta$	0.0155 at 26 GHz
surface impedance, Z_s	$j240\,\Omega$ at 26 GHz
depth of splitting pins, d_e	0, 2, 4, 6 mm

VNA via coaxial cables for S-parameter measurements, is illustrated in Fig. 5.3. This surface prototype is also identical to the one utilized in Section 4.2. However, the experimental configuration for the distribution pathway differs. It can be observed that three WR-28 rectangular waveguides with a thickness of 1 mm are utilized as transducers to evaluate the surface wave distribution performance, instead of the two used previously. When testing the information from the third transducer, it is achieved by disconnecting the coaxial cable from another transducer and connecting it to the third transducer. It is important to note that calibration of the VNA is necessary after completing this process. Similarly, these three transducers are mounted on 3-axis optical linear stages, enabling precise adjustments to their relative positions. Copper pins with the same radius as the circular cavities are incorporated within the customized surface to showcase its reconfigurability. The specific parameter values are provided in Table 5.1.

5.3 Measurement and Simulation Results

5.3.1 Symmetric Pathways and Splitting Losses

The effectiveness of T-junctions in distributing surface waves is investigated using a symmetric distribution pathway, as shown in Fig. 5.4. Splitting pins are introduced at the T-junction and evenly distributed along the centerline. The depth refers to the distance of the splitting pins extending from the bottom wall of the junction towards the $-z$-direction. It varied from 0 mm at Junction 1 to 6 mm at Junction 4, increasing in 2 mm increments between each step. Point 1, which have a normalized E-field power density of 0 dB, served as the reference point.

Based on the E-field distribution observed at Junction 1 in Fig. 5.4, it is evident that surface waves are directly reflected at the bottom wall, where no splitting pins are present. This is indicated by a value of -28.82 dB at the D/U8 point. Consequently, the majority of surface waves are reflected back towards Transducer 1, while only a small portion reaches Transducers 2 and 3. In contrast, at Junctions 2-4, where splitting pins are introduced, the corresponding values at D/U8 are -8.64 dB, -8.21 dB, and -12.74 dB, respectively. This significant increase in sur-

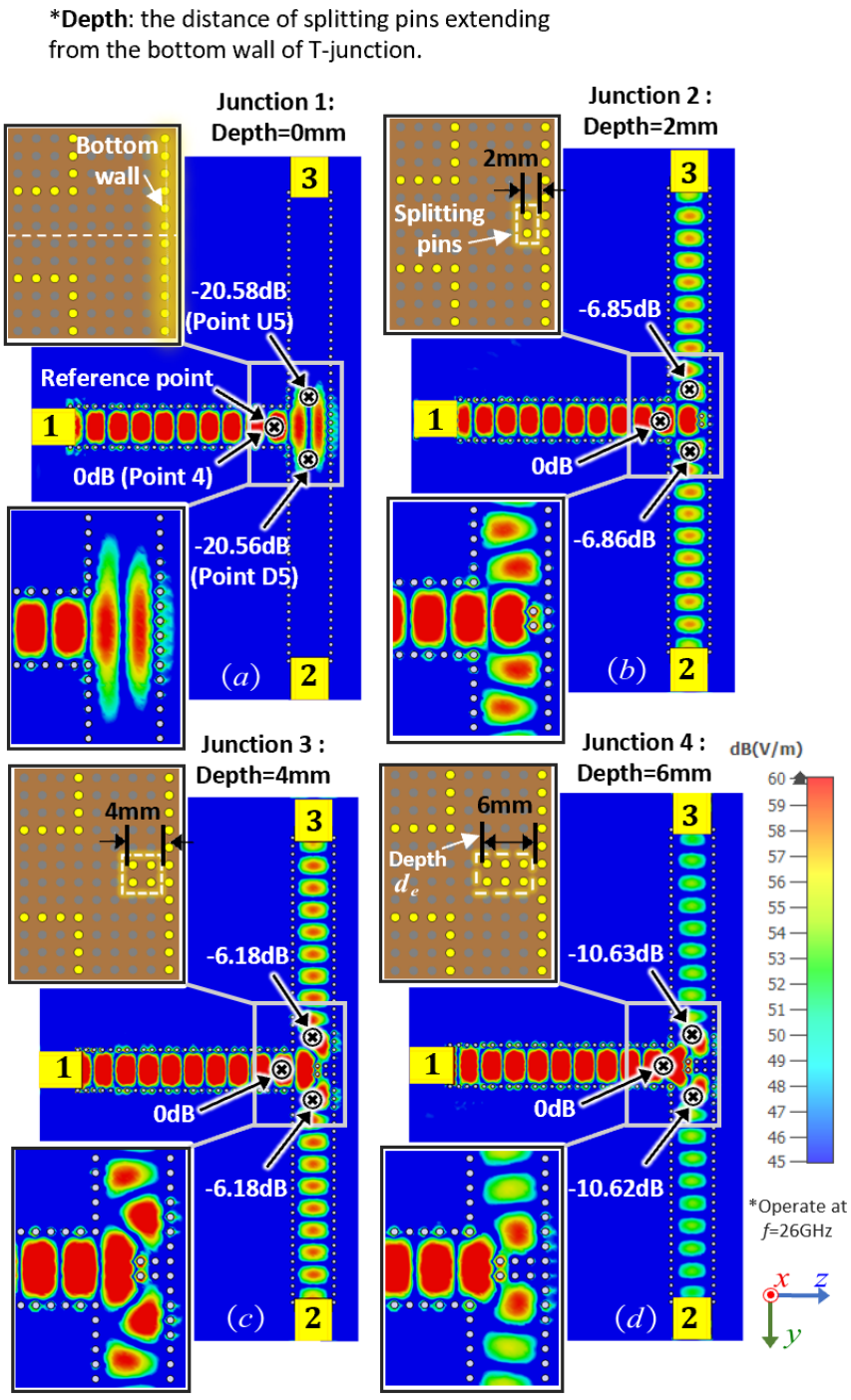

Figure 5.4: Illustration of the distribution pathway performances of a symmetric geometry in (a) Junction 1 without splitting pins, i.e., depth $d_e = 0$ mm, and Junctions 2-4 configured with the splitting pins with d_e of (b) 2 mm, (c) 4 mm, and (d) 6 mm at 26 GHz.

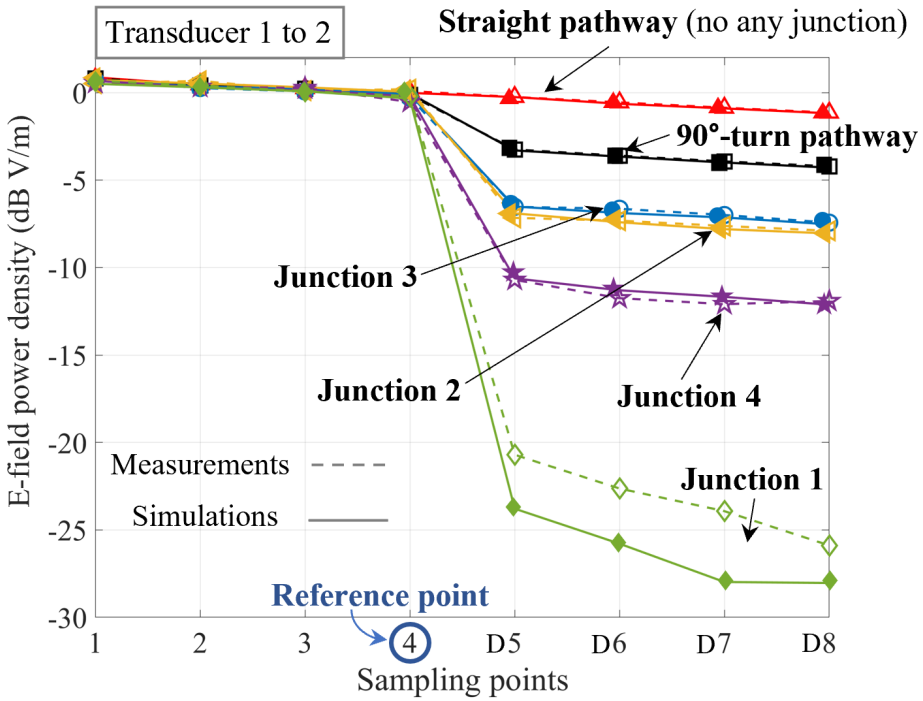

Figure 5.5: The comparison of the E-field power attenuation at each sampling point in 1-D8 from Transducer 1 to 2 in measurement and simulation results at 26 GHz.

face waves received by Transducers 2 and 3 compared to Junction 1 suggests that the splitting pins facilitate distribution pathways, reducing surface wave reflection at the junctions and enhancing the signals received by the transducers. Additionally, it is worth noting that the E-field power at D8 and U8 remains consistent across the junctions, indicating a uniform distribution of surface waves along both the $+y$- and $-y$-directed pathways in the symmetric geometry.

Fig. 5.5 illustrates the normalized values of the E-field power density in dB at sampling points 1-D8 along the distributed pathway from Transducer 1 to 2 at a frequency of 26 GHz. The performance of Junctions 1-4 is studied using two reference models. The first model represents a straight pathway without any junction, resulting in a path loss of 0.28 dB/10mm. In contrast, the second model simulates an L-shaped 90°-turn pathway, with a junction insertion loss of 3.11 dB. It is worth noting that the path loss of 0.28 dB/10mm is primarily attributed to the dielectric loss tangent of the resin used, and this can be significantly reduced by employing

Table 5.2: The E-field power variations at the T-junction

Model	Point 4[§]	Point D5	Point U5	Average Loss at the junction (dB)[‡]
	(All data are in dB)			
Straight path	0	−0.28	–	0.28
90°-turn path	0	−3.11	–	3.11
Junction 1	0	−20.56	−20.58	20.57
Junction 2	0	−6.86	−6.85	6.86
Junction 3	0	−6.18	−6.18	6.18
Junction 4	0	−10.62	−10.63	10.63

[§]In each pathway, the value at the reference point (4) is normalized to 0 dB. [‡]The average loss in dB is calculated by subtracting the average value of D5 and U5 located at the reconfigurable T-junction from the value at point 4.

low loss tangent materials such as conventional PTFE ($\tan\delta = 0.00005$ at 26 GHz) [116], which exhibits a path loss of $0.0078, \mathrm{dB}/10\mathrm{mm}$.

Analyzing the results, it is evident that an E-field power reduction occurs between the sampling points 4-D5 in all T-junction models, representing the insertion loss at the T-junction. The attenuation between sampling points follows a linear path loss rate similar to that of the straight pathway. Furthermore, the agreement between the measurement and simulation results across the models validates the accuracy of the measurements, except for the higher measured S_{21} value in Junction 1 compared to the simulation results. This discrepancy may be attributed to reflections in the physical environment, resulting in the reception of space waves by Transducer 2, an effect that is not accounted for in the simulation where the boundary condition assumes an open space without reflections. Similar observations are recorded for points 1-U8 along the pathway from Transducer 1 to 3.

Table 5.2 presents the measured values at points 4, D5, and U5 at the T-junction, along with the insertion loss of each model. The symmetric geometry ensures that the values at D5 and U5 are nearly identical, and the insertion losses are calculated by subtracting the average of D5 and U5 from point 4. In Junction 1, a significant insertion loss of 20.57 dB is observed, indicating that the model without splitting pins is unable to efficiently distribute the surface waves. Junctions 2 and 3 exhibit insertion losses of 6.86 dB and 6.18 dB, respectively. Considering the 3.11 dB loss caused by the 90° turn, both Junctions 2 and 3 perform reasonably well

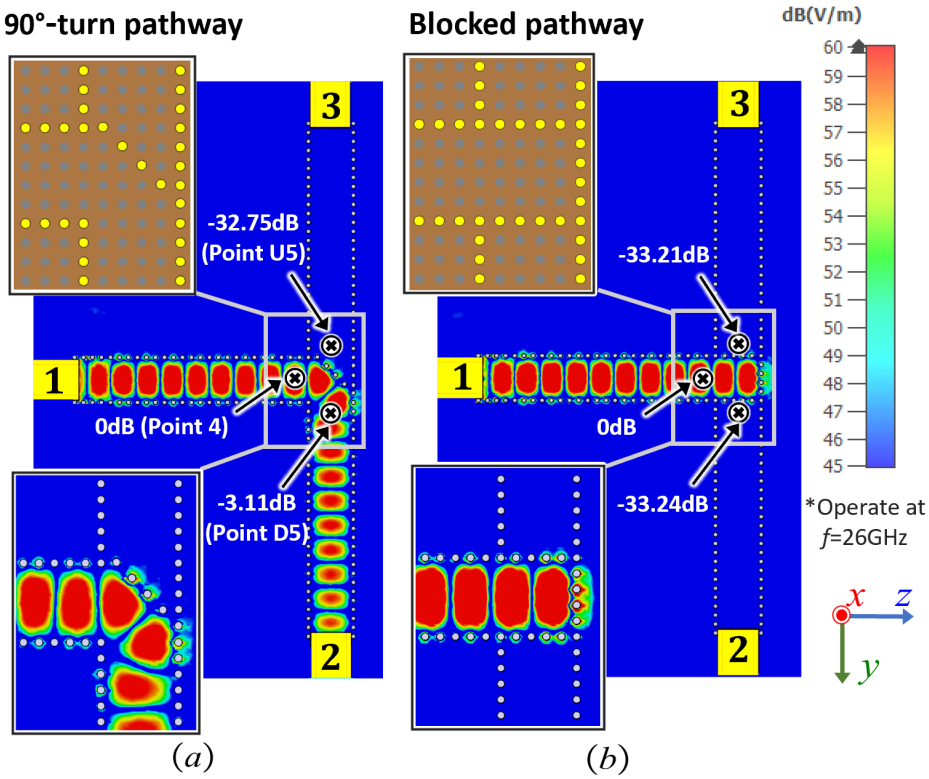

Figure 5.6: The E-field contour of (a) a 90°-turn pathway and (b) a blocked pathway after the metal pins at the T-junction, operating at 26 GHz.

as 3-dB power dividers, while Junction 4 may not be the optimal choice. Furthermore, in Junction 3, the splitting pins with a depth of 4 mm demonstrate the least insertion loss, indicating that deeper splitting pins in Junction 3 slightly outperform the smaller ones in Junction 2. This can be attributed to the deeper splitting pins guiding the surface waves along a slightly longer path, reducing reflections on the bottom wall. The relatively weaker distribution performance of Junction 4 can be attributed to the excessively long splitting pins, which further narrow the exit width at the T-junction, resulting in a certain degree of mismatch. Therefore, achieving better surface wave distribution requires an appropriate arrangement of splitting pins. Additionally, the optimization process can be further enhanced by considering the specific surface geometry associated with the application scenarios.

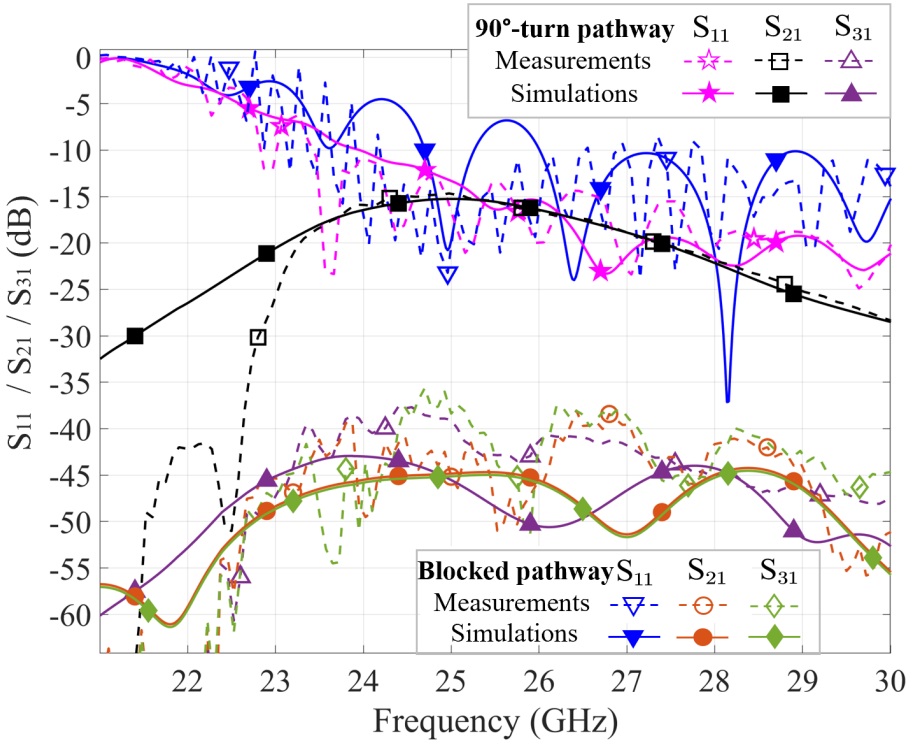

Figure 5.7: The $S_{11}/S_{21}/S_{31}$ (dB) results for a 90°-turn pathway and a blocked pathway in the measurements and simulations.

5.3.2 Flexible Open and blocked pathways

Fig. 5.6 displays simulation results of an L-shaped 90°-turn pathway as mentioned in Section 4.3.2.1 and a blocked pathway in the same surface at a frequency of 26 GHz for reference. By introducing splitting pins arranged at 45° at the T-junction, the 90°-turn pathway exclusively guides surface waves from Transducer 1 to 2, while blocking the wave propagation towards Transducer 3. The results reveal a significant difference of approximately 29.6 dB between Transducers 2 and 3, with a value of −3.11 dB at the sampling point D5 and −32.75 dB at U5. On the other hand, the blocked pathway completely impedes the surface wave propagation towards both transducers.

The $S_{11}/S_{21}/S_{31}$ curves presented in Fig. 5.7 demonstrate that the S_{31} value in the 90°-turn pathway is approximately −45 dB, comparable to the S_{21} and S_{31} values in the blocked pathway model, with a difference of nearly 30 dB from the

S_{21} value in the 90°-turn pathway. Additionally, the S_{11} value in the blocked pathway slightly exceeds that in the 90°-turn pathway due to the presence of reflections in the blocked pathway. Moreover, both the experimental and simulation results are consistent. These findings illustrate that the surface pathway design effectively guides and isolates surface waves, enabling flexible control over their propagation and mitigating mutual interference.

5.3.3 Shape of T-Junction

Further investigations were conducted to assess the effects of different shapes in the arrangement of splitting pins within the T-junction. The reference model, Configuration 1, features symmetrically located splitting pins on the centerline, with a splitting depth of 4 mm, which was found to yield the lowest insertion loss in Section 5.3.1. By gradually increasing the width of the base of the T-junction, Configurations 2-4 were obtained, as illustrated in Fig. 5.8(a). The edges formed by joining the pins, along with the bottom wall, can be approximated as isosceles triangles with apex angles (θ) of approximately 60°, 90°, 120°, and 150°, respectively.

Fig. 5.8(b) presents the measured and simulated S_{21} values across the frequency range of 22 to 30 GHz for different configurations, exhibiting negligible differences of approximately 0.1 dB. The results demonstrate that altering the apex angles does not significantly impact the received surface wave signal at Transducers 2 and 3, while the splitting depth of the T-junction has a much more pronounced effect on the insertion loss. This indicates that the shape of the T-junction can be simplified by employing Configuration 1 to achieve a low insertion loss for the distribution of surface waves, provided that the pins maintain an appropriate depth, such as 4 mm.

Furthermore, the measured and simulated S_{21} results generally exhibit good agreement. However, the experimental S_{21} values are slightly lower than those obtained from the simulations below approximately 23.5 GHz. This discrepancy may be attributed to the cutoff frequency of the coaxial-to-waveguide adapters used in the measurements [115], which is not accounted for in the simulations where the waveguide ports are directly connected to the transducers.

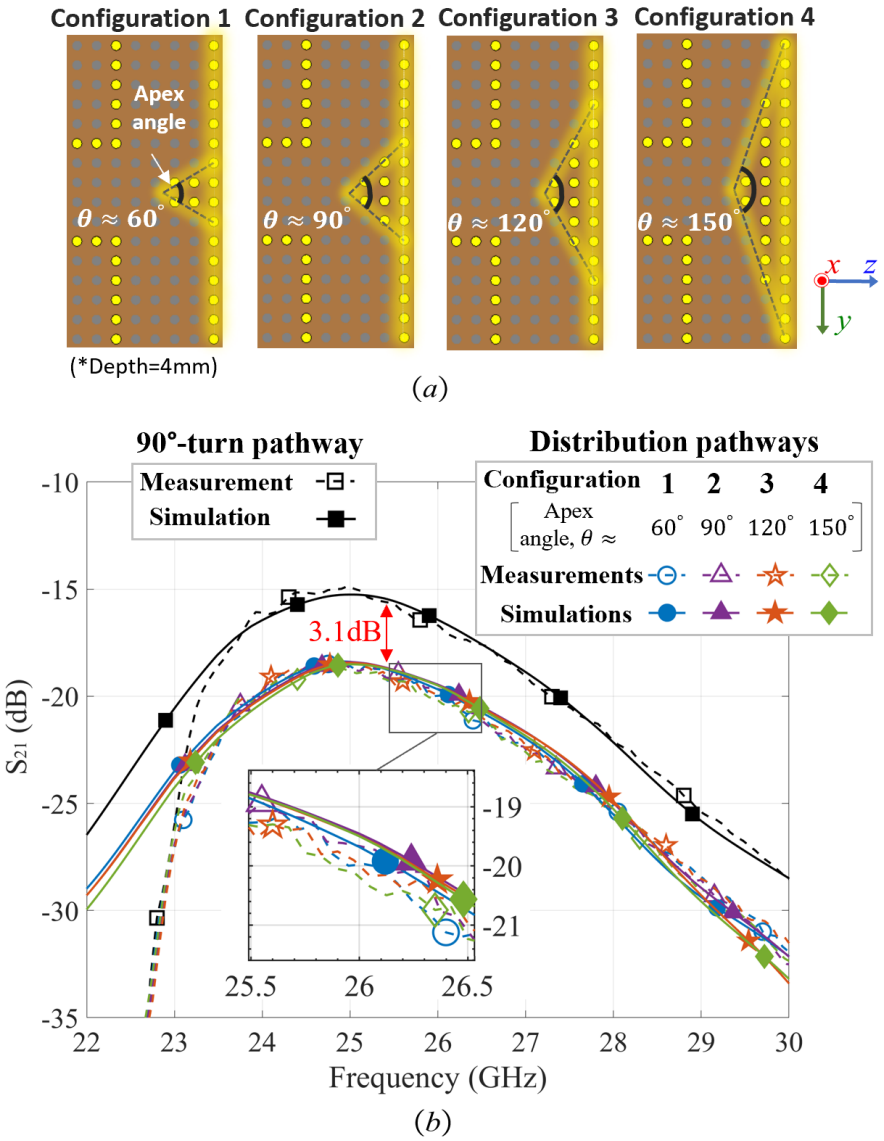

Figure 5.8: (a) The different symmetric configurations (Configurations 1-4) of splitting pins with an apex angle of around 60°, 90°, 120°, and 150°, respectively, and (b) their corresponding S_{21} (dB) results in the measurements and simulations compared with those in the 90°-turn pathway.

Additionally, there is a promising design approach for distributing and directing surface waves. This involves laying small-sized units, electromagnetic structures, microstructures, or conductive structures on the surface to adjust the paths and distribution of surface currents. By modifying the surface current, a new electromagnetic field is generated, interacting with the surrounding medium and resulting in the generation and propagation of surface waves. This design allows for the customization of surface wave guidance and control by adjusting current intensity, direction, and distribution density. To substantiate the potential of this study, Appendices A.4 provides a series of derived formulas for the surface equivalent transmission line. The conceptual framework of this approach is similar to deploying RIS on the surface, aiming to directly alter the characteristics of surface waves on-chip rather than solely relying on changes within the medium. Mr. Hadumanro Malau from our research group is actively investigating this aspect as part of his doctoral research under the guidance of Prof. Kit Wong and Prof. Kenneth Tong. The current state of research in this area is outlined in Subsection 6.2.1.

5.3.4 Asymmetric Junctions

Fig. 5.9 illustrates the geometries of Asymmetric Junctions 1-3, which are obtained by gradually shifting the splitting pins on the centerline towards the $-y$-direction in 2 mm increments, up to 6 mm, resulting in an asymmetric T-junction. Three sampling points, 4, D5, and U5, are selected at the entrance and exit ends of the T-junction in three directions. Point 4, with a normalized value of 0 dB, is taken as the reference point, as listed in Table 5.3.

In the symmetric junction, the values at D5 and U5 are -6.18 dB, with a ratio of 1:1. Conversely, in asymmetric junction 1, the value at point D5 is -5.84 dB, while that at point U5 is -7.13 dB, resulting in a ratio of E-field strengths of approximately 1.3:1. For asymmetric junction 2, the difference in the E-field power ratio increases to 4:1, and further changes to 5.1:1 in asymmetric junction 3. These results highlight the variation in power distribution of surface waves at the T-junction when the splitting pins deviate from the centerline, with a greater proportion of surface waves directed towards the wider side of the T-junction. As the pins move

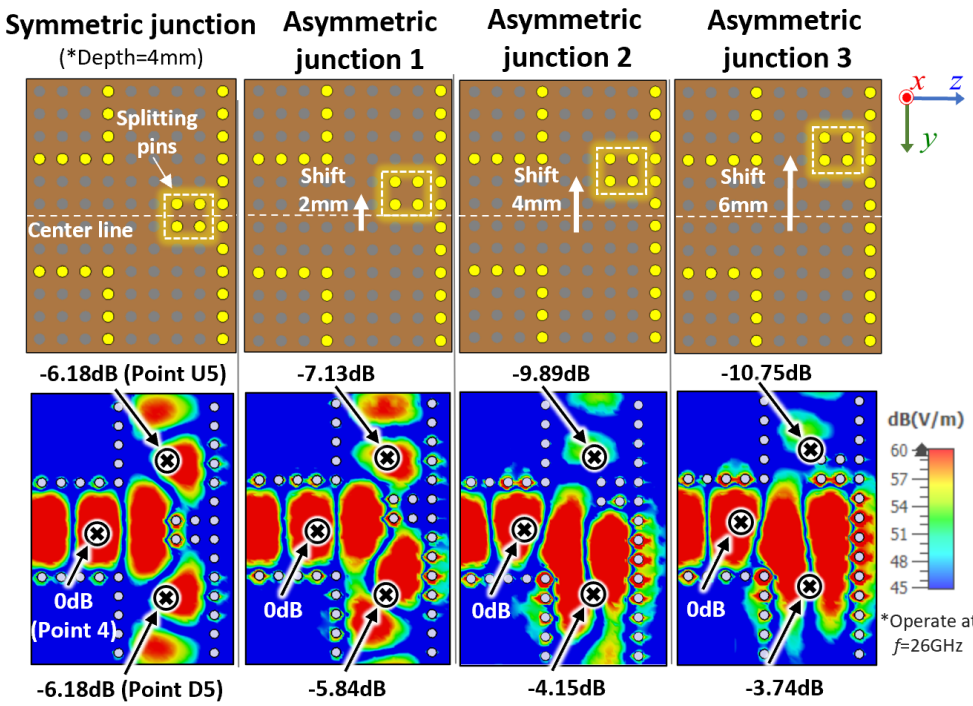

Figure 5.9: The geometry of symmetric junction and asymmetric junctions 1, 2, 3 with the splitting pins shifted from 2 mm to 6 mm in the $-y$-direction and their corresponding E-field at sample point 4, D5, U5 in three directions of the T-junction at 26 GHz.

further away from the centerline, a complete blockage of the pathway eventually occurs. Overall, these findings demonstrate the flexibility of adjusting the position of the splitting pins to control the power distribution of surface waves in different pathways.

5.3.5 Asymmetric Pathways and Frequency Selectivity

Fig. 5.10 illustrates an example of asymmetric pathways to demonstrate the frequency selectivity of the pathway. The pathway width w_c at the T-junction entrance, connecting to Transducer 1, is fixed at 10 mm, while the $+y$- and $-y$-directed pathway widths are set at 16 mm and 6 mm, respectively. The splitting pins in the T-junction are asymmetrically configured to control the power distribution. The simulation results indicate that at $f = 25.5$ GHz, S_{21} is -34.17 dB, while S_{31} is -14.82 dB, resulting in an approximate 20 dB difference between Transducers 2

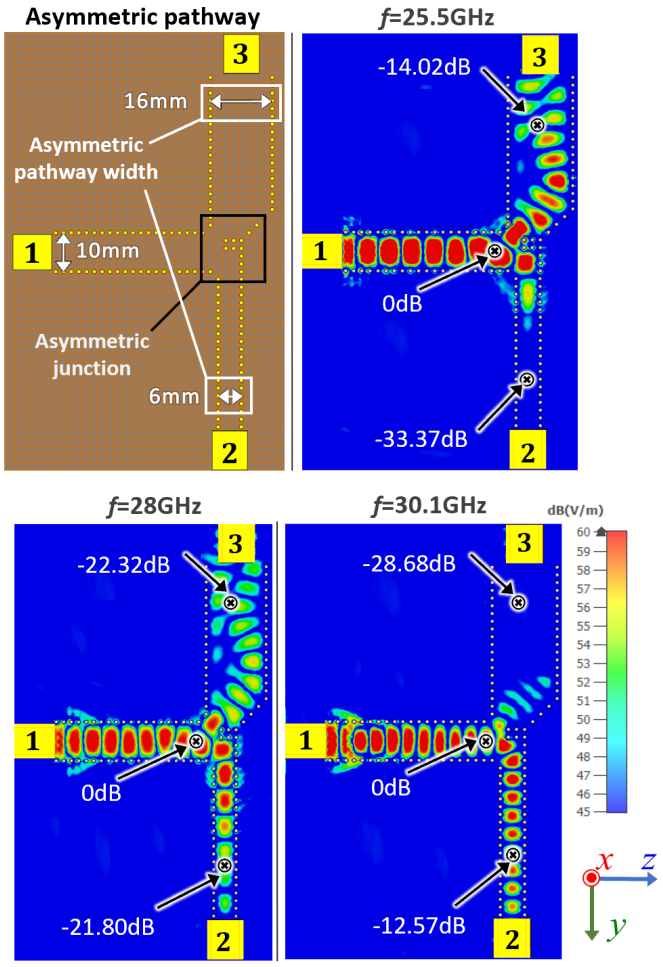

Figure 5.10: An asymmetric surface geometry with asymmetric widths of 16 mm and 6 mm at upward and downward pathways and its E-field power in simulation results at 25.5 GHz, 28 GHz and −30.1 GHz.

and 3. At 28 GHz, S_{21} is −22.60 dB, and S_{31} is −23.52 dB, approaching similar values. Furthermore, at 30.1 GHz, S_{21} is −13.37 dB, and S_{31} is −29.68 dB, resulting in a 16 dB difference between the two ports. These results demonstrate that the asymmetric pathway can effectively separate surface waves operating at different frequency bands.

Fig. 5.11 displays the S_{21} and S_{31} values of the model obtained from both measurements and simulations. For the 16 mm pathway, the operating frequency is 25.5 GHz, with a 3-dB half-power bandwidth ranging from 24.1 GHz to 26.9 GHz. On the other hand, the 6 mm pathway operates at 30.1 GHz, with a 3-dB half-power

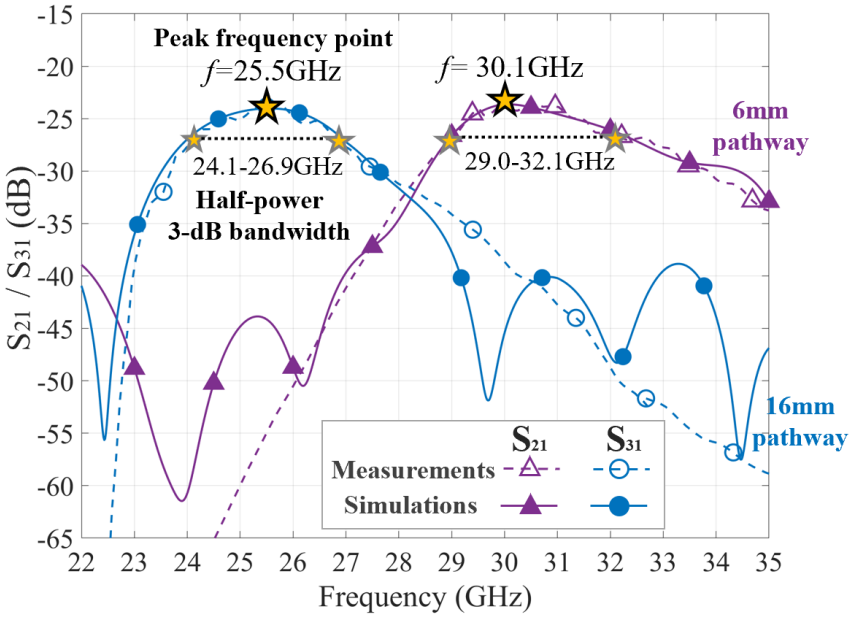

Figure 5.11: The S_{21}/S_{31} (dB) results for an asymmetric surface geometry in the measurements and simulations.

Table 5.3: The E-field power variations in the symmetric/asymmetric junctions

Junction	Normalized E-field power (dB)			Difference (dB)	Power ratio
	Point 4	D5	U5	D5 – U5	D5:U5
Sym.	0	−6.18	−6.18	0	1 : 1
Asym. 1	0	−5.84	−7.13	1.29	1.3 : 1
Asym. 2	0	−4.15	−9.89	5.74	4 : 1
Asym. 3	0	−3.74	−10.75	7.01	5.1 : 1

bandwidth spanning from 29.0 GHz to 32.1 GHz. At the peak frequency point of each separated pathway, the isolation is approximately 18 dB. Therefore, the asymmetric pathways have the potential to achieve frequency-based signal distribution by controlling the splitting pins and pathway width simultaneously, allowing surface waves at different frequency bands to be delivered to different transducers. These results demonstrate the feasibility of flexible control over surface waves in frequency bands. However, further comprehensive studies are required for more precise frequency division and characterization.

5.4 Conclusions

In conclusion, this chapter introduces a reconfigurable T-junction as a means of flexible control over distribution pathway in the millimeter-wave frequency band. By utilizing fluid metal or metal pins as splitting pins at the junction, the incoming wave can be divided and directed along the $+y$ and $-y$ pathways towards transducers 2 and 3, respectively. In a symmetric splitting pins structure, the field strengths in the two distribution pathways are totally equal. The selection of an appropriate splitting depth is instrumental in minimizing insertion losses incurred during the distribution process. Furthermore, this chapter reveals that the shape of the T-junction has minimal impact on the distributed signals. By adjusting the degree of asymmetry, the asymmetric arrangement of splitting pins and pathway widths effectively redistributes the power of surface waves along different propagation directions, and further regulate the half-power bandwidth in different distribution pathways. Consequently, these research findings demonstrate the remarkable capability of the reconfigurable surface wave platform in flexibly managing and allocating the propagation direction, power, and optimal operating frequency of surface waves. This underscores the significant potential of this platform in various SWC applications.

Chapter 6

Conclusions and Future Works

6.1 Summary of the Thesis

In conclusion, this thesis has successfully developed a novel reconfigurable surface wave platform and thoroughly investigated its propagation characteristics and the analysis of different surface wave pathways as shown in Fig. 6.1. The proposed re-

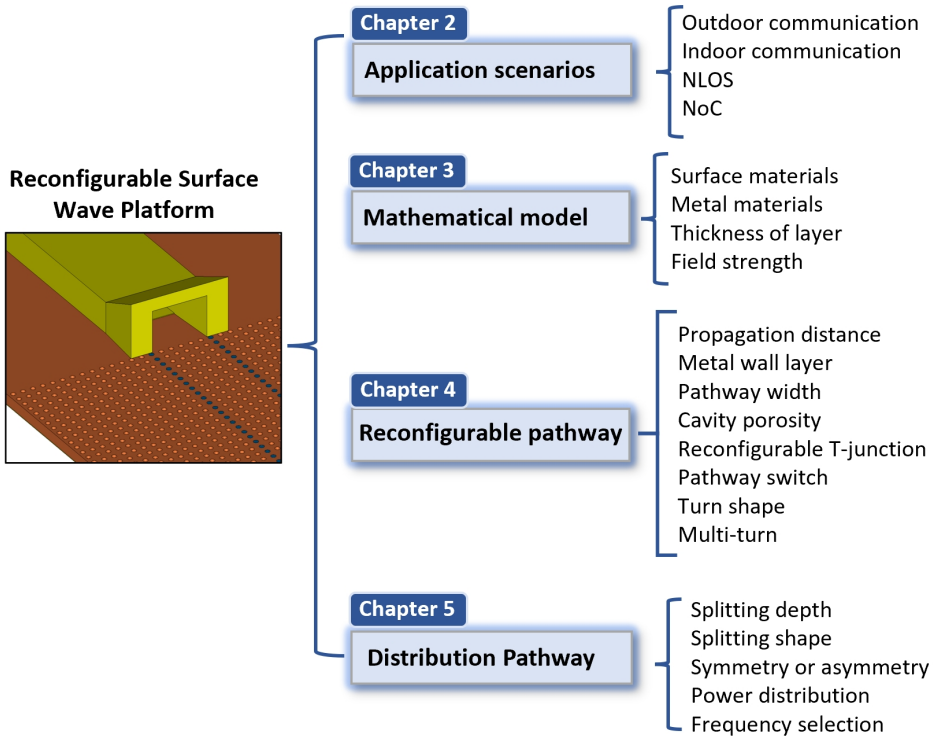

Figure 6.1: The summarized investigation structure of this thesis.

configurable surface wave platform, utilizing a porous architecture and fluid metal filling, has demonstrated dynamic propagation pathways for surface wave communication. The mathematical analysis conducted in this study has provided theoretical models into the impact of surface materials, metal materials, thickness, cavity porosity, and other parameters on the propagation performance of surface waves, leading to effective optimization of the reconfigurable surface geometry.

Experimental measurements and full electromagnetic simulations of the three-dimensional printed reconfigurable surface wave platform were conducted, providing comprehensive validation for the proposed technology. The examination of pathway parameters, including guided pathways and turning pathways, further enhanced the understanding of the platform's capabilities. The simulation results were successfully verified through real experiments, confirming the accuracy and reliability of the mathematical analysis.

The results obtained from the experiments and simulations have demonstrated the feasibility of the proposed reconfigurable platform in terms of its wide bandwidth, low path loss, and controllable communication capabilities. By optimizing the studied parameters, such as surface wave pathway configuration dynamically, power distribution, and frequency selection, the platform has exhibited higher flexibility and adaptability. These research findings contribute to the advancement and application of multiple devices accessing a shared surface wave communication network simultaneously.

Future research directions can focus on further optimizing the reconfigurable platform and exploring its applications in various practical scenarios, such as wireless sensor networks, IoT, NoC in 5G/6G communication systems. Additionally, investigations into the integration of advanced signal processing techniques and intelligent algorithms can further enhance the performance and capabilities of the reconfigurable surface wave platform.

Overall, this thesis has positive laid a foundation for the development and implementation of reconfigurable surface wave transmission technique by introducing a reconfigurable platform and providing a comprehensive analysis of its propaga-

tion characteristics., opening up new possibilities for efficient and adaptable wireless communication systems, particularly in complex channel environments with a massive number of connected devices. The research findings contribute to the understanding of surface wave mathematical modeling, experimental validation, and optimization techniques and advancements in surface wave communication.

6.2 Future Works

6.2.1 Challenges and Strategies for the Future

In the future research and application scenarios of surface waves, there still exist several limitations and challenges. The following will outline and discuss the potential issues that may arise or be faced by surface waves from the following perspectives.

Physical Deployment Issue

The practical application scenarios of surface waves require further consideration. For instance, the choice of operating frequency range is crucial. If operating in the low-frequency range (centimeter waves), such as 3.5 GHz in frequency range 1 (FR1) of 5G, a surface wave platform necessitates a large surface area for wave propagation. The extensive use of dielectric and metal materials over a wide range could lead to a substantial increase in costs. Alternatively, selecting a higher frequency range (millimeter waves), like the 26 GHz discussed in FR2 of 5G in this thesis, introduces increased path losses due to higher tangent losses with frequency, as indicated in Equation (3.13). Additionally, inherent attenuation of surface waves would also rise.

In such circumstances, it may be necessary to choose an appropriate frequency range for different application scenarios. Addressing existing Sub-6GHz frequency bands in outdoor 5G scenarios, designing building walls from the outset to facilitate surface wave propagation can mitigate additional costs associated with secondary construction. This process may involve the use of composite materials, such as designing the external walls of buildings with glass as a dielectric layer, embedding metal ground and pins within the glass to form a structure conducive to surface

wave propagation. On the other hand, for small-scale applications like NoC, higher frequency bands can be considered as carriers. Regardless of the scenario, the use of low-loss dielectric boards is crucial to minimize energy loss during electromagnetic wave transmission on the surface.

Wave transition Issue:
The transition from surface waves to space waves can be achieved through the use of metal patches on the surface, as discussed in subsection 2.6. However, in practical scenarios, as illustrated in Fig. 2.6, it is essential to consider the user's position in different directions for beamforming propagation. Simultaneously transforming surface waves into space waves on a surface and shaping space waves into beamforms are two complex and challenging problems.

Our current approaches do not consider the placement of a large number of antenna elements on the surface, akin to beamforming in massive MIMO, as it is impractical and cost-prohibitive. Therefore, the primary focus now is on leveraging mature RIS technology for directional control of waves. This process necessitates a reevaluation of how RIS are configured on the surface, with two research directions currently being pursued. Firstly, in the horizontal direction, a layer of RIS is adhered to the surface. This entails an analysis of the equivalent circuits for both the surface and the RIS. Secondly, in the vertical direction, periodic small-sized RIS elements are arranged to adjust parameters such as amplitude and phase of surface waves. Both directions involve complex mathematical and physical modeling. Size constraints, as mentioned in the previous section, also pose a challenge. Considering the use of small-sized diodes for controlling circuit signals within the RIS, soldering these diodes onto the RIS presents a challenge. Fortunately, Mr. Hadumanro Malau, a member of our research group, is currently investigating this issue (part of his doctoral research) under the guidance of Prof. Kit Wong and Prof. Kenneth Tong. Progress has been made, and it is now possible to adjust beam directions on the surface by configuring diodes within the RIS. Positive simulation results have been obtained, and efforts are underway to advance the entire project towards experimental validation in the laboratory.

Attenuation estimation Issue

In practical application scenarios, a common occurrence is the conversion between space waves to surface waves and back to space waves. As reasoned in Chapter 3 and Appendices of this thesis, the entire process of this transformation requires deriving the electromagnetic wave expressions based on the specific space structure of the surface. The entire procedure involves multiple mathematical modeling of the surface, and the derivations are inherently complex. Consequently, estimating the electromagnetic wave attenuation from the base station to the surface and then to the user is challenging.

Our current approach involves simplifying certain aspects of the model and the problem during the derivation process. For instance, considering multiple antennas simultaneously emitting signals from the active antenna unit (AAU) in existing 5G base stations, we initially focus on modeling one channel. When the electromagnetic wave enters the surface, we assume the wave to be a uniform plane wave, facilitating the analysis of wave reflection and incidence. Diffuse waves in free space and surface waves caused by secondary reflections are not considered at this stage. Through the streamlined model, we aim to obtain a preliminary overall electromagnetic wave attenuation formula. We then assess the disparities between our idealized simplified model and the simulation environment by quantitatively analyzing the same scenario using simulation software. Any differences identified are summarized as additional parameters incorporated into our deduced formula. This part of the work is primarily conducted by Miss. Haizhe Liu (part of her doctoral research) in our research group under the guidance of Prof. Kit Wong and Prof. Kenneth Tong. The current results are in the process of being organized, and we plan to submit them for publication soon.

Communication Quality Issue

As outlined in this thesis, my doctoral research has primarily focused on whether surfaces can control surface waves and how surfaces can flexibly manipulate them. The overall perspective on existing surface wave systems is that they are still in a nascent stage. Further contemplation is required for various indoor and outdoor

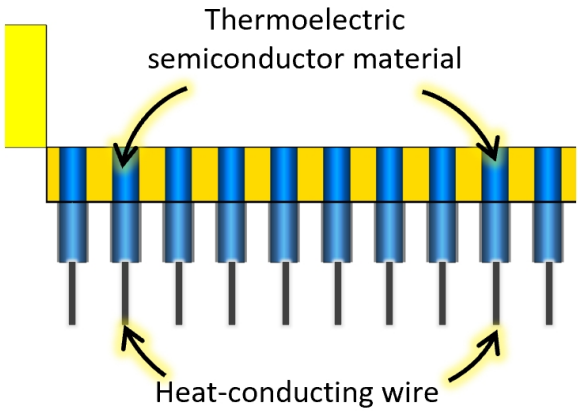

Figure 6.2: A schematic diagram depicting the substitution of a thermoelectric semiconductor material for fluid metal within cavities.

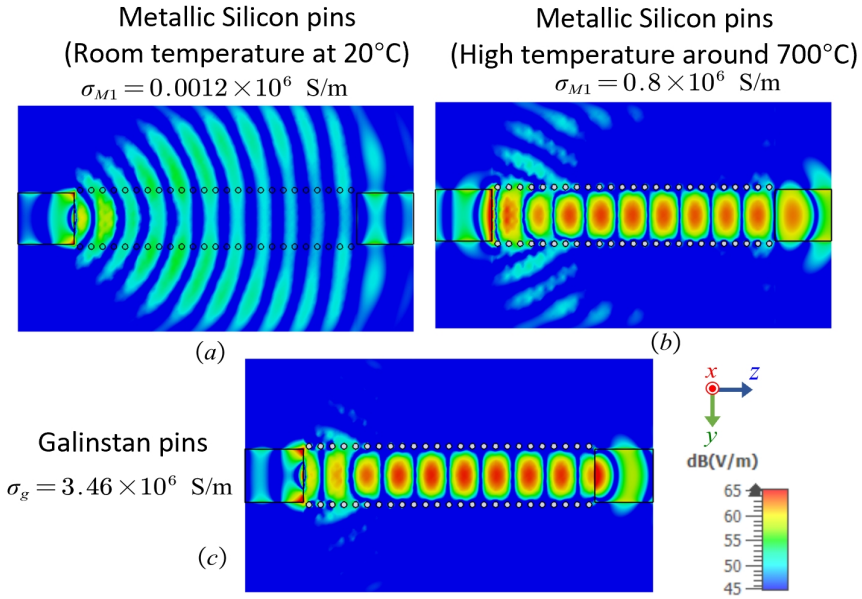

Figure 6.3: The simulation results of (a) metallic silicon pins at room temperature at 20 °C ($\sigma_{M1} = 0.0012 \times 10^6$ S/m) and (b) high temperature around 700 °C ($\sigma_{M2} = 0.8 \times 10^6$ S/m) and (c) Galinstan pins at room temperature ($\sigma_g = 3.46 \times 10^6$ S/m) at 26 GHz.

application scenarios, particularly as it pertains to ensuring communication quality.

As discussed in this thesis, while surface waves propagate stably and reliably on surfaces under normal circumstances, obstacles on the surface can disrupt this propagation. To overcome obstacles, flexible pathways can be designed to redirect the surface wave propagation. However, this process necessitates a thorough awareness of the entire communication environment. Accurate identification of obstacle size and range is crucial for planning logical propagation routes. Similar to challenges encountered in many communication channels, this process requires an integrated approach combining sensing and adaptive propagation algorithms to yield effective results. Likewise, this poses a highly challenging and long-term problem. At this stage, research efforts are focused on refining the theoretical aspects of surface waves and ensuring the reliability of surface wave communication in laboratory settings. By incrementally addressing current challenges, we can progressively pave the way for more extended considerations in the future.

6.2.2 Potential Research Direction

The programmable digital design of reconfigurable surfaces based on fluid metals has been thoroughly detailed in this thesis. Building upon the summarized surface wave characteristics derived from this, there is an opportunity to further explore alternative materials for direct digital implementation, bypassing the pump introduced in this thesis.

In future research, the author considers a promising direction for exploration, envisioning the utilization of thermoelectric semiconductor materials as a replacement for the currently studied fluid metals to achieve the guidance of surface waves on a reconfigurable surface wave platform as well. The potential advantage of thermoelectric semiconductor materials lies in their significant increase in electrical conductivity with rising temperatures. As illustrated in Fig. 6.2, heat-conducting wires can be connected to the thermoelectric semiconductor pins at the bottom of the metal ground. When the entire surface is in a non-guided state, the heat-conducting wire remains inactive, and the thermoelectric semiconductor behaves like a normal semiconductor without waveguiding functionality. However, in a guided state, when

preparing to form a pathway beneath the cavity, the heat-conducting wire beneath the cavity is heated through electrical signals, causing the thermoelectric semiconductor's electrical conductivity to markedly increase, mimicking the waveguiding function of fluid metals.

A set of comparative simulation results is presented in Fig. 6.3. The novel multilayered structure of metallic Silicon Si(111) serves as the test subject, with its electrical conductivity capable of increasing by several orders of magnitude upon heating ideally [121]. Fig. 6.3 (a) and (b) simulate the metallic silicon pins at room temperature (20 °C) ($\sigma_{M1} = 0.0012 \times 10^6$,S/m) and high temperature around 700 °C ($\sigma_{M2} = 0.8 \times 10^6$,S/m), respectively. It is evident that the former exhibits weak electrical conductivity and cannot guide surface waves, while the latter demonstrates effective surface wave guidance, with results comparable to Fig. 6.3 (c), depicting Galinstan pins in the surface at room temperature ($\sigma_g = 3.46 \times 10^6$,S/m) at 26,GHz. This suggests that thermoelectric semiconductor materials have the potential to replace fluid metals as guiding materials. They can be controlled directly through electrical signals transmitted by the underlying heat-conducting wire, bringing digital control of the surface one step closer. However, this concept is highly idealized, and delving deeper into this direction requires addressing several challenges.

The exploration of thermoelectric semiconductor material: This involves researching the construction of a novel thermoelectric semiconductor material, with the stability of such material requiring further evaluation. The challenge lies in the implementation of this material in connection with heat-conducting wires, especially in smaller dimensions.

Excessive heating temperatures: The current requirement for excessively high temperatures to alter the conductivity of thermoelectric semiconductor materials is impractical for real-world applications. Exploring temperature-sensitive materials on a small scale becomes essential, necessitating research in the fields of chemistry and new materials.

Connection status detection and feedback: Building upon the solutions to the

aforementioned challenges, the next concern is ensuring the stability of the designed system. This involves employing sensors or other components to detect the connection status of each pin and providing timely feedback to the control system. This facilitates closed-loop control and real-time adjustments.

Through research in this direction, the potential for dynamic control of surfaces can be expanded, enabling more flexible and programmable connectivity functions across various application domains. Furthermore, this is expected to catalyze the future development of reconfigurable surfaces in the realm of SWC.

6.2.3 Digital Control

In the future work of digital control of surface waves, a key task is to enhance the design of the digital control surface wave platform. This entails developing algorithms to control and select surface wave paths, converting real path information into digital data, and dynamically generating paths using programmable pumps. This work encompasses several aspects as follows

Path encoding algorithms: Researching methods to encode actual path information into digital format. This involves modeling and analyzing surface wave propagation characteristics to determine path parameters and constraints. Algorithms can then be devised to generate digital path encoding schemes for implementation and control within the digital control surface wave platform.

Path selection algorithms: Designing algorithms to select suitable paths that meet specific communication requirements. This entails considering mutual interference and signal attenuation between paths, as well as optimizing path selection for optimal transmission performance. By analyzing communication needs and environmental conditions, intelligent path selection algorithms can be developed to achieve efficient signal transmission and communication quality.

Programmable pump design: Investigating the design and control techniques for programmable pumps to enable dynamic path generation. This includes studying appropriate materials and structures to facilitate pump controllability in different paths and directions. Designing precise control mechanisms is crucial for accurately controlling the pumps and adjusting the paths.

System integration and optimization: Considering the overall integration and optimization of the digital control surface wave platform is essential. This involves integrating sensors, control units, and communication interfaces (such as microtubes) to enable dynamic control and adjustment of surface wave paths.

By pursuing research in these specific directions, further advancements in digital control of surface waves can be made, resulting in more flexible and efficient control of surface wave paths and communication capabilities.

Appendix A

Appendices

A.1 Derivation of Surface Wave Excitation Process

This section will particularly introduce the derivation for the excitation process of surface waves and the surface impedance functions.

A.1.1 Oblique Incidence Model

Fig. A.1 illustrates a ideal model where the oblique incidence of a uniform plane wave onto the ideal multi-layer medium interface, consisting of a metal ground (Layer 1), dielectric layer (Layer 2) and air layer (Layer 3). That is the basic propagation surface for surface waves in this thesis. In this scenario, the incident, reflected, and transmitted waves deviate from propagating perpendicularly to the interface. For oblique incidence, the plane formed by the wave vector of the incident wave and the normal vector to the interface is termed the incident plane ($x-z$ plane). If the incident wave is characterized as a parallel-polarized wave, signifying that the E-field of the incident wave aligns with the incident plane. Currently, all E-field component directions parallel the incident plane, while the H-field component directions remain perpendicular to the incident plane.

Within the multi-layer structure depicted in Fig. A.1, the incident wave experiences two reflections and refractions at the interfaces $x = 0$ and $x = l$, corresponding to the boundaries between layers. The E-field $\hat{\boldsymbol{E}}$ can be decomposed into $\hat{\boldsymbol{x}}E_x$ and $\hat{\boldsymbol{x}}E_z$ components at x and z directions, respectively. The H-field $\hat{\boldsymbol{H}}$ can be written as

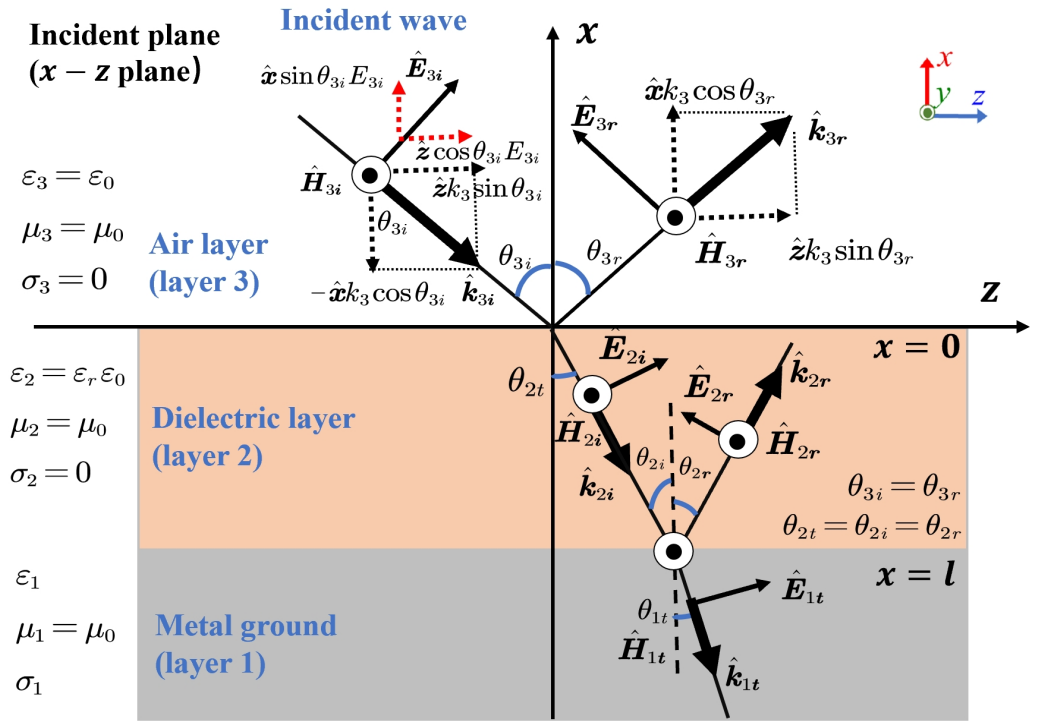

Figure A.1: The process of oblique incidence of a uniform plane wave on a multi-layered surface.

$\hat{\boldsymbol{y}}H_y$ at y direction. Therefore, in this model, there are only components $\hat{\boldsymbol{y}}H_y$, $\hat{\boldsymbol{x}}E_x$, $\hat{\boldsymbol{z}}E_z \neq 0$ are present. Here are some parameters for the different layers as follows.

Air layer (Layer 3): θ_{3i} and θ_{3r} are the incidence and reflection angle, respectively, and $\theta_{3i} = \theta_{3r}$ by boundary condition (Snell's law). The intrinsic coefficients are $\varepsilon_3 = \varepsilon_0$, $\mu_3 = \mu_0$ and $\sigma_3 = 0$.

Dielectric layer (Layer 2): θ_{2i}, θ_{2r} and θ_{2t} are the incidence, reflection and transmission angle, respectively, and $\theta_{3i} = \theta_{3r} = \theta_{3t}$. The intrinsic coefficients are $\varepsilon_2 = \varepsilon_r\varepsilon_0$, $\mu_2 = \mu_0$ and $\sigma_2 = 0$. ε_r is the relative permittivity of the dielectric layer.

Metal ground (Layer 1): θ_{1t} is the transmission angle. The intrinsic coefficients are ε_1, $\mu_2 = \mu_0$ and σ_1.

Then the waves in the air layer are analyzed by using decomposition. $\hat{\boldsymbol{k}}$ is defined as the wave vector. $\hat{\boldsymbol{k}}_{3i}$ could be decomposed with $-\hat{\boldsymbol{x}}k_3\cos\theta_{3i}$ and $\hat{\boldsymbol{z}}k\sin\theta_{3i}$. And $\hat{\boldsymbol{k}}_{3r}$ could be decomposed with $\hat{\boldsymbol{x}}k_3\cos\theta_{3r}$ and $\hat{\boldsymbol{z}}k_3\sin\theta_{3r}$. The wave number is $k_3 = w\sqrt{\mu_0\varepsilon_0}$ in air layer. $\hat{\boldsymbol{E}}_{3i}$ is the incident E-field in the air layer and could be

decomposed with $\hat{\boldsymbol{x}} \sin\theta_{3i} E_{3i}$ and $\hat{\boldsymbol{x}} \sin\theta_{3i} E_{3i}$ along $\hat{\boldsymbol{x}}$ and $\hat{\boldsymbol{z}}$ directions, respectively, and E_{3i} is regarded as the magnitude of $\hat{\boldsymbol{E}}_{3i}$. Similarly, the other layers have the same decomposition principle.

A.1.2 Vector Decomposition

In a rectangular coordinate system, the position vector is $\hat{\boldsymbol{r}} = \hat{\boldsymbol{x}}x + \hat{\boldsymbol{y}}y + \hat{\boldsymbol{z}}z$. The Incident wave wave vector is $\hat{\boldsymbol{k}}_{\boldsymbol{i}} = \hat{\boldsymbol{x}}k_{ix} + \hat{\boldsymbol{y}}k_{iy} + \hat{\boldsymbol{z}}k_{iz}$, the reflected wave wave vector is $\hat{\boldsymbol{k}}_{\boldsymbol{r}} = \hat{\boldsymbol{x}}k_{rx} + \hat{\boldsymbol{y}}k_{ry} + \hat{\boldsymbol{z}}k_{rz}$ and transmitted wave vector is $\hat{\boldsymbol{k}}_{\boldsymbol{t}} = \hat{\boldsymbol{x}}k_{tx} + \hat{\boldsymbol{y}}k_{ty} + \hat{\boldsymbol{z}}k_{tz}$.

The H-field of the incident wave is

$$\hat{\boldsymbol{H}}_{\boldsymbol{i}} = \hat{\boldsymbol{y}} H_i e^{-j\hat{\boldsymbol{k}}_{\boldsymbol{i}} \cdot \hat{\boldsymbol{r}}}, \tag{A.1}$$

Here

$$\begin{aligned} \hat{\boldsymbol{k}}_{\boldsymbol{i}} \cdot \hat{\boldsymbol{r}} &= \left(\hat{\boldsymbol{x}}k_{ix} + \hat{\boldsymbol{y}}k_{iy} + \hat{\boldsymbol{z}}k_{iz}\right) \cdot \left(\hat{\boldsymbol{x}}x + \hat{\boldsymbol{y}}y + \hat{\boldsymbol{z}}z\right) \\ &= \hat{\boldsymbol{x}}k_{ix} \cdot \hat{\boldsymbol{x}}x + \hat{\boldsymbol{y}}k_{iy} \cdot \hat{\boldsymbol{y}}y + \hat{\boldsymbol{z}}k_{iz} \cdot \hat{\boldsymbol{z}}z \\ &= k_{ix}x + k_{iy}y + k_{iz}z \ \left(\hat{\boldsymbol{x}} \cdot \hat{\boldsymbol{y}}, \hat{\boldsymbol{x}} \cdot \hat{\boldsymbol{z}}, \hat{\boldsymbol{y}} \cdot \hat{\boldsymbol{z}} = 0\right), \end{aligned} \tag{A.2}$$

Therefore

$$\hat{\boldsymbol{H}}_{\boldsymbol{i}} = \hat{\boldsymbol{y}} H_i e^{-j\left(k_{ix}x + k_{iy}y + k_{iz}z\right)} \tag{A.3}$$

Similarly, $\hat{\boldsymbol{H}}_{\boldsymbol{r}}$ and $\hat{\boldsymbol{H}}_{\boldsymbol{t}}$ can be written as

$$\hat{\boldsymbol{H}}_{\boldsymbol{r}} = \hat{\boldsymbol{y}} H_r e^{-j\left(k_{rx}x + k_{ry}y + k_{rz}z\right)} \tag{A.4}$$

And

$$\hat{\boldsymbol{H}}_{\boldsymbol{t}} = \hat{\boldsymbol{y}} H_t e^{-j\left(k_{tx}x + k_{ty}y + k_{tz}z\right)} \tag{A.5}$$

where H_i, H_r, H_t are magnitudes of $\hat{\boldsymbol{H}}_{\boldsymbol{i}}$, $\hat{\boldsymbol{H}}_{\boldsymbol{r}}$ and $\hat{\boldsymbol{H}}_{\boldsymbol{t}}$, respectively. And k_{ix}, k_{iy}, k_{iz}, k_{rx}, k_{ry}, k_{rz}, k_{tx}, k_{ty}, k_{tz} are the wave numbers in incident, reflected, transmitted wave on the x, y, z axes.

At the boundary where $x = 0$, i.e., $e^{-jkx} = e^{-jk(0)} = 1$, the tangential components of the E- and H-fields are continuous on the y and z axes. Therefore,

$$\begin{aligned} H_{i0}e^{-j\left(k_{iy}y + k_{iz}z\right)} + H_{r0}e^{-j\left(k_{ry}y + k_{rz}z\right)} &= H_{t0}e^{-j\left(k_{ty}y + k_{tz}z\right)} \\ k_{iy}y + k_{iz}z = k_{ry}y + k_{rz}z &= k_{ty}y + k_{tz}z \end{aligned} \tag{A.6}$$

And then,

$$\begin{aligned} k_{iy} = k_{ry} = k_{ty} = k_y \\ k_{iz} = k_{rz} = k_{tz} = k_z \end{aligned} \tag{A.7}$$

where H_{i0}, H_{r0}, H_{t0} are magnitudes of $\hat{\boldsymbol{H}}_{\boldsymbol{i}}$,$\hat{\boldsymbol{H}}_{\boldsymbol{r}}$ and $\hat{\boldsymbol{H}}_{\boldsymbol{t}}$ in the tangential direction at $x = 0$.

A.1.3 Electromagnetic Field Analysis in Three Layers

Decompose the E- and magnetic components along the Cartesian coordinate system, as shown above.

Air layer (Layer 3):

In incident wave:

$$\begin{aligned} \hat{\boldsymbol{E}}_{3\boldsymbol{i}} &= \left(\hat{\boldsymbol{x}}\sin\theta_{3i} + \hat{\boldsymbol{z}}\cos\theta_{3i}\right) E_{3i} e^{-j\left(k_{3ix}x + k_{3iy}y + k_{3iz}z\right)} \\ &= \left(\hat{\boldsymbol{x}}\sin\theta_{3i} + \hat{\boldsymbol{z}}\cos\theta_{3i}\right) E_{3i} e^{-jk_3(-\cos\theta_{3i}x + \sin\theta_{3i}z)} \end{aligned} \tag{A.8}$$

And

$$\hat{\boldsymbol{H}}_{3\boldsymbol{i}} = \hat{\boldsymbol{y}} \frac{1}{\eta_3} E_{3i} e^{-jk_3(-\cos\theta_{3i}x + \sin\theta_{3i}z)} \tag{A.9}$$

In reflected wave:

$$\begin{aligned} \hat{\boldsymbol{E}}_{3\boldsymbol{r}} &= (\hat{\boldsymbol{x}}\sin\theta_{3i} - \hat{\boldsymbol{z}}\cos\theta_{3i})\, E_{3r} e^{-jk_3(\cos\theta_{3i}x + \sin\theta_{3i}z)} \\ &= (\hat{\boldsymbol{x}}\sin\theta_{3i} - \hat{\boldsymbol{z}}\cos\theta_{3i})\, R_3 E_{3i} e^{-jk_3(\cos\theta_{3i}x + \sin\theta_{3i}z)} \end{aligned} \tag{A.10}$$

And,

$$\hat{\boldsymbol{H}}_{3\boldsymbol{r}} = \hat{\boldsymbol{y}} \frac{1}{\eta_3} R_3 E_{3i} e^{-jk_3(\cos\theta_{3i}x + \sin\theta_{3i}z)} \tag{A.11}$$

where $\eta_3 = \sqrt{\frac{\mu_0}{\varepsilon_0}}$ represents the wave impedance in the air layer. R_3 is the reflection coefficient in the reflection plane, and T_3 is the transmission coefficient in the transmission plane.

Dielectric layer (Layer 2):

In incident wave:

$$\begin{aligned} \hat{\boldsymbol{E}}_{2\boldsymbol{i}} &= (\hat{\boldsymbol{x}}\sin\theta_{2i} + \hat{\boldsymbol{z}}\cos\theta_{2i})\, E_{2i} e^{-jk_2[-\cos\theta_{2i}(x-l) + \sin\theta_{2i}z]} \\ &= (\hat{\boldsymbol{x}}\sin\theta_{2i} + \hat{\boldsymbol{z}}\cos\theta_{2i})\, T_3 E_{3i} e^{-jk_2[-\cos\theta_{2i}(x-l) + \sin\theta_{2i}z]} \end{aligned} \tag{A.12}$$

And,

$$\hat{\boldsymbol{H}}_{2\boldsymbol{i}} = \hat{\boldsymbol{y}} \frac{1}{\eta_2} T_3 E_{3i} e^{-jk_2[-\cos\theta_{2i}(x-l) + \sin\theta_{2i}z]} \tag{A.13}$$

In reflected wave:

$$\begin{aligned}\hat{\boldsymbol{E}}_{2\boldsymbol{r}} &= (\hat{\boldsymbol{x}}\sin\theta_{2i} - \hat{\boldsymbol{z}}\cos\theta_{2i})\, E_{2r} e^{-jk_2[\cos\theta_{2i}(x-l)+\sin\theta_{2i}z]} \\ &= (\hat{\boldsymbol{x}}\sin\theta_{2i} - \hat{\boldsymbol{z}}\cos\theta_{2i})\, R_2T_3E_{3i} e^{-jk_2[\cos\theta_{2i}(x-l)+\sin\theta_{2i}z]}\end{aligned} \tag{A.14}$$

And

$$\hat{\boldsymbol{H}}_{2\boldsymbol{r}} = \hat{\boldsymbol{y}}\frac{1}{\eta_2} R_2T_3E_{3i} e^{-jk_2[\cos\theta_{2i}(x-l)+\sin\theta_{2i}z]} \tag{A.15}$$

where $\eta_2 = \sqrt{\frac{\mu_0}{\varepsilon_2}} = \sqrt{\frac{\mu_0}{\varepsilon_r\varepsilon_0}}$ is the wave impedance in the dielectric layer. Here, the analysis primarily focuses on when the boundary conditions are satisfied between the dielectric layer and the metal layer in the $x-$direction. It is essential to examine the boundary conditions at the bottom layer interface because, in a multi-layer model, the lower layer influences the equivalent wave impedance of the upper layer.

Metal ground (Layer 1):

In transmitted wave:

$$\begin{aligned}\hat{\boldsymbol{E}}_{1t} &= (\hat{\boldsymbol{x}}\sin\theta_{1t} + \hat{\boldsymbol{z}}\cos\theta_{1t})\, E_{1t} e^{-jk_1[-\cos\theta_{1t}(x-l)+\sin\theta_{1t}z]} \\ &= (\hat{\boldsymbol{x}}\sin\theta_{1t} + \hat{\boldsymbol{z}}\cos\theta_{1t})\, T_2T_3E_{3i} e^{-jk_1[-\cos\theta_{1t}(x-l)+\sin\theta_{1t}z]}\end{aligned} \tag{A.16}$$

And,

$$\hat{\boldsymbol{H}}_{1t} = \hat{\boldsymbol{y}}\frac{1}{\eta_1} T_2T_3E_{3i} e^{-jk_1[-\cos\theta_{1t}(x-l)+\sin\theta_{1t}z]}, E_{1t} = T_2T_3E_{3i} \tag{A.17}$$

A.1.4 Boundary Condition Formula Derivation

According to the boundary conditions, the tangential component of the E- and H-field are both continuous across the interface at $x = 0$ and $x = l$.

At the interface $x = l$ between he dielectric layer and the metal ground, have

$$\begin{aligned}
&\hat{\boldsymbol{E}}_{1z} = \hat{\boldsymbol{E}}_{2z}\,; \hat{\boldsymbol{H}}_{1y} = \hat{\boldsymbol{H}}_{2y} \\
&\hat{\boldsymbol{E}}_{2z} = \hat{\boldsymbol{E}}_{2iz} + \hat{\boldsymbol{E}}_{2rz}; \hat{\boldsymbol{E}}_{1z} = \hat{\boldsymbol{E}}_{1tz} \\
&\hat{\boldsymbol{H}}_{2y} = \hat{\boldsymbol{H}}_{2iy} + \hat{\boldsymbol{H}}_{2ry}; \hat{\boldsymbol{H}}_{1y} = \hat{\boldsymbol{H}}_{1t}
\end{aligned} \tag{A.18}$$

Then,

$$\hat{\boldsymbol{E}}_{2iz} + \hat{\boldsymbol{E}}_{2rz} = \hat{\boldsymbol{E}}_{1tz} \tag{A.19}$$

And

$$\hat{\boldsymbol{H}}_{2iy} + \hat{\boldsymbol{H}}_{2ry} = \hat{\boldsymbol{H}}_{1t} \tag{A.20}$$

Combine (A.12), (A.14) and (A.16), (A.19) can be written as

$$\begin{aligned}
&-\hat{\boldsymbol{z}}\cos\theta_{2i} R_2 T_3 E_{3i} e^{-jk_2[\cos\theta_{2i}(x-l)+\sin\theta_{2i}z]} + \hat{\boldsymbol{z}}\cos\theta_{2i} T_3 E_{3i} e^{-jk_2[-\cos\theta_{2i}(x-l)+\sin\theta_{2i}z]} \\
&= \hat{\boldsymbol{z}}\cos\theta_{1t} T_2 T_3 E_{3i} e^{-jk_1[-\cos\theta_{1t}(x-l)+\sin\theta_{1t}z]}
\end{aligned} \tag{A.21}$$

where $k_2 \sin\theta_{2i} = k_1 \sin\theta_{1t}$ and $x = l\ then\ e^{-j(x-l)} = 1$. And it can be get

$$(1 - R_2)\cos\theta_{2i} = \cos\theta_{1t} T_2 \tag{A.22}$$

Combine (A.13), (A.15) and (A.17), (A.20) can be written as

$$\hat{\boldsymbol{y}}\frac{1}{\eta_2}T_3E_{3i}e^{-jk_2[-\cos\theta_{2i}(x-l)+\sin\theta_{2i}z]}+\hat{\boldsymbol{y}}\frac{1}{\eta_2}R_2T_3E_{3i}e^{-jk_2[\cos\theta_{2i}(x-l)+\sin\theta_{2i}z]} = \hat{\boldsymbol{y}}\frac{1}{\eta_1}T_2T_3E_{3i}e^{-jk_1[-\cos\theta_{1t}(x-l)+\sin\theta_{1t}z]} \tag{A.23}$$

And get

$$\frac{1}{\eta_2}(1+R_2)=\frac{1}{\eta_1}T_2 \tag{A.24}$$

Combine (A.22) and (A.24) , get

$$R_2=\frac{\eta_2\cos\theta_{2i}-\eta_1\cos\theta_{1t}}{\eta_2\cos\theta_{2i}+\eta_1\cos\theta_{1t}} \tag{A.25}$$

$$T_2=\frac{2\eta_1\cos\theta_{2i}}{\eta_2\cos\theta_{2i}+\eta_1\cos\theta_{1t}} \tag{A.26}$$

At the interface $x = 0$ between the air layer and the dielectric layer, have

$$\begin{aligned}&\hat{\boldsymbol{E}}_{3\boldsymbol{z}}=\hat{\boldsymbol{E}}_{2\boldsymbol{z}};\hat{\boldsymbol{H}}_{3\boldsymbol{y}}=\hat{\boldsymbol{H}}_{2\boldsymbol{y}}\\&\hat{\boldsymbol{E}}_{3\boldsymbol{z}}=\hat{\boldsymbol{E}}_{3\boldsymbol{iz}}+\hat{\boldsymbol{E}}_{3\boldsymbol{rz}}\,;\hat{\boldsymbol{E}}_{2\boldsymbol{z}}=\hat{\boldsymbol{E}}_{2\boldsymbol{iz}}+\hat{\boldsymbol{E}}_{2\boldsymbol{rz}}\\&\hat{\boldsymbol{H}}_{3\boldsymbol{y}}=\hat{\boldsymbol{H}}_{3\boldsymbol{iy}}+\hat{\boldsymbol{H}}_{3\boldsymbol{ry}};\hat{\boldsymbol{H}}_{2\boldsymbol{y}}=\hat{\boldsymbol{H}}_{2\boldsymbol{iy}}+\hat{\boldsymbol{H}}_{2\boldsymbol{ry}}\end{aligned} \tag{A.27}$$

Then,

$$\hat{\boldsymbol{E}}_{3\boldsymbol{iz}}+\hat{\boldsymbol{E}}_{3\boldsymbol{rz}}=\hat{\boldsymbol{E}}_{2\boldsymbol{iz}}+\hat{\boldsymbol{E}}_{2\boldsymbol{rz}} \tag{A.28}$$

And

$$\hat{\boldsymbol{H}}_{3\boldsymbol{iy}} + \hat{\boldsymbol{H}}_{3\boldsymbol{ry}} = \hat{\boldsymbol{H}}_{2\boldsymbol{iy}} + \hat{\boldsymbol{H}}_{2\boldsymbol{ry}} \tag{A.29}$$

Combine (A.8), (A.10), (A.12) and (A.14), (A.28) can be written as

$$\hat{\boldsymbol{z}}\cos\theta_{3i}E_{3i}e^{-jk_3(-\cos\theta_{3i}x+\sin\theta_{3i}z)} - \hat{\boldsymbol{z}}\cos\theta_{3i}R_3E_{3i}e^{-jk_3(\cos\theta_{3i}x+\sin\theta_{3i}z)} \tag{A.30}$$

$$= \hat{\boldsymbol{z}}\cos\theta_{2i}T_3E_{3i}e^{-jk_2[-\cos\theta_{2i}(x-l)+\sin\theta_{2i}z]} - \hat{\boldsymbol{z}}\cos\theta_{2i}R_2T_3E_{3i}e^{-jk_2[\cos\theta_{2i}(x-l)+\sin\theta_{2i}z]} \tag{A.31}$$

And

$$\cos\theta_{3i}\,(1-R_3)\,e^{-jk_3\sin\theta_{3i}z} = \cos\theta_{2i}T_3\left(e^{jk_2\cos\theta_{2i}l} - R_2e^{-jk_2\cos\theta_{2i}l}\right)e^{-jk_2\sin\theta_{2i}z} \tag{A.32}$$

Get

$$\cos\theta_{3i}\,(1-R_3) = \cos\theta_{2i}T_3\left(e^{jk_2\cos\theta_{2i}l} - R_2e^{-jk_2\cos\theta_{2i}l}\right) \tag{A.33}$$

where $k_3\sin\theta_{3i} = k_2\sin\theta_{2i}$ and $e^{-jx} = 1$.

Combine (A.9), (A.11), (A.13) and (A.15), (A.29) can be written as

$$\begin{aligned}&\hat{\boldsymbol{y}}\frac{1}{\eta_3}E_{3i}e^{-jk_3(-\cos\theta_{3i}x+\sin\theta_{3i}z)} + \hat{\boldsymbol{y}}\frac{1}{\eta_3}R_3E_{3i}e^{-jk_3(\cos\theta_{3i}x+\sin\theta_{3i}z)}\\ &= \hat{\boldsymbol{y}}\frac{1}{\eta_2}T_3E_{3i}e^{-jk_2[-\cos\theta_{2i}(x-l)+\sin\theta_{2i}z]} + \hat{\boldsymbol{y}}\frac{1}{\eta_2}R_2T_3E_{3i}e^{-jk_2[\cos\theta_{2i}(x-l)+\sin\theta_{2i}z]}\end{aligned} \tag{A.34}$$

Get

$$\frac{1}{\eta_3}(1+R_3)=\frac{1}{\eta_2}T_3\left(e^{jk_2\cos\theta_{2i}l}+R_2e^{-jk_2\cos\theta_{2i}l}\right) \tag{A.35}$$

Combine (A.33) and (A.35), get

$$\eta_3\cos\theta_{3i}\frac{1-R_3}{1+R_3}=\eta_2\cos\theta_{2i}\frac{e^{jk_2\cos\theta_{2i}il}-R_2e^{-jk_2\cos\theta_{2i}il}}{e^{jk_2\cos\theta_{2i}il}+R_2e^{-jk_2\cos\theta_{2i}il}} \tag{A.36}$$

Bring (A.25) into (A.36), get

$$\begin{aligned}
&\eta_3\cos\theta_{3i}\frac{1-R_3}{1+R_3}\\
&=\eta_2\cos\theta_{2i}\frac{(\eta_2\cos\theta_{2i}+\eta_1\cos\theta_{1t})\,e^{jk_2\cos\theta_{2i}l}-(\eta_2\cos\theta_{2i}-\eta_1\cos\theta_{1t})\,e^{-jk_2\cos\theta_{2i}l}}{(\eta_2\cos\theta_{2i}+\eta_1\cos\theta_{1t})\,e^{jk_2\cos\theta_{2i}l}+(\eta_2\cos\theta_{2i}-\eta_1\cos\theta_{1t})\,e^{-jk_2\cos\theta_{2i}l}}\\
&=\eta_2\cos\theta_{2i}\frac{\eta_2\cos\theta_{2i}\left(e^{jk_2\cos\theta_{2i}l}-e^{-jk_2\cos\theta_{2i}l}\right)+\eta_1\cos\theta_{1t}\left(e^{jk_2\cos\theta_{2i}l}+e^{-jk_2\cos\theta_{2i}l}\right)}{\eta_2\cos\theta_{2i}\left(e^{jk_2\cos\theta_{2i}l}+e^{-jk_2\cos\theta_{2i}l}\right)+\eta_1\cos\theta_{1t}\left(e^{jk_2\cos\theta_{2i}l}-e^{-jk_2\cos\theta_{2i}l}\right)}\\
&=\eta_2\cos\theta_{2i}\frac{\eta_2\cos\theta_{2i}j\sin(k_2\cos\theta_{2i}l)+\eta_1\cos\theta_{1t}\cos(k_2\cos\theta_{2i}l)}{\eta_2\cos\theta_{2i}\cos(k_2\cos\theta_{2i}l)+\eta_1\cos\theta_{1t}j\sin(k_2\cos\theta_{2i}l)}\\
&=\eta_2\cos\theta_{2i}\frac{\eta_1\cos\theta_{1t}+\eta_2\cos\theta_{2i}j\tan(k_2\cos\theta_{2i}l)}{\eta_2\cos\theta_{2i}+\eta_1\cos\theta_{1t}j\tan(k_2\cos\theta_{2i}l)}
\end{aligned} \tag{A.37}$$

The impact of the dielectric layer and the metal ground on the reflection coefficient at the interface $x=0$ can be effectively replaced by an equivalent medium. The intrinsic impedance of this medium serves as the equivalent impedance, set

$$\begin{aligned}
Z_3=\eta_3\cos\theta_{3i}&=\sqrt{\frac{\mu_0}{\varepsilon_0}}\cos\theta_{3i}=\frac{\omega\sqrt{\mu_0\varepsilon_0}\cos\theta_3}{\omega\varepsilon_0}\\
&=\frac{k_3\cos\theta_{3i}}{\omega\varepsilon_0}=\frac{jk_{3x}}{j\omega\varepsilon_0}\;;set\;k_{3x}=k_3\cos\theta_{3i}
\end{aligned} \tag{A.38}$$

$$Z_2=\eta_2\cos\theta_{2i}=\frac{k_2\cos\theta_{2i}}{\omega\varepsilon_2}=\frac{jk_{3x}}{j\omega\varepsilon_r\varepsilon_0};set\;k_{2x}=k_2\cos\theta_{2i} \tag{A.39}$$

$$Z_1 = \eta_1 \cos\theta_{1t} \approx \eta_1 = \sqrt{\frac{\mu_0}{\varepsilon_{metal}}} \approx \sqrt{\frac{j\omega\mu_0}{\sigma_{metal}}} = (1+j)\sqrt{\frac{\omega\mu_0}{2\sigma_{metal}}} \tag{A.40}$$

When the incident angle is Brewster's angle at the interface $x = 0$ between the air layer and the dielectric layer, the reflection component is 0 with $R_3 = 0$.

Bring (A.38),(A.39) and (A.40) into (A.37), get

$$Z_3 = Z_2 \frac{Z_1 + jZ_2 \tan(k_{x2} l)}{Z_2 + jZ_1 \tan(k_{x2} l)} \tag{A.41}$$

Up to this point, Z_3 has been derived as the equation for the equivalent impedance of the surface. In Section A.3, it will continue to follow the derivation approach of the equivalent circuit to establish the same equation.

A.2 Derivation of Equivalent Surface Impedance

Based on Helmholtz equation as above prove, in air layer

$$\gamma_{x_3}^2 + \gamma_z^2 = \gamma_3^2 \tag{A.42}$$

$$k_{x_3}^2 + k_z^2 = k_3^2 = \left(w\sqrt{\mu_0\varepsilon_0}\right)^2 \tag{A.43}$$

$$k_z^2 = k_3^2 - k_{x_3}^2 \tag{A.44}$$

And in dielectric layer

$$\gamma_{x_2}^2 + \gamma_z^2 = \gamma_2^2 \tag{A.45}$$

$$k_{x_2}^2 + k_z^2 = k_2^2 = \left(w\sqrt{\mu_0 \varepsilon_r \varepsilon_0}\right)^2 = \varepsilon_r k_3^2 \tag{A.46}$$

It can be get that

$$k_z^2 = \varepsilon_r k_3^2 - k_{x_2}^2 \tag{A.47}$$

Now we have

$$k_{x_2}^2 = (\varepsilon_r - 1)k_3^2 + k_{x_3}^2 = (\varepsilon_r - 1)w^2 \mu_0 \varepsilon_0 + k_{x_3}^2 \tag{A.48}$$

Solve

$$Z_3 = Z_2 \frac{Z_1 + jZ_2 \tan\left(k_{x_2} l\right)}{Z_2 + jZ_1 \tan\left(k_{x_2} l\right)} \tag{A.49}$$

Since l is very small and $k_{x_2} l \ll 1$, so that $\tan\left(k_{x_2} l\right) \approx k_{x_2} l$, (A.41) can be rewritten as

$$\frac{Z_3}{Z_2}\left(Z_2 + jZ_1 k_{x_2} l\right) = Z_1 + jZ_2 k_{x_2} l \tag{A.50}$$

$$Z_3 = Z_1 + jZ_2 k_{x_2} l - jZ_1 \frac{Z_3}{Z_2} k_{x_2} l \tag{A.51}$$

Bring $Z_3 = \frac{jk_{x3}}{jw\varepsilon_3} = \frac{k_{x3}}{w\varepsilon_0}$ and $Z_2 = \frac{jk_{x2}}{jw\varepsilon_2} = \frac{k_{x2}}{w\varepsilon_r\varepsilon_0}$ into (A.41), get

$$\frac{k_{x3}}{w\varepsilon_0} = Z_1 + j\frac{k_{x2}}{w\varepsilon_r\varepsilon_0}k_{x2}l - jZ_1\frac{k_{x3}}{w\varepsilon_0}\frac{w\varepsilon_r\varepsilon_0}{k_{x2}}k_{x2}l \tag{A.52}$$

Then

$$k_{x3} = w\varepsilon_0 Z_1 + j\frac{k_{x2}^2}{\varepsilon_r}l - jw\varepsilon_r\varepsilon_0 Z_1 k_{x3}l \tag{A.53}$$

Now we get

$$k_{x3} = w\varepsilon_0 Z_1 + j\frac{(\varepsilon_r - 1)}{\varepsilon_r}lw^2\mu_0\varepsilon_0 + jl\frac{1}{\varepsilon_r}k_{x3}^2 - jw\varepsilon_r\varepsilon_0 Z_1 k_{x3}l \tag{A.54}$$

Since $k_{x3}l \ll 1$, omit $jl\frac{1}{\varepsilon_r}k_{x3}^2 - jw\varepsilon_r\varepsilon_0 Z_1 k_{x3}l = 0$, get

$$k_{x3} = w^2\mu_0\varepsilon_0\left[\frac{Z_1}{w\mu_0} + j\frac{(\varepsilon_r - 1)}{\varepsilon_r}l\right] \tag{A.55}$$

where $\frac{Z_1}{w\mu_0} = (1+j)\sqrt{\frac{w\mu_0}{2\sigma_{metal}}}\frac{1}{w\mu_0} = (1+j)\sqrt{\frac{1}{2w\mu_0\sigma_{metal}}} = \frac{\Delta}{2}$, hence

$$k_{x3} = -w^2\mu_0\varepsilon_0\left[\frac{\Delta}{2} + j\frac{(\varepsilon_r - 1)}{\varepsilon_r}l + j\frac{\Delta}{2}\right] \tag{A.56}$$

A.3 Derivation of Field Strength Equations in Surface Wave

The differential form of Maxwell's equations is as follows:

1. Ampere's law with Maxwell's addition:

$$\nabla \times \hat{\boldsymbol{H}} = \hat{\boldsymbol{J}} + \varepsilon_0\frac{\partial \hat{\boldsymbol{E}}}{\partial t} \tag{A.57}$$

2. Faraday's law of electromagnetic induction:

$$\boldsymbol{\nabla} \times \hat{\boldsymbol{E}} = -\mu_0 \frac{\partial \hat{\boldsymbol{H}}}{\partial t} \tag{A.58}$$

3. Gauss's law for magnetic fields:

$$\boldsymbol{\nabla} \cdot \hat{\boldsymbol{H}} = 0 \tag{A.59}$$

4. Gauss's law for electric fields

$$\boldsymbol{\nabla} \cdot \hat{\boldsymbol{E}} = \frac{\rho}{\varepsilon_0} \tag{A.60}$$

where $\hat{\boldsymbol{E}}$ represents the electric field vector, $\hat{\boldsymbol{H}}$ represents the magnetic field vector, ρ is the electric charge density, $\hat{\boldsymbol{J}}$ is the current density, ε_0 is the permittivity of free space, μ_0 is the permeability of free space, $\boldsymbol{\nabla}\cdot$ denotes the divergence operator, and $\boldsymbol{\nabla}\times$ denotes the curl operator. Note that symbols in bold and with a superscript, such as $\hat{\boldsymbol{E}}$, represent vectors indicating direction, while symbols without bold formatting, such as ε_0, represent scalars.

Consider that $\hat{\boldsymbol{E}}$ in the plane wave in free space is a function of $e^{j\omega t}$, here $\frac{\partial \hat{\boldsymbol{E}}}{\partial t} = j\omega \hat{\boldsymbol{E}}$. Then (A.57) can be rewritten as

$$\boldsymbol{\nabla} \times \hat{\boldsymbol{H}} = \sigma \hat{\boldsymbol{E}} + j\omega\varepsilon_0 \hat{\boldsymbol{E}} = (\sigma + j\omega\varepsilon_0)\, \hat{\boldsymbol{E}} \tag{A.61}$$

Expand $\boldsymbol{\nabla} \times \hat{\boldsymbol{H}}$ in the Cartesian coordinate system xyz. (A.61) will be

$$\begin{cases} \hat{\boldsymbol{x}} \left(\dfrac{\partial H_z}{\partial y} - \dfrac{\partial H_y}{\partial z} \right) = (\sigma + j\omega\varepsilon_0)\, \hat{\boldsymbol{E}}_{\boldsymbol{x}} \\ \hat{\boldsymbol{y}} \left(\dfrac{\partial H_x}{\partial z} - \dfrac{\partial H_z}{\partial x} \right) = (\sigma + j\omega\varepsilon_0)\, \hat{\boldsymbol{E}}_{\boldsymbol{y}} \\ \hat{\boldsymbol{z}} \left(\dfrac{\partial H_y}{\partial x} - \dfrac{\partial H_x}{\partial y} \right) = (\sigma + j\omega\varepsilon_0)\, \hat{\boldsymbol{E}}_{\boldsymbol{z}} \end{cases} \tag{A.62}$$

Previously, it is deduced that in this model, only the components in directions

$\hat{\boldsymbol{H}}_{\boldsymbol{y}} = \hat{\boldsymbol{y}} H_y$, $\hat{\boldsymbol{E}}_{\boldsymbol{x}} = \hat{\boldsymbol{x}} E_x$, $\hat{\boldsymbol{E}}_{\boldsymbol{z}} = \hat{\boldsymbol{z}} E_z$ exist, while the components in other directions are all zero. Furthermore, $\hat{\boldsymbol{H}}_{\boldsymbol{y}} = \hat{\boldsymbol{y}} A e^{-jk_z z} e^{-jk_x x} e^{j\omega t} = \hat{\boldsymbol{y}} A e^{-\gamma_z z} e^{-\gamma_x x} e^{j\omega t}$ is obtained. Here $H_y = A e^{-\gamma_z z} e^{-\gamma_x x} e^{j\omega t}$ is the magnitude of $\hat{\boldsymbol{H}}_{\boldsymbol{y}}$. Therefore, (A.62) can be expressed as

$$\begin{cases} \hat{\boldsymbol{E}}_{\boldsymbol{x}} = \hat{\boldsymbol{x}} \left(-\dfrac{\partial H_y}{\partial z} \dfrac{1}{\sigma + j\omega\varepsilon} \right) = \hat{\boldsymbol{x}} \dfrac{\gamma_z}{j\omega\varepsilon_0} A e^{-\gamma_z z} e^{-\gamma_x x} e^{j\omega t} \\ \hat{\boldsymbol{E}}_{\boldsymbol{z}} = \hat{\boldsymbol{z}} \left(\dfrac{\partial H_y}{\partial x} \dfrac{1}{\sigma + j\omega\varepsilon} \right) = -\hat{\boldsymbol{z}} \dfrac{\gamma_x}{j\omega\varepsilon_0} A e^{-\gamma_z z} e^{-\gamma_x x} e^{j\omega t} \end{cases} \tag{A.63}$$

Take the curl on both sides of (A.58) and obtain

$$\boldsymbol{\nabla} \times \left(\boldsymbol{\nabla} \times \hat{\boldsymbol{E}} \right) = -\mu \frac{\partial}{\partial t} \left(\boldsymbol{\nabla} \times \hat{\boldsymbol{H}} \right) \tag{A.64}$$

Take (A.57) into (A.64), get

$$\boldsymbol{\nabla} \times \left(\boldsymbol{\nabla} \times \hat{\boldsymbol{E}} \right) + \mu_0 \varepsilon_0 \frac{\partial^2 \hat{\boldsymbol{E}}}{\partial t} = 0 \tag{A.65}$$

Based on vector identity $\boldsymbol{\nabla} \times \left(\boldsymbol{\nabla} \times \hat{\boldsymbol{E}} \right) = \boldsymbol{\nabla} \left(\boldsymbol{\nabla} \cdot \hat{\boldsymbol{E}} \right) - \boldsymbol{\nabla}^2 \hat{\boldsymbol{E}}$ and $\boldsymbol{\nabla} \left(\boldsymbol{\nabla} \cdot \hat{\boldsymbol{E}} \right) = 0$ in (A.60), then (A.65) can be written as

$$\boldsymbol{\nabla}^2 \hat{\boldsymbol{E}} - \mu_0 \varepsilon_0 \frac{\partial^2 \hat{\boldsymbol{E}}}{\partial t} = 0 \tag{A.66}$$

Here $\frac{\partial \hat{\boldsymbol{E}}}{\partial t} = j\omega \hat{\boldsymbol{E}}$, $\frac{\partial^2 \hat{\boldsymbol{E}}}{\partial t} = -\omega^2 \hat{\boldsymbol{E}}$, then in Helmholtz equation (A.66) will be

$$\left(\boldsymbol{\nabla}^2 + k_0^2 \right) \hat{\boldsymbol{E}} = 0, \tag{A.67}$$

where $k_0 = \omega\sqrt{\mu_0 \varepsilon_0}$, and $\gamma = j k_0 = j\omega\sqrt{\mu_0 \varepsilon_0}$, then it can get

$$\left(\boldsymbol{\nabla}^2 - \gamma^2 \right) \hat{\boldsymbol{E}} = 0, \text{ that is, } \boldsymbol{\nabla}^2 \hat{\boldsymbol{E}} = \gamma^2 \hat{\boldsymbol{E}} \tag{A.68}$$

Left side of (A.68) is

$$\begin{aligned}\nabla^2 \hat{\boldsymbol{E}} &= \hat{\boldsymbol{x}}\nabla^2 E_x + \hat{\boldsymbol{y}}\nabla^2 E_y + \hat{\boldsymbol{z}}\nabla^2 E_z \\ &= \hat{\boldsymbol{x}}\left(\frac{\partial^2 E_x}{\partial x^2} + \frac{\partial^2 E_x}{\partial y^2} + \frac{\partial^2 E_x}{\partial z^2}\right) + \hat{\boldsymbol{y}}\left(\frac{\partial^2 E_y}{\partial x^2} + \frac{\partial^2 E_y}{\partial y^2} + \frac{\partial^2 E_y}{\partial z^2}\right) \\ &+ \hat{\boldsymbol{z}}\left(\frac{\partial^2 E_z}{\partial x^2} + \frac{\partial^2 E_z}{\partial y^2} + \frac{\partial^2 E_z}{\partial z^2}\right) \\ &= \hat{\boldsymbol{x}}E_x\left(\gamma_x^2 + \gamma_z^2\right) + \hat{\boldsymbol{z}}E_z\left(\gamma_x^2 + \gamma_z^2\right)\end{aligned} \tag{A.69}$$

where E_x, E_y, E_z are magnitudes of $\hat{\boldsymbol{E}}_{\boldsymbol{x}}$, $\hat{\boldsymbol{E}}_{\boldsymbol{y}}$, $\hat{\boldsymbol{E}}_{\boldsymbol{z}}$, respectively. And right side of (A.68) is

$$\begin{aligned}\gamma^2\hat{\boldsymbol{E}} &= \gamma^2\left(\hat{\boldsymbol{x}}E_x + \hat{\boldsymbol{y}}E_y + \hat{\boldsymbol{z}}E_z\right) \\ &= \hat{\boldsymbol{x}}\gamma^2 E_x + \hat{\boldsymbol{z}}\gamma^2 E_z\end{aligned} \tag{A.70}$$

Combine (A.69) and (A.70), get

$$\begin{gathered}\hat{\boldsymbol{x}}E_x\left(\gamma_x^2 + \gamma_z^2\right) + \hat{\boldsymbol{z}}E_z\left(\gamma_x^2 + \gamma_z^2\right) = \hat{\boldsymbol{x}}\gamma^2 E_x + \hat{\boldsymbol{z}}\gamma^2 E_z \\ \text{that is, } \gamma_x^2 + \gamma_z^2 = \gamma^2\end{gathered} \tag{A.71}$$

Combine (A.63), (A.71), the equations of surface wave in air layer can be obtained

$$\begin{cases}\hat{\boldsymbol{H}}_{\boldsymbol{y}} = \hat{\boldsymbol{y}}Ae^{-\gamma_z z}e^{-\gamma_x x}e^{j\omega t} \\ \hat{\boldsymbol{E}}_{\boldsymbol{x}} = \hat{\boldsymbol{x}}\dfrac{\gamma_z}{j\omega\varepsilon_0}Ae^{-\gamma_z z}e^{-\gamma_x x}e^{j\omega t} \\ \hat{\boldsymbol{E}}_{\boldsymbol{z}} = -\hat{\boldsymbol{z}}\dfrac{\gamma_x}{j\omega\varepsilon_0}Ae^{-\gamma_z z}e^{-\gamma_x x}e^{j\omega t} \\ \gamma_x^2 + \gamma_z^2 = \gamma^2\end{cases} \tag{A.72}$$

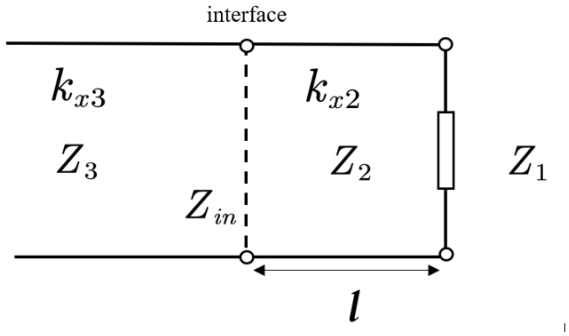

Figure A.2: An equivalent circuit diagram of a basic surface.

A.4 Equivalent Transmission Line

Fig. A.2 shows an equivalent circuit diagram of a basic surface, here two equations describe the circuit elements

$$i-\left(i+\frac{\partial i}{\partial x}dx\right)=G_0\left(u+\frac{\partial u}{\partial x}dx\right)dx+C_0\frac{\partial}{\partial x}\left(u+\frac{\partial u}{\partial x}dx\right)dx \tag{A.73}$$

And

$$u-\left(u+\frac{\partial u}{\partial x}dx\right)=R_0 i dx+L_0\frac{\partial i}{\partial t}dx \tag{A.74}$$

The coupled differential equations are derived

$$\begin{cases}-\dfrac{\partial u}{\partial x}=R_0 i+L_0\dfrac{\partial i}{\partial t}\\ -\dfrac{\partial i}{\partial x}=G_0 i+C_0\dfrac{\partial u}{\partial t}\end{cases} \tag{A.75}$$

In terms of real and imaginary parts

$$u(x,t)=\mathrm{Re}\left[\sqrt{2}U(x)\,e^{jwt}\right] \tag{A.76}$$

$$i(x,t) = \mathrm{Re}\left[\sqrt{2} I(x) e^{jwt}\right] \tag{A.77}$$

The impedances are

$$\begin{cases} -\dfrac{dU}{dx} = (R_0 + jwL_0) I = Z_0 I \\ Z_0 = (R_0 + jwL_0) \\ -\dfrac{dI}{dx} = (G_0 + jwC_0) U = Y_0 U \\ Y_0 = (G_0 + jwC_0) \end{cases} \tag{A.78}$$

And the wave equations for voltage and current are obtained

$$\frac{d^2U}{dx^2} = Z_0 Y_0 U \tag{A.79}$$

$$\frac{d^2I}{dx^2} = Z_0 Y_0 I \tag{A.80}$$

The propagation constant is defined as

$$\gamma = jk = \sqrt{Z_0 Y_0} = \sqrt{(R_0 + jwL_0)(G_0 + jwC_0)} \tag{A.81}$$

General solutions for U and I are given

$$\frac{d^2U}{dx^2} = \gamma^2 U \tag{A.82}$$

$$\frac{d^2I}{dx^2} = \gamma^2 I \tag{A.83}$$

$$\begin{cases} U = A_1 e^{-\gamma x} + A_2 e^{\gamma x} \\ I = B_1 e^{-\gamma x} + B_2 e^{\gamma x} \end{cases} \tag{A.84}$$

And then

$$\begin{aligned} I &= -\frac{1}{Z_0}\frac{dU}{dx} = -\frac{1}{Z_0}\left(-A_1\gamma e^{-\gamma x} + A_2\gamma e^{\gamma x}\right) \\ &= \frac{A_1}{\sqrt{\frac{Z_0}{Y_0}}}e^{-\gamma x} - \frac{A_2}{\sqrt{\frac{Z_0}{Y_0}}}e^{-\gamma x} = B_1 e^{-\gamma x} + B_2 e^{\gamma x} \end{aligned} \tag{A.85}$$

$$Z_{characteristic} = \sqrt{\frac{Z_0}{Y_0}} = \sqrt{\frac{(R_0 + jwL_0)}{(G_0 + jwC_0)}} \tag{A.86}$$

Expressions for B_1 and B_2 in terms of Z_c are given

$$B_1 = \frac{A_1}{\sqrt{\frac{Z_0}{Y_0}}} = \frac{A_1}{Z_c} \tag{A.87}$$

$$B_2 = -\frac{A_2}{\sqrt{\frac{Z_0}{Y_0}}} = -\frac{A_2}{Z_c} \tag{A.88}$$

$$\begin{cases} U = A_1 e^{-\gamma x} + A_2 e^{\gamma x} \\ I = \dfrac{A_1}{Z_c} e^{-\gamma x} - \dfrac{A_2}{Z_c} e^{\gamma x} \end{cases} \tag{A.89}$$

$$x = d\ U\prime I\prime \tag{A.90}$$

The final expression can be get

$$\begin{cases} U\prime = A_1 e^{-\gamma d} + A_2 e^{\gamma d} \\ I\prime = \dfrac{A_1}{Z_c} e^{-\gamma d} - \dfrac{A_2}{Z_c} e^{\gamma d} \end{cases} \tag{A.91}$$

$$A_1 = \frac{1}{2}\left(U\prime + Z_c I\prime\right) e^{\gamma d} \tag{A.92}$$

$$A_2 = \frac{1}{2}\left(U\prime - Z_c I\right) e^{-\gamma d} \tag{A.93}$$

And then

$$\begin{cases} U = \dfrac{1}{2}\left(U\prime + Z_c I\prime\right) e^{\gamma(d-x)} + \dfrac{1}{2}\left(U\prime - Z_c I\right) e^{-\gamma(d-x)} \\ I = \dfrac{1}{2}\left(\dfrac{U\prime}{Z_c} + I\prime\right) e^{\gamma(d-x)} - \dfrac{1}{2}\left(\dfrac{U\prime}{Z_c} - I\prime\right) e^{-\gamma(d-x)} \end{cases} \tag{A.94}$$

$$\begin{cases} U = \dfrac{1}{2}\left(U\prime + Z_c I\prime\right) e^{\gamma x\prime} + \dfrac{1}{2}\left(U\prime - Z_c I\right) e^{-\gamma x\prime} \\ I = \dfrac{1}{2}\left(\dfrac{U\prime}{Z_c} + I\prime\right) e^{\gamma x\prime} - \dfrac{1}{2}\left(\dfrac{U\prime}{Z_c} - I\prime\right) e^{-\gamma x\prime} \end{cases} \tag{A.95}$$

Now we get

$$\begin{cases} U = \dfrac{1}{2}U\prime e^{\gamma x} + \dfrac{1}{2}U\prime e^{-\gamma x} + \dfrac{1}{2}Z_c I\prime e^{\gamma x} - \dfrac{1}{2}Z_c I\prime e^{\gamma x} = U\prime\cosh(\gamma x) + Z_c I\prime\sinh(\gamma x) \\ I = \dfrac{1}{2}\dfrac{U\prime}{Z_c} e^{\gamma x} - \dfrac{1}{2}\dfrac{U\prime}{Z_c} e^{-\gamma x} + \dfrac{1}{2}I\prime e^{\gamma x} + \dfrac{1}{2}I\prime e^{-\gamma x} = I\prime\cosh(\gamma x) + \dfrac{U\prime}{Z_c}\sinh(\gamma x) \end{cases} \tag{A.96}$$

$$\cosh(x) = \frac{e^x + e^{-x}}{2} \quad \sinh(x) = \frac{e^x - e^{-x}}{2} \tag{A.97}$$

$$\cos(x) = \frac{e^{jx} + e^{-jx}}{2} \; j\sin(x) = \frac{e^{jx} - e^{-jx}}{2} \tag{A.98}$$

$$U = U\prime\cos(kx) + jZ_c I\prime\sin(kx) \tag{A.99}$$

Therefore

$$I = I\prime\cos(kx) + j\frac{U\prime}{Z_c}\sin(kx) \tag{A.100}$$

The input impedance is calculated as

$$\begin{aligned} Z_{in-x} = \frac{U_x}{I_x} &= \frac{U\prime\cos(kx) + jZ_c I\prime\sin(kx)}{I\prime\cos(kx) + j\frac{U\prime}{Z_c}\sin(kx)} = \frac{\frac{U\prime}{I\prime}\cos(kx) + jZ_c\sin(kx)}{\cos(kx) + j\frac{U\prime}{I\prime Z_c}\sin(kx)} \\ &= Z_c\frac{Z_1\cos(kx) + jZ_c\sin(kx)}{Z_c\cos(kx) + jZ_1\sin(kx)} = Z_c\frac{Z_1 + jZ_c\tan(kx)}{Z_c + jZ_1\tan(kx)} \end{aligned} \tag{A.101}$$

Bibliography

[1] A. Shojaeifard, K.-K. Wong, K.-F. Tong, Z. Chu, A. Mourad, A. Haghighat, I. Hemadeh, N. T. Nguyen, V. Tapio, and M. Juntti. MIMO evolution beyond 5G through reconfigurable intelligent surfaces and fluid antenna systems. *Proceedings of the IEEE*, 110(9):1244–1265, 2022.

[2] K.-K. Wong, K.-F. Tong, Z. Chu, and Y. Zhang. A vision to smart radio environment: Surface wave communication superhighways. *IEEE Wireless Communications*, 28(1):112–119, 2020.

[3] O. Balosso, J. Sokoloff, and S. Bolioli. Brief overview about surface wave theory and applications. In *2012 15 International Symposium on Antenna Technology and Applied Electromagnetics*, pages 1–7. IEEE, 2012.

[4] J. Wait. Excitation of surface waves on conducting, stratified, dielectric-clad, and corrugated surfaces. *Journal of Research of the National Bureau of Standards*, 59(6):365–377, 1957.

[5] D. González-Ovejero, E. Martini, B. Loiseaux, C. Tripon-Canseliet, M. Mencagli, J. Chazelas, and S. Maci. Basic properties of checkerboard metasurfaces. *IEEE Antennas and Wireless Propagation Letters*, 14:406–409, 2014.

[6] S. H. Kim, Y. Kim, and Y. J. Yoon. Low-profile checkerboard electromagnetic band-gap surface. In *2016 International Symposium on Antennas and Propagation (ISAP)*, pages 488–489. IEEE, 2016.

[7] V. Popov, A. Díaz-Rubio, V. Asadchy, S. Tcvetkova, F. Boust, S. Tretyakov, and S. N. Burokur. Omega-bianisotropic metasurface for converting a propagating wave into a surface wave. *Physical Review B*, 100(12):125103, 2019.

[8] H. Barlow. Surface waves. *Proceedings of the IRE*, 46(7):1413–1417, 1958.

[9] A. Karkar, J. Turner, K.-F. Tong, R. AI-Dujaily, T. Mak, A. Yakovlev, and F. Xia. Hybrid wire-surface wave interconnects for next-generation networks-on-chip. *IET Computers and Digital Techniques*, 7(6):294–303, 2013.

[10] A. Karkar, N. Dahir, T. Mak, and K.-F. Tong. Thermal and performance efficient on-chip surface-wave communication for many-core systems in dark silicon era. *ACM Journal on Emerging Technologies in Computing Systems (JETC)*, 18(3):1–18, 2022.

[11] M. Lieberman, J.-P. Booth, P. Chabert, J.-M. Rax, and M. Turner. Standing wave and skin effects in large-area, high-frequency capacitive discharges. *Plasma Sources Science and Technology*, 11(3):283, 2002.

[12] J. Turner, M. Jessup, and K.-F. Tong. A novel technique enabling the realization of 60 GHz body area networks. In *2012 Ninth International Conference on Wearable and Implantable Body Sensor Networks*, pages 58–62. IEEE, 2012.

[13] H. Wang, Y. Shen, K.-F. Tong, and K.-K. Wong. Continuous electrowetting surface-wave fluid antenna for mobile communications. In *TENCON 2022-2022 IEEE Region 10 Conference (TENCON)*, pages 1–3. IEEE, 2022.

[14] J. O. Martínez, J. R. Rodríguez, Y. Shen, K.-F. Tong, K.-K. Wong, and A. G. Armada. Toward liquid reconfigurable antenna arrays for wireless communications. *IEEE Communications Magazine*, 60(12):145–151, 2022.

[15] J. Turner and M. Jessup. How surface waves reduce through-life costs. *Measurement and Control*, 46(6):180–184, 2013.

[16] T. Sarkar, M. Abdallah, M. Salazar-Palma, and W. Dyab. Surface Plasmons-Polaritons, Surface waves, and Zenneck waves: Clarification of the terms and a description of the concepts and their evolution. *IEEE Antennas and Propagation Magazine*, 59(3):77–93, 2017.

[17] J. Zenneck. Propagation of plane EM waves along a plane conducting surface. *Annals of Physics*, 23(1):907, 1907.

[18] J. Zenneck. Über die fortpflanzung ebener elektromagnetischer wellen längs einer ebenen leiterfläche und ihre beziehung zur drahtlosen telegraphie. *Annalen der Physik*, 328(10):846–866, 1907.

[19] H. Wise. The physical reality of Zenneck's surface wave. *Bell System Technical Journal*, 16(1):35–44, 1937.

[20] H. Barlow and A. Cullen. Surface waves. *Proceedings of the IEE-Part III: Radio and Communication Engineering*, 100(68):329–341, 1953.

[21] H. Barlow and A. E. Karbowiak. An experimental investigation of the properties of corrugated cylindrical surface waveguides. *Proceedings of the IEE-part III: Radio and Communication Engineering*, 101(71):182–188, 1954.

[22] H. Barlow and J. Brown. *Radio surface waves*. Clarendon Press, 1962.

[23] J. Turner. Isolation of the Zenneck surface wave: Update. 2013.

[24] T.-I. Jeon and D. Grischkowsky. THz Zenneck surface wave (THz surface plasmon) propagation on a metal sheet. *Applied Physics Letters*, 88(6), 2006.

[25] J. Wan, K.-F. Tong, and C. H. Chan. Simulation and experimental verification for a 52 GHz wideband trapped surface wave propagation system. *IEEE Transactions on Antennas and Propagation*, 67(4):2158–2166, 2019.

[26] M. Hayes and R. Rivlin. Surface waves in deformed elastic materials. *Archive for Rational Mechanics and Analysis*, 8:358–380, 1961.

[27] E. Johansen. Surface wave scattering by a step. *IEEE Transactions on Antennas and Propagation*, 15(3):442–448, 1967.

[28] E. Johansen. Surface wave radiation from a thick, semi-infinite plane with a reactive surface. *IEEE Transactions on Antennas and Propagation*, 16(4):391–398, 1968.

[29] M. Tsuji, H. Shigesawa, and A. Oliner. New surface-wave-like mode on CPWs of infinite width and its role in explaining the leakage cancellation effect. In *1992 IEEE MTT-S Microwave Symposium Digest*, pages 495–498. IEEE, 1992.

[30] I. Tayyar. Surface wave scattering by a material filled rectangular impedance groove in a reactive plane. *Wave Motion*, 48(1):24–38, 2011.

[31] S. Sun, K.-Y. Yang, C.-M. Wang, T.-K. Juan, W. T. Chen, C. Y. Liao, Q. He, S. Xiao, W.-T. Kung, G.-Y. Guo, et al. High-efficiency broadband anomalous reflection by gradient meta-surfaces. *Nano Letters*, 12(12):6223–6229, 2012.

[32] Z. Sun, X. Zuo, T. Guan, and W. Chen. Artificial TE-mode surface waves at metal surfaces mimicking surface plasmons. *Optics Express*, 22(4):4714–4722, 2014.

[33] Y. Liu, C. Ouyang, P. Zheng, J. Ma, Q. Xu, X. Su, Y. Li, Z. Tian, J. Gu, L. Liu, et al. Simultaneous manipulation of electric and magnetic surface waves by topological hyperbolic metasurfaces. *ACS Applied Electronic Materials*, 3(9):4203–4209, 2021.

[34] D. González-Ovejero, E. Martini, and S. Maci. Surface waves supported by metasurfaces with self-complementary geometries. *IEEE Transactions on Antennas and Propagation*, 63(1):250–260, 2014.

[35] S. H. Kim and Y. J. Yoon. Wideband radar cross-section reduction on checkerboard metasurfaces with surface wave suppression. *IEEE Antennas and Wireless Propagation Letters*, 18(5):896–900, 2019.

[36] R. Mitchell-Thomas, T. McManus, O. Quevedo-Teruel, S. Horsley, and Y. Hao. Perfect surface wave cloaks. *Physical Review Letters*, 111(21):213901, 2013.

[37] T. McManus, J. Valiente-Kroon, S. Horsley, and Y. Hao. Illusions and cloaks for surface waves. *Scientific Reports*, 4(1):5977, 2014.

[38] T. McManus, L. La Spada, and Y. Hao. Isotropic and anisotropic surface wave cloaking techniques. *Journal of Optics*, 18(4):044005, 2016.

[39] S. Xu, H. Xu, H. Gao, Y. Jiang, F. Yu, J. D. Joannopoulos, M. Soljačić, H. Chen, H. Sun, and B. Zhang. Broadband surface-wave transformation cloak. *Proceedings of the National Academy of Sciences*, 112(25):7635–7638, 2015.

[40] L. Jing, B. Zheng, S. Xu, L. Shen, and H. Chen. Experimental study on invisibility cloaks. In *2016 IEEE International Workshop on Electromagnetics: Applications and Student Innovation Competition (iWEM)*, pages 1–3. IEEE, 2016.

[41] S. Tcvetkova, D.-H. Kwon, A. Diaz-Rubio, and S. Tretyakov. Nearly perfect conversion of a propagating wave into a surface wave. In *2017 International Conference on Electromagnetics in Advanced Applications (ICEAA)*, pages 1426–1428. IEEE, 2017.

[42] S. Tcvetkova, D.-H. Kwon, A. Díaz-Rubio, and S. Tretyakov. Near-perfect conversion of a propagating plane wave into a surface wave using metasurfaces. *Physical Review B*, 97(11):115447, 2018.

[43] S. Tcvetkova, E. Martini, S. Tretyakov, and S. Maci. Perfect conversion of a TM surface wave into a TM leaky wave by an isotropic periodic metasurface printed on a grounded dielectric slab. *IEEE Transactions on Antennas and Propagation*, 68(8):6145–6153, 2020.

[44] S. Tcvetkova, S. Maci, and S. Tretyakov. Exact solution for conversion of surface waves to space waves by periodical impenetrable metasurfaces. *IEEE Transactions on Antennas and Propagation*, 67(5):3200–3207, 2019.

[45] B. Liang and M. Bai. Subwavelength three-dimensional frequency selective surface based on surface wave tunneling. *Optics Express*, 24(13):14697–14702, 2016.

[46] E. Basar, M. Renzo, J. De Rosny, M. Debbah, M.-S. Alouini, and R. Zhang. Wireless communications through reconfigurable intelligent surfaces. *IEEE Access*, 7:116753–116773, 2019.

[47] IMT-2030 Promotion Group. White paper on 6G vision and candidate technologies. 2021.

[48] University of Surrey 5GIC Strategy Advisory Board. 6G wireless: A new strategic vision. 2020.

[49] M. Renzo, A. Zappone, M. Debbah, M.-S. Alouini, C. Yuen, J. De Rosny, and S. Tretyakov. Smart radio environments empowered by reconfigurable intelligent surfaces: How it works, state of research, and the road ahead. *IEEE Journal on Selected Areas in Communications*, 38(11):2450–2525, 2020.

[50] M. Elmossallamy, H. Zhang, L. Songyang, K. Seddik, Z. Han, and G. Y. Li. Reconfigurable intelligent surfaces for wireless communications: Principles, challenges, and opportunities. *IEEE Transactions on Cognitive Communications and Networking*, 6(3):990–1002, 2020.

[51] Y. Liu, X. Liu, X. Mu, T. Hou, J. Xu, M. Renzo, and N. Al-Dhahir. Reconfigurable intelligent surfaces: Principles and opportunities. *IEEE Communications Surveys and Tutorials*, 23(3):1546–1577, 2021.

[52] C. Huang, A. Zappone, G. Alexandropoulos, M. Debbah, and C. Yuen. Reconfigurable intelligent surfaces for energy efficiency in wireless communi-

cation. *IEEE Transactions on Wireless Communications*, 18(8):4157–4170, 2019.

[53] M. Renzo and A. Aravanis. Catching the 6G wave by using metamaterials: A reconfigurable intelligent surface paradigm. *Shaping Future 6G Networks: Needs, Impacts, and Technologies*, pages 69–87, 2021.

[54] F. Yang, A. Aminian, and Y. Rahmat-Samii. A novel surface-wave antenna design using a thin periodically loaded ground plane. *Microwave and Optical Technology Letters*, 47(3):240–245, 2005.

[55] Z. Liu, Z. Xue, and B. Gao. Research on the EM field on the surface of a surface wave antenna. In *2007 International Symposium on Microwave, Antenna, Propagation and EMC Technologies for Wireless Communications*, pages 695–698. IEEE, 2007.

[56] S. Podilchak, A. Freundorfer, and Y. Antar. Planar leaky-wave antenna designs offering conical-sector beam scanning and broadside radiation using surface-wave launchers. *IEEE Antennas and Wireless Propagation Letters*, 7:155–158, 2008.

[57] S. Podilchak, A. Freundorfer, and Y. Antar. Surface-wave launchers for beam steering and application to planar leaky-wave antennas. *IEEE Transactions on Antennas and Propagation*, 57(2):355–363, 2009.

[58] P. Delmote and F. Bieth. Additional lens for TEM horn antenna and transient high-power application: Design and characterization in time domain. In *2021 15th European Conference on Antennas and Propagation (EuCAP)*, pages 1–5. IEEE, 2021.

[59] Z. Chen, R. Xu, and Z. Shen. Design of a broadband antenna array with compact surface-wave antenna elements. *IEEE Antennas and Wireless Propagation Letters*, 21(2):337–340, 2021.

[60] E. Martini, M. Faenzi, D. González-Ovejero, and S. Maci. Surface-wave based metasurface antennas. *Antenna and Array Technologies for Future Wireless Ecosystems*, pages 1–41, 2022.

[61] M. Bodehou, K. Khalifeh, S. N. Jha, and C. Craeye. Direct numerical inversion methods for the design of surface wave-based metasurface antennas: Fundamentals, realizations, and perspectives. *IEEE Antennas and Propagation Magazine*, 64(4):24–36, 2022.

[62] M. Mencagli, E. Martini, and S. Maci. Surface wave dispersion for anisotropic metasurfaces constituted by elliptical patches. *IEEE Transactions on Antennas and Propagation*, 63(7):2992–3003, 2015.

[63] M. Kuznetcov, V. G. Buendía, Z. Shafiq, L. Matekovits, D. Anagnostou, and S. Podilchak. Printed leaky-wave antenna with aperture control using width-modulated microstrip lines and TM surface-wave feeding by SIW technology. *IEEE Antennas and Wireless Propagation Letters*, 18(9):1809–1813, 2019.

[64] D. Comite, M. Kuznetcov, V. G. Buendía, S. Podilchak, P. Baccarelli, P. Burghignoli, and A. Galli. Directive 2-D beam steering by means of a multiport radially periodic leaky-wave antenna. *IEEE Transactions on Antennas and Propagation*, 69(5):2494–2506, 2020.

[65] J. Liu, D. Jackson, and Y. Long. Substrate integrated waveguide (SIW) leaky-wave antenna with transverse slots. *IEEE Transactions on Antennas and Propagation*, 60(1):20–29, 2011.

[66] K. Alrushud, V. G. Buendía, and S. Podilchak. Compact substrate integrated waveguide quasi-endfire antenna for Cubesat integration. *IEEE Antennas and Wireless Propagation Letters*, 20(11):2120–2124, 2021.

[67] Z. Shafiq, M. Kuznetcov, V. G. Buendia, D. Anagnostou, and S. Podilchak. A planar horn antenna for TM surface wave launching using substrate inte-

grated waveguide technology. In *2019 13th European Conference on Antennas and Propagation (EuCAP)*, pages 1–3. IEEE, 2019.

[68] Y. Cassivi, L. Perregrini, P. Arcioni, M. Bressan, K. Wu, and G. Conciauro. Dispersion characteristics of substrate integrated rectangular waveguide. *IEEE Microwave and Wireless Components Letters*, 12(9):333–335, 2002.

[69] K. Wu, D. Deslandes, and Y. Cassivi. The substrate integrated circuits-a new concept for high-frequency electronics and optoelectronics. In *6th International Conference on Telecommunications in Modern Satellite, Cable and Broadcasting Service, 2003. TELSIKS 2003.*, volume 1, pages P–III. IEEE, 2003.

[70] M. Bozzi, A. Georgiadis, and K. Wu. Review of substrate-integrated waveguide circuits and antennas. *IET Microwaves, Antennas & Propagation*, 5(8):909–920, 2011.

[71] M. Ebrahimpouri, O. Quevedo-Teruel, and E. Rajo-Iglesias. Design guidelines for gap waveguide technology based on glide-symmetric holey structures. *IEEE Microwave and Wireless Components Letters*, 27(6):542–544, 2017.

[72] E. Rajo-Iglesias, Z. Sipus, A. Uz Zaman, F. Yang, and Y. Rahmat-Samii. Gap waveguide technology. In *Surface Electromagnetics: With Applications in Antenna, Microwave, and Optical Engineering*, pages 198–230. Cambridge Univ. Press, 2019.

[73] Y. Shen, K.-F. Tong, and K.-K. Wong. Beam-steering surface wave fluid antennas for MIMO applications. In *2020 IEEE Asia-Pacific Microwave Conference (APMC)*, pages 634–636. IEEE, 2020.

[74] Y. Shen, K.-F. Tong, and K.-K. Wong. Reconfigurable surface wave fluid antenna for spatial MIMO applications. In *2021 IEEE-APS Topical Conference*

on Antennas and Propagation in Wireless Communications (APWC), pages 150–152. IEEE, 2021.

[75] Y. Shen, K.-F. Tong, and K.-K. Wong. Radiation pattern diversified single-fluid-channel surface-wave antenna for mobile communications. In *2022 IEEE-APS Topical Conference on Antennas and Propagation in Wireless Communications (APWC)*, pages 049–051. IEEE, 2022.

[76] W. Dyab, M. Abdallah, T. Sarkar, and M. Salazar-Palma. On the relation between surface plasmons and sommerfeld's surface electromagnetic waves. In *2013 IEEE MTT-S International Microwave Symposium Digest (MTT)*, pages 1–4. IEEE, 2013.

[77] Z. Sun, T. Guan, W. Chen, and X. Zuo. Transmission of TE-polarized light through metallic nanoslit arrays assisted by a quasi surface wave. *Applied Physics Express*, 7(3):032001, 2014.

[78] P. Danilov, A. Ionin, S. Kudryashov, S. Makarov, A. Rudenko, P. Saltuganov, L. Seleznev, V. Yurovskikh, D. Zayarny, and T. Apostolova. Silicon as a virtual plasmonic material: Acquisition of its transient optical constants and the ultrafast surface plasmon-polariton excitation. *Journal of Experimental and Theoretical Physics*, 120:946–959, 2015.

[79] A. Cardin, S. Silva, S. Vardeny, W. Padilla, A. Saxena, A. Taylor, W. Kort-Kamp, H. T. Chen, D. Dalvit, and A. Azad. Surface-wave-assisted nonreciprocity in spatio-temporally modulated metasurfaces. *Nature Communications*, 11(1):1469, 2020.

[80] W. C. Chen, A. Cardin, M. Koirala, X. Liu, T. Tyler, K. West, C. Bingham, T. Starr, A. Starr, N. Jokerst, et al. Role of surface electromagnetic waves in metamaterial absorbers. *Optics Express*, 24(6):6783–6792, 2016.

[81] M. M. Moeini, H. Oraizi, A. Amini, and V. Nayyeri. Wide-band beam-scanning by surface wave confinement on leaky wave holograms. *Scientific Reports*, 9(1):13227, 2019.

[82] M. M. Moeini, H. Oraizi, and A. Amini. Collimating cylindrical surface leaky waves for highly improved radiation characteristics of holograms. *Physical Review Applied*, 11(4):044006, 2019.

[83] M. M. Moeini, H. Oraizi, and A. Amini. Embedding parabolic reflector on hologram for redirecting surface leaky waves into forward ones. In *2019 URSI International Symposium on Electromagnetic Theory (EMTS)*, pages 1–4. IEEE, 2019.

[84] H. Emamian, H. Oraizi, and M. M. Moeini. Design of wide-band dual-beam leaky-wave antenna using the holographic theory. In *2019 27th Iranian Conference on Electrical Engineering (ICEE)*, pages 1456–1460. IEEE, 2019.

[85] A. Amini, H. Oraizi, M. Movahediqomi, and M. M. Moeini. Adiabatic floquet-wave solutions of temporally modulated anisotropic leaky-wave holograms. *arXiv preprint arXiv:2206.00797*, 2022.

[86] R. Yang and Y. Hao. An accurate control of the surface wave using transformation optics. *Optics Express*, 20(9):9341–9350, 2012.

[87] R. Yang, Z. Lei, L. Chen, Z. Wang, and Y. Hao. Surface wave transformation lens antennas. *IEEE Transactions on Antennas and Propagation*, 62(2):973–977, 2013.

[88] M. Salucci, F. Boulos, A. Polo, and G. Oliveri. Conformal transformation electromagnetics based on Schwarz-Christoffel mapping for the synthesis of doubly connected metalenses. *IEEE Transactions on Antennas and Propagation*, 68(3):1836–1850, 2019.

[89] C. Wei, M. Cen, H.-C. Chui, and T. Cao. Surface wave direction control on curved surfaces. *Journal of Physics D: Applied Physics*, 54(7):074003, 2020.

[90] Y. Takano and A. Sanada. Novel design of an anisotropic dielectric lens with spatially discontinuous boundary based on Quasi-conformal transfor-

mation electromagnetics. In *2020 IEEE Asia-Pacific Microwave Conference (APMC)*, pages 1048–1050. IEEE, 2020.

[91] M. Junqueira, L. Gabrielli, and D. Spadoti. Comparison of anisotropy reduction strategies for transformation optics designs. *IEEE Photonics Journal*, 7(1):1–10, 2015.

[92] R. Yang. Controlling surface waves using transformation optics. In *2016 IEEE MTT-S International Microwave Workshop Series on Advanced Materials and Processes for RF and THz Applications (IMWS-AMP)*, pages 1–3. IEEE, 2016.

[93] W. Bai, H. Yang, Y. Ma, H. Chen, J. Shin, Y. Liu, Q. Yang, I. Kandela, Z. Liu, S.-K. Kang, et al. Flexible transient optical waveguides and surface-wave biosensors constructed from monocrystalline silicon. *Advanced Materials*, 30(32):1801584, 2018.

[94] H. Zhang, H. Zhao, X. Zhao, C. Xu, D. Franklin, A. Vázquez-Guardado, W. Bai, J. Zhao, K. Li, G. Monti, et al. Biocompatible light guide-assisted wearable devices for enhanced UV light delivery in deep skin. *Advanced Functional Materials*, 31(23):2100576, 2021.

[95] F. Fuschini, M. Barbiroli, M. Zoli, G. Bellanca, G. Calò, P. Bassi, and V. Petruzzelli. Ray tracing modeling of electromagnetic propagation for on-chip wireless optical communications. *Journal of Low Power Electronics and Applications*, 8(4):39, 2018.

[96] J. Schäfer, H. Gulan, D. Müller, and T. Zwick. On-chip millimeter wave surface wave launcher for off-chip leaky wave antennas. In *2018 48th European Microwave Conference (EuMC)*, pages 1113–1116. IEEE, 2018.

[97] L. Berkelmann and D. Manteuffel. Antenna parameters for on-body communications with wearable and implantable antennas. *IEEE Transactions on Antennas and Propagation*, 69(9):5377–5387, 2021.

[98] T. Neumann and M. Dickey. Liquid metal direct write and 3D printing: a review. *Advanced Materials Technologies*, 5(9):2000070, 2020.

[99] S. Chen, Z. Cui, H. Wang, X. Wang, and J. Liu. Liquid metal flexible electronics: Past, present, and future. *Applied Physics Reviews*, 10(2), 2023.

[100] Y. Yu, J. Guo, B. Ma, D. Zhang, and Y. Zhao. Liquid metal-integrated ultraelastic conductive microfibers from microfluidics for wearable electronics. *Science Bulletin*, 65(20):1752–1759, 2020.

[101] S.-Y. Tang, K. Khoshmanesh, V. Sivan, P. Petersen, A. P. O'Mullane, D. Abbott, A. Mitchell, and K. Kalantar-Zadeh. Liquid metal enabled pump. *Proceedings of the National Academy of Sciences*, 111(9):3304–3309, 2014.

[102] Y. Huang, L. Xing, C. Song, S. Wang, and F. Elhouni. Liquid antennas: Past, present and future. *IEEE Open Journal of Antennas and Propagation*, 2:473–487, 2021.

[103] K. Khoshmanesh, S.-Y. Tang, J. Y. Zhu, S. Schaefer, A. Mitchell, K. Kalantar-Zadeh, and M. Dickey. Liquid metal enabled microfluidics. *Lab on a Chip*, 17(6):974–993, 2017.

[104] Darwin Microfluidics. BT100-1L Multichannel (4-24) peristaltic pump. [Online] https://darwin-microfluidics.com/collections/peristaltic-pumps-systems-drives/products/microfluidic-2-24-channel-peristaltic-pump?variant=92609675265.

[105] Darwin Microfluidics. NE-1200 Syringe twelve programmable multichannel syringe pump. [Online] https://darwin-microfluidics.com/collections/syringe-pump/products/syringetwelve-programmable-multichannel-syringe-pump.

[106] C.-L. Sotiropoulou, L. Voudouris, C. Gentsos, A. Demiris, N. Vassiliadis, and S. Nikolaidis. Real-time machine vision FPGA implementation for microflu-

idic monitoring on lab-on-chips. *IEEE Transactions on Biomedical Circuits and Systems*, 8(2):268–277, 2013.

[107] X.-D. Liu, Z.-L. Hou, B.-X. Zhang, K.-T. Zhan, P. He, K.-L. Zhang, and W.-L. Song. A general model of dielectric constant for porous materials. *Applied Physics Letters*, 108(10):102902, 2016.

[108] T. K. Geok, F. Hossain, M. N. Kamaruddin, N. Z. A. Rahman, S. Thiagarajah, A. T. W. Chiat, and C. P. Liew. A comprehensive review of efficient ray-tracing techniques for wireless communication. *International Journal on Communications Antenna and Propagation*, 8(2):123–136, 2018.

[109] C. Schüßler, M. Hoffmann, J. Bräunig, I. Ullmann, R. Ebelt, and M. Vossiek. A realistic radar ray tracing simulator for large mimo-arrays in automotive environments. *IEEE Journal of Microwaves*, 1(4):962–974, 2021.

[110] H. Choi, J. Oh, J. Chung, G. C. Alexandropoulos, and J. Choi. Withray: A versatile ray-tracing simulator for smart wireless environments. *IEEE Access*, 2023.

[111] Tektronix. What is a Vector Network Analyzer and how does it work. [Online]https://www.tek.com/en/documents/primer/what-vector-network-analyzer-and-how-does-it-work.

[112] Tektronix. Etsi tr 138 913. Study on channel models for mm-wave bands. [Online]https://www.etsi.org.

[113] ECO. Ecc decision (15)01 - technical and operational requirements for the use of the frequency band 24.25-27.5 GHz for 5G networks. [Online]https://docdb.cept.org.

[114] Nano Dimension. A multi-material, multi-layer 3D printer that generates entire circuits in one step–including substrate, conductive traces, and passive components. [Online] https://www.nano-di.com/dragonfly-iv.

[115] Fairview Microwave. WR-28 to 2.92mm female waveguide to coax adapter UG-599/U square cover with 26.5 GHz to 40 GHz ka band in copper, gold. [Online] https://www.fairviewmicrowave.com/wr28-2.92mm-female-waveguide-coax-adapter-ug599-square-fmwca1078-p.aspx.

[116] Teledyne Storm Microwave. Dielectric options-low loss, low density PTFE. [Online]https://www.teledynedefenseelectronics.com.

[117] X.-F. Zhang, J.-X. Chen, R.-F. Gao, C. Xu, and Z.-H. Bao. Differential surface plasmon polaritons transmission line with controllable common mode rejection. *Scientific Reports*, 7(1):2974, 2017.

[118] iPCB. Insertion loss of microstrip line of RO4350B PCB at 24GHz. [Online]https://www.ipcb.com.

[119] Huber Suhner. Sucoflex-103. the high performance microwave cable assembly. [Online]chrome-extension://efaidnbmnnnibpcajpcglclefindmkaj/https://ateservice.jp/as/hs/wp-content/uploads/sites/2/2018/01/SUCOFLEX103.pdf.

[120] McGill Microwave. MaxGain-130. Assemblies are high-performance, ultra-low-loss microwave coaxial cables. [Online]https://www.mcgillmicrowave.com/product/maxgain-130/.

[121] C. S. Tan. Density functional theory study of metallic Silicon (111) plane structures. *ACS Omega*, 7(6):5385–5392, 2022.

UCL Research Paper Declaration Form (Paper 1)

referencing the doctoral candidate's own published work(s)

Please use this form to declare if parts of your thesis are already available in another format, e.g. if data, text, or figures:

- *have been uploaded to a preprint server*
- *are in submission to a peer-reviewed publication*
- *have been published in a peer-reviewed publication, e.g. journal, textbook.*

This form should be completed as many times as necessary. For instance, if you have seven thesis chapters, two of which containing material that has already been published, you would complete this form twice.

1. **For a research manuscript that has already been published** (if not yet published, please skip to section 2)

a) **What is the title of the manuscript?**

b) **Please include a link to or doi for the work**

c) **Where was the work published?**

d) **Who published the work?** (e.g. OUP)

e) **When was the work published?**

f) **List the manuscript's authors in the order they appear on the publication**

g) **Was the work peer reviewed?**

h) **Have you retained the copyright?**

i) **Was an earlier form of the manuscript uploaded to a preprint server?** (e.g. medRxiv). If 'Yes', please give a link or doi)

If 'No', please seek permission from the relevant publisher and check the box next to the below statement:

☐

*I acknowledge permission of the publisher named under **1d** to include in this thesis portions of the publication named as included in **1c**.*

2. **For a research manuscript prepared for publication but that has not yet been published** (if already published, please skip to section 3)

a) **What is the current title of the manuscript?**

On propagation characteristics of reconfigurable surface-wave platform: Simulation and experimental verification

b) **Has the manuscript been uploaded to a preprint server?** (e.g. medRxiv; if 'Yes', please give a link or doi)

Yes, arXiv:2304.13903

c) **Where is the work intended to be published?** (e.g. journal names)

IEEE Transactions on Antennas and Propagation

d) **List the manuscript's authors in the intended authorship order**

Zhiyuan Chu, Kin-Fai Tong, Kai-Kit Wong, Chan-Byoung Chae, and Chi Hou Chan

e) **Stage of publication** (e.g. in submission)

Submitted (under review)

3. **For multi-authored work, please give a statement of contribution covering all authors** (if single-author, please skip to section 4)

We, the authors of this paper, hereby provide a statement of contribution. We acknowledge that each author has contributed substantially to different aspects of this work, including but not limited to conceptualization, methodology, data collection and analysis, writing and editing, and critical review.

4. **In which chapter(s) of your thesis can this material be found?**

Chapter 4, Chapter 5

5. **e-Signatures confirming that the information above is accurate** (this form should be co-signed by the supervisor/ senior author unless this is not appropriate, e.g. if the paper was a single-author work)

Candidate

Zhiyuan Chu

Date:

14/08/2023

Supervisor/ Senior Author (where appropriate)

Kai-Kit Wong

Date

22/06/2023

UCL Research Paper Declaration Form (Paper 2)

referencing the doctoral candidate's own published work(s)

Please use this form to declare if parts of your thesis are already available in another format, e.g. if data, text, or figures:

- *have been uploaded to a preprint server*
- *are in submission to a peer-reviewed publication*
- *have been published in a peer-reviewed publication, e.g. journal, textbook.*

This form should be completed as many times as necessary. For instance, if you have seven thesis chapters, two of which containing material that has already been published, you would complete this form twice.

1. **For a research manuscript that has already been published** (if not yet published, please skip to section 2)

a) **What is the title of the manuscript?**

b) **Please include a link to or doi for the work**

c) **Where was the work published?**

d) **Who published the work?** (e.g. OUP)

e) **When was the work published?**

f) **List the manuscript's authors in the order they appear on the publication**

g) **Was the work peer reviewed?**

h) **Have you retained the copyright?**

i) **Was an earlier form of the manuscript uploaded to a preprint server?** (e.g. medRxiv). If 'Yes', please give a link or doi)

If 'No', please seek permission from the relevant publisher and check the box next to the below statement:

☐

*I acknowledge permission of the publisher named under **1d** to include in this thesis portions of the publication named as included in **1c**.*

2. **For a research manuscript prepared for publication but that has not yet been published** (if already published, please skip to section 3)

a) **What is the current title of the manuscript?**

Reconfigurable surface wave divider

b) **Has the manuscript been uploaded to a preprint server?** (e.g. medRxiv; if 'Yes', please give a link or doi)

No

c) **Where is the work intended to be published?** (e.g. journal names)

Scientific Reports

d) **List the manuscript's authors in the intended authorship order**

Zhiyuan Chu, Kin-Fai Tong, Kai-Kit Wong, Chan-Byoung Chae, and Yangyang Zhang

e) **Stage of publication** (e.g. in submission)

Submitted (under review)

3. **For multi-authored work, please give a statement of contribution covering all authors** (if single-author, please skip to section 4)

We, the authors of this paper, hereby provide a statement of contribution. We acknowledge that each author has contributed substantially to different aspects of this work, including but not limited to conceptualization, methodology, data collection and analysis, writing and editing, and critical review.

4. **In which chapter(s) of your thesis can this material be found?**

Chapter 6

5. **e-Signatures confirming that the information above is accurate** (this form should be co-signed by the supervisor/ senior author unless this is not appropriate, e.g. if the paper was a single-author work)

Candidate

Zhiyuan Chu

Date:

14/08/2023

Supervisor/ Senior Author (where appropriate)

Kai-Kit Wong

Date

14/08/2023

UCL Research Paper Declaration Form (Paper 3)

referencing the doctoral candidate's own published work(s)

Please use this form to declare if parts of your thesis are already available in another format, e.g. if data, text, or figures:

- *have been uploaded to a preprint server*
- *are in submission to a peer-reviewed publication*
- *have been published in a peer-reviewed publication, e.g. journal, textbook.*

This form should be completed as many times as necessary. For instance, if you have seven thesis chapters, two of which containing material that has already been published, you would complete this form twice.

1. **For a research manuscript that has already been published** (if not yet published, please skip to section 2)

a) **What is the title of the manuscript?**

b) **Please include a link to or doi for the work**

c) **Where was the work published?**

d) **Who published the work?** (e.g. OUP)

e) **When was the work published?**

f) **List the manuscript's authors in the order they appear on the publication**

g) **Was the work peer reviewed?**

h) **Have you retained the copyright?**

i) **Was an earlier form of the manuscript uploaded to a preprint server?** (e.g. medRxiv). If 'Yes', please give a link or doi)

If 'No', please seek permission from the relevant publisher and check the box next to the below statement:

☐

*I acknowledge permission of the publisher named under **1d** to include in this thesis portions of the publication named as included in **1c**.*

2. **For a research manuscript prepared for publication but that has not yet been published** (if already published, please skip to section 3)

a) **What is the current title of the manuscript?**

Study on surface wave path loss in reconfigurable surface guided pathways

b) **Has the manuscript been uploaded to a preprint server?** (e.g. medRxiv; if 'Yes', please give a link or doi)

No

c) **Where is the work intended to be published?** (e.g. journal names)

IEEE Transactions on communications

d) **List the manuscript's authors in the intended authorship order**

Zhiyuan Chu, Kin-Fai Tong, Kai-Kit Wong, Chan-Byoung Chae, and Yangyang Zhang

e) **Stage of publication** (e.g. in submission)

Prepare to submit

3. **For multi-authored work, please give a statement of contribution covering all authors** (if single-author, please skip to section 4)

We, the authors of this paper, hereby provide a statement of contribution. We acknowledge that each author has contributed substantially to different aspects of this work, including but not limited to conceptualization, methodology, data collection and analysis, writing and editing, and critical review.

4. **In which chapter(s) of your thesis can this material be found?**

Chapter 3

5. **e-Signatures confirming that the information above is accurate** (this form should be co-signed by the supervisor/ senior author unless this is not appropriate, e.g. if the paper was a single-author work)

Candidate

Zhiyuan Chu

Date:

14/08/2023

Supervisor/ Senior Author (where appropriate)

Kai-Kit Wong

Date

14/08/2023

UCL Research Paper Declaration Form (Paper 4)

referencing the doctoral candidate's own published work(s)

Please use this form to declare if parts of your thesis are already available in another format, e.g. if data, text, or figures:

- *have been uploaded to a preprint server*
- *are in submission to a peer-reviewed publication*
- *have been published in a peer-reviewed publication, e.g. journal, textbook.*

This form should be completed as many times as necessary. For instance, if you have seven thesis chapters, two of which containing material that has already been published, you would complete this form twice.

1. **For a research manuscript that has already been published** (if not yet published, please skip to section 2)

a) **What is the title of the manuscript?**

Enhancing and localizing surface wave propagation with reconfigurable surfaces

b) **Please include a link to or doi for the work**

https://doi.org/10.23919/ISAP47258.2021.9614402

c) **Where was the work published?**

2021 International Symposium on Antennas and Propagation (ISAP), Taipei, Taiwan

d) **Who published the work?** (e.g. OUP)

IEEE

e) **When was the work published?**

19-22 October 2021

f) **List the manuscript's authors in the order they appear on the publication**

Zhiyuan Chu; Kai-Kit Wong; Kin-Fai Tong

g) **Was the work peer reviewed?**

Yes

h) **Have you retained the copyright?**

No, transfer it to IEEE

i) **Was an earlier form of the manuscript uploaded to a preprint server?** (e.g. medRxiv). If 'Yes', please give a link or doi)

arXiv:2106.10569

If 'No', please seek permission from the relevant publisher and check the box next to the below statement:

☐

*I acknowledge permission of the publisher named under **1d** to include in this thesis portions of the publication named as included in **1c**.*

2. **For a research manuscript prepared for publication but that has not yet been published** (if already published, please skip to section 3)

a) **What is the current title of the manuscript?**

b) **Has the manuscript been uploaded to a preprint server?** (e.g. medRxiv; if 'Yes', please give a link or doi)

c) **Where is the work intended to be published?** (e.g. journal names)

d) **List the manuscript's authors in the intended authorship order**

e) **Stage of publication** (e.g. in submission)

3. **For multi-authored work, please give a statement of contribution covering all authors** (if single-author, please skip to section 4)

We, the authors of this paper, hereby provide a statement of contribution. We acknowledge that each author has contributed substantially to different aspects of this work, including but not limited to conceptualization, methodology, data collection and analysis, writing and editing, and critical review.

4. **In which chapter(s) of your thesis can this material be found?**

Chapter 3

5. **e-Signatures confirming that the information above is accurate** (this form should be co-signed by the supervisor/ senior author unless this is not appropriate, e.g. if the paper was a single-author work)

Candidate

Zhiyuan Chu

Date:

14/08/2023

Supervisor/ Senior Author (where appropriate)

Kai-Kit Wong

Date:

14/08/2023

UCL Research Paper Declaration Form (Paper 5)

referencing the doctoral candidate's own published work(s)

Please use this form to declare if parts of your thesis are already available in another format, e.g. if data, text, or figures:

- *have been uploaded to a preprint server*
- *are in submission to a peer-reviewed publication*
- *have been published in a peer-reviewed publication, e.g. journal, textbook.*

This form should be completed as many times as necessary. For instance, if you have seven thesis chapters, two of which containing material that has already been published, you would complete this form twice.

1. **For a research manuscript that has already been published** (if not yet published, please skip to section 2)

a) **What is the title of the manuscript?**

Reconfigurable surface wave platform using fluidic conductive structures

b) **Please include a link to or doi for the work**

https://doi.org/10.23919/ISAP47258.2021.9614402

c) **Where was the work published?**

2021 IEEE International Symposium on Antennas and Propagation and USNC-URSI Radio Science Meeting (APS/URSI), Singapore, Singapore

d) **Who published the work?** (e.g. OUP)

IEEE

e) **When was the work published?**

04-10 December 2021

f) **List the manuscript's authors in the order they appear on the publication**

Zhiyuan Chu; Kai-Kit Wong; Kin-Fai Tong

g) **Was the work peer reviewed?**

Yes

h) **Have you retained the copyright?**

No, transfer it to IEEE

i) **Was an earlier form of the manuscript uploaded to a preprint server?** (e.g. medRxiv). If 'Yes', please give a link or doi)

arXiv:2105.10810

If 'No', please seek permission from the relevant publisher and check the box next to the below statement:

☐

*I acknowledge permission of the publisher named under **1d** to include in this thesis portions of the publication named as included in **1c**.*

2. **For a research manuscript prepared for publication but that has not yet been published** (if already published, please skip to section 3)

a) **What is the current title of the manuscript?**

b) **Has the manuscript been uploaded to a preprint server?** (e.g. medRxiv; if 'Yes', please give a link or doi)

c) **Where is the work intended to be published?** (e.g. journal names)

d) **List the manuscript's authors in the intended authorship order**

e) **Stage of publication** (e.g. in submission)

3. **For multi-authored work, please give a statement of contribution covering all authors** (if single-author, please skip to section 4)

We, the authors of this paper, hereby provide a statement of contribution. We acknowledge that each author has contributed substantially to different aspects of this work, including but not limited to conceptualization, methodology, data collection and analysis, writing and editing, and critical review.

4. **In which chapter(s) of your thesis can this material be found?**

Chapter 3

5. **e-Signatures confirming that the information above is accurate** (this form should be co-signed by the supervisor/ senior author unless this is not appropriate, e.g. if the paper was a single-author work)

Candidate

Zhiyuan Chu

Date:

14/08/2023

Supervisor/ Senior Author (where appropriate)

Kai-Kit Wong

Date:

14/08/2023

UCL Research Paper Declaration Form (Paper 6)

referencing the doctoral candidate's own published work(s)

Please use this form to declare if parts of your thesis are already available in another format, e.g. if data, text, or figures:

- *have been uploaded to a preprint server*
- *are in submission to a peer-reviewed publication*
- *have been published in a peer-reviewed publication, e.g. journal, textbook.*

This form should be completed as many times as necessary. For instance, if you have seven thesis chapters, two of which containing material that has already been published, you would complete this form twice.

1. **For a research manuscript that has already been published** (if not yet published, please skip to section 2)

a) **What is the title of the manuscript?**

On Surface Wave Propagation Characteristics of Porosity-Based Reconfigurable Surfaces

b) **Please include a link to or doi for the work**

https://doi.org/10.23919/APMC55665.2022.9999806

c) **Where was the work published?**

2022 Asia-Pacific Microwave Conference (APMC), Yokohama, Japan

d) **Who published the work?** (e.g. OUP)

IEEE

e) **When was the work published?**

29 November 2022 - 02 December 2022

f) **List the manuscript's authors in the order they appear on the publication**

Zhiyuan Chu; Kai-Kit Wong; Kin-Fai Tong

g) **Was the work peer reviewed?**

Yes

h) **Have you retained the copyright?**

No, transfer it to IEEE

i) **Was an earlier form of the manuscript uploaded to a preprint server?** (e.g. medRxiv). If 'Yes', please give a link or doi)

arXiv:2206.11401

If 'No', please seek permission from the relevant publisher and check the box next to the below statement:

☐

*I acknowledge permission of the publisher named under **1d** to include in this thesis portions of the publication named as included in **1c**.*

2. **For a research manuscript prepared for publication but that has not yet been published** (if already published, please skip to section 3)

a) **What is the current title of the manuscript?**

b) **Has the manuscript been uploaded to a preprint server?** (e.g. medRxiv; if 'Yes', please give a link or doi)

c) **Where is the work intended to be published?** (e.g. journal names)

d) **List the manuscript's authors in the intended authorship order**

e) **Stage of publication** (e.g. in submission)

3. **For multi-authored work, please give a statement of contribution covering all authors** (if single-author, please skip to section 4)

We, the authors of this paper, hereby provide a statement of contribution. We acknowledge that each author has contributed substantially to different aspects of this work, including but not limited to conceptualization, methodology, data collection and analysis, writing and editing, and critical review.

4. **In which chapter(s) of your thesis can this material be found?**

Chapter 3

5. **e-Signatures confirming that the information above is accurate** (this form should be co-signed by the supervisor/ senior author unless this is not appropriate, e.g. if the paper was a single-author work)

Candidate

Zhiyuan Chu

Date:

14/08/2023

Supervisor/ Senior Author (where appropriate)

Kai-Kit Wong

Date:

14/08/2023

UCL Research Paper Declaration Form (Paper 7)

referencing the doctoral candidate's own published work(s)

Please use this form to declare if parts of your thesis are already available in another format, e.g. if data, text, or figures:

- *have been uploaded to a preprint server*
- *are in submission to a peer-reviewed publication*
- *have been published in a peer-reviewed publication, e.g. journal, textbook.*

This form should be completed as many times as necessary. For instance, if you have seven thesis chapters, two of which containing material that has already been published, you would complete this form twice.

1. **For a research manuscript that has already been published** (if not yet published, please skip to section 2)

a) **What is the title of the manuscript?**

A vision to smart radio environment: Surface wave communication superhighways

b) **Please include a link to or doi for the work**

https://doi.org/10.1109/MWC.001.2000162

c) **Where was the work published?**

IEEE Wireless Communications

d) **Who published the work?** (e.g. OUP)

IEEE

e) **When was the work published?**

February 2021

f) **List the manuscript's authors in the order they appear on the publication**

Kai-Kit Wong, Kin-Fai Tong, Zhiyuan Chu, Yangyang Zhang

g) **Was the work peer reviewed?**

Yes

h) **Have you retained the copyright?**

No, transfer it to IEEE

i) **Was an earlier form of the manuscript uploaded to a preprint server?** (e.g. medRxiv). If 'Yes', please give a link or doi)

arXiv:2005.14082

If 'No', please seek permission from the relevant publisher and check the box next to the below statement:

☐

*I acknowledge permission of the publisher named under **1d** to include in this thesis portions of the publication named as included in **1c**.*

2. **For a research manuscript prepared for publication but that has not yet been published** (if already published, please skip to section 3)

a) **What is the current title of the manuscript?**

b) **Has the manuscript been uploaded to a preprint server?** (e.g. medRxiv; if 'Yes', please give a link or doi)

c) **Where is the work intended to be published?** (e.g. journal names)

d) **List the manuscript's authors in the intended authorship order**

e) **Stage of publication** (e.g. in submission)

3. **For multi-authored work, please give a statement of contribution covering all authors** (if single-author, please skip to section 4)

We, the authors of this paper, hereby provide a statement of contribution. We acknowledge that each author has contributed substantially to different aspects of this work, including but not limited to conceptualization, methodology, data collection and analysis, writing and editing, and critical review.

4. **In which chapter(s) of your thesis can this material be found?**

Chapter 2

5. **e-Signatures confirming that the information above is accurate** (this form should be co-signed by the supervisor/ senior author unless this is not appropriate, e.g. if the paper was a single-author work)

Candidate

Zhiyuan Chu

Date:

14/08/2023

Supervisor/ Senior Author (where appropriate)

Kai-Kit Wong

Date

14/08/2023

UCL Research Paper Declaration Form (Paper 8)

referencing the doctoral candidate's own published work(s)

Please use this form to declare if parts of your thesis are already available in another format, e.g. if data, text, or figures:

- *have been uploaded to a preprint server*
- *are in submission to a peer-reviewed publication*
- *have been published in a peer-reviewed publication, e.g. journal, textbook.*

This form should be completed as many times as necessary. For instance, if you have seven thesis chapters, two of which containing material that has already been published, you would complete this form twice.

1. **For a research manuscript that has already been published** (if not yet published, please skip to section 2)

a) **What is the title of the manuscript?**

MIMO evolution beyond 5G through reconfigurable intelligent surfaces and fluid antenna systems

b) **Please include a link to or doi for the work**

https://doi.org/10.1109/MWC.001.2000162

c) **Where was the work published?**

Proceedings of the IEEE

d) **Who published the work?** (e.g. OUP)

IEEE

e) **When was the work published?**

September 2022

f) **List the manuscript's authors in the order they appear on the publication**

Arman Shojaeifard, Kai-Kit Wong, Kin-Fai Tong, Zhiyuan Chu, Alain Mourad, Afshin Haghighat, Ibrahim Hemadeh, Nhan Thanh Nguyen, Visa Tapio, and Markku Juntti

g) **Was the work peer reviewed?**

Yes

h) **Have you retained the copyright?**

No, transfer it to IEEE

i) **Was an earlier form of the manuscript uploaded to a preprint server?** (e.g. medRxiv). If 'Yes', please give a link or doi)

arXiv:2005.14082

If 'No', please seek permission from the relevant publisher and check the box next to the below statement:

☒

*I acknowledge permission of the publisher named under **1d** to include in this thesis portions of the publication named as included in **1c**.*

2. **For a research manuscript prepared for publication but that has not yet been published** (if already published, please skip to section 3)

a) **What is the current title of the manuscript?**

b) **Has the manuscript been uploaded to a preprint server?** (e.g. medRxiv; if 'Yes', please give a link or doi)

c) **Where is the work intended to be published?** (e.g. journal names)

d) **List the manuscript's authors in the intended authorship order**

e) **Stage of publication** (e.g. in submission)

3. **For multi-authored work, please give a statement of contribution covering all authors** (if single-author, please skip to section 4)

We, the authors of this paper, hereby provide a statement of contribution. We acknowledge that each author has contributed substantially to different aspects of this work, including but not limited to conceptualization, methodology, data collection and analysis, writing and editing, and critical review.

4. **In which chapter(s) of your thesis can this material be found?**

Chapter 2

5. **e-Signatures confirming that the information above is accurate** (this form should be co-signed by the supervisor/ senior author unless this is not appropriate, e.g. if the paper was a single-author work)

Candidate

Zhiyuan Chu

Date:

14/08/2023

Supervisor/ Senior Author (where appropriate)

Kai-Kit Wong

Date

14/08/2023